University of Rome "Sapienza"

Department of Chemical Engineering, Materials and Environment

ASSESSMENT OF DAMAGE TO PEOPLE AND BUILDINGS AS CONSEQUENCE OF HYDROGEN PIPELINE ACCIDENTS

PhD in Chemical Engineering
XXXII cycle

Tutor
Prof.ssa Paola Russo

Candidate
Alessandra De Marco

A.A. 2018/2019

Publications list

International Journals

Russo P., **De Marco A**., Mazzaro M., Capobianco L., 2018, *Quantitative risk assessment on a hydrogen refuelling station*, Chemical Engineering Transactions, 67, pp. 739-744.

Russo P., **De Marco A**., Parisi F., 2019, *Failure of concrete and tuff stone masonry buildings as consequence of hydrogen pipeline explosions*, International Journal of Hydrogen Energy, 44, pp. 21067- 21079.

Conference proceedings

Russo P., **De Marco A**., Parisi F., 2018, *Failure probability of reinforced concrete buildings as consequence of hydrogen pipeline explosions,* In*:* HYPOTHESIS XIII, Book of Abstracts, Lecture A9/3, Singapore, 24-28 July 2018.

Russo P., **De Marco A**., Parisi F., 2019, *Impact assessment on people and buildings for hydrogen pipeline explosions*, Proceedings of 8th International Conference on Hydrogen Safety, (ICHS 2019), pp. 248-269, Adelaide, South Australia, 24-26 September, 2019.

Abstract

Hydrogen is increasingly considered a valid alternative to traditional fuels, which are gradually being more and more depleted. It is defined as “the energy carrier of the future” and so, as such, it must be produced. Several hydrogen production technologies are widespread and they involve both traditional and innovative sources. After its production, the hydrogen must be made available for use and, so, it must be transported from the production site to the utilization site.

One of the most common ways to transport considerable quantities of gaseous hydrogen is through pipelines.

Since hydrogen is considered a “no safe” fuel due to its physical properties, the consequences of an accidental release must be investigated, to preserve the safety of people and facilities located in the surrounding area of a possible accidental event involving pipelines.

Hydrogen disperses into the air very easily, being lighter than air, but if it is released in a confined space can result in an explosion.

The hazards of the hydrogen-air mixture are related to the wide flammability range and the low minimum ignition energy. Furthermore, hydrogen burns with an invisible flame and so it is very difficult to suddenly identify the presence of danger.

Based on these considerations, it results that a failure of pipeline conveying gaseous hydrogen can pose severe risks.

The aim of this study is to evaluate damage to people and buildings involved in high-pressure hydrogen pipeline explosions and (jet) fires and, to this scope, a probabilistic risk assessment procedure is proposed.

The annual probability of damage to people and to buildings exposed to an extreme event is calculated as the product of the conditional probability of damage given by a fire or an explosion and the probability of occurrence of the fire/explosion as consequence of pipeline failure.

The consequences of hydrogen pipeline accidents are estimated through different tools: the SLAB integral model is used to define the gas dispersion, the TNO Multi-Energy Method to evaluate the overpressure and impulse generated from the explosions and Pressure-Impulse diagrams to evaluate damage to buildings.

The flame length is calculated through the SLAB model by considering the length at which the hydrogen concentrations of 4% (lower limit flammability) is reached.

The point source model is employed to estimate the radiative heat flux generated by jet fire with the radiant fraction calculated through the empirical correlation proposed by Molina et al. (2007).

Finally, the Probit equations are used to calculate damage to people, both in the case of an explosion and a jet fire. The characteristic quantities of the two accidental events investigated, overpressure and impulse in the case of the explosions and radiative heat flux in the case of jet fires, are considered as causative variables.

Reinforced concrete buildings and tuff stone masonry buildings are taken into consideration to estimate the effect of overpressure and impulse caused by an explosion.

Direct and indirect damage on the people are investigated to define the effects of consequence of explosions and jet fires.

The probabilistic procedure proposed can represent a useful tool in the design of a new hydrogen distribution network and in risks assessment for existing ones.

Contents

Publications list ii

Abstract iii

List of Figures viii

List of Tables xiii

CHAPTER 1

Hydrogen

1.1 Introduction 1

1.2 Hydrogen properties relevant to safety 2

1.3 Hazards related to the use of hydrogen 6

1.4 Thesis Objectives 6

1.5 Thesis Structures 8

CHAPTER 2

Hydrogen accidents

2.1 Introduction 9

2.2 Elements of risk analysis 12

2.3 Methodology 15

CHAPTER 3

Consequences of accidents involving gaseous hydrogen

3.1 Introduction 17

3.2 Hydrogen release through a hole 17

3.3 Hydrogen dispersion 19

3.3.1 The SLAB model and validation for hydrogen dispersion 21

3.4 Hydrogen explosions 32

3.4.1 Multi-Energy Method 33

3.4.2 SLAB + TNO model for blast hazard evaluation 35

3.5 Damage to structural components: Blast fragility 39

3.5.1 Reinforced concrete columns 42

3.5.2 Tuff stone masonry walls 44

3.6 Comparison between hydrogen and natural-gas pipeline 45

3.7 Damage to people involved in an explosion 46

3.8 Hydrogen Jet fires 48

3.8.1 Flame length and validation of the SLAB model 49

3.8.2 Radiative heat flux: literature review 52

3.8.3 Prediction of radiative heat flux 57

3.8.4 SLAB + point source model for radiative heat flux 60

3.9 Damage to people involved in a jet fire 61

3.10 Damage to structures involved in a jet fire 64

CHAPTER 4

Results and discussion

4.1 Introduction 66

4.2 Blast hazard 67

4.3 Damage to structural components 71

4.4 Case study 75

4.5 Comparison between hydrogen and natural gas pipelines 77

4.6 Damage to people involved in an explosion 80

4.7 Fire hazard 84

4.8 Damage to people due to jet fire 86

4.9 Damage to structures due to jet fire 95

4.10 Safety distance 96

4.11 Prevention and Mitigation systems 98

4.11.1 Prevention and Mitigation measures relating to the leakage 99

CHAPTER 5

Conclusions 101

References 104

Nomenclature 112

List of Figures

CHAPTER 1

Figure 1.1: Hydrogen jet fire and gasoline fire 2

Figure 1.2: The phase diagram of hydrogen 3

Figure 1.3: Momentum-controlled jet, transitional jet and buoyancy-controlled for a horizontal jet. 5

CHAPTER 2

Figure 2.1: Hydrogen Production plant distribution in the World 9

Figure 2.2: Capacity (Nm^3/h) of hydrogen production plants 10

Figure 2.3: Main causes of accidents involving hydrogen (data from Gerboni and Salvator, 2019) 12

Figure 2.4: Example of an event tree constructed for a failure of a pipeline carrying hydrogen (data from Gerboni and Salvator, 2019) 14

CHAPTER 3

Figure 3.1: A free expansion gas leak 17

Figure 3.2: Characteristic plume following a continuous release and puff following an instantaneous gas release 19

Figure 3.3: Dispersion cloud in the plume dispersion model by SLAB 22

Figure 3.4: Experimental setup related to the trials of Shirvill et al. (2006) 23

Figure 3.5: Comparison of hydrogen concentration (expressed in terms of volume fractions) vs distance between SLAB predictions and experimental data by Shirvill et al. (2006) in the conditions of RUN 3 25

Figure 3.6: Comparison of hydrogen concentration (expressed in terms of volume fractions) vs distance between SLAB predictions and experimental data by Shirvill et al. (2006) in the conditions of RUN 4 25

Figure 3.7: Comparison of hydrogen concentration (expressed in terms of volume fractions) vs distance between SLAB predictions and experimental data by Shirvill et al. (2006) in the conditions of RUN 7 26

Figure 3.8: Comparison of hydrogen concentration (expressed in terms of volume fractions) vs distance between SLAB predictions and experimental data by Shirvill et al. (2006) in the conditions of RUN 11 26

Figure 3.9: Experimental setup considered by Han et al. (2014) 27

Figure 3.10: Comparison of hydrogen concentration (expressed in terms of volume fractions) vs distance between SLAB predictions and experimental data by Han et al. (2014) (P=100 bar, d_f= 1 mm) 28

Figure 3.11: Comparison of hydrogen concentration (expressed in terms of volume fractions) vs distance between SLAB predictions and experimental data by Han et al. (2014) (P=200 bar, d_f= 1 mm) 29

Figure 3.12: Comparison of hydrogen concentration (expressed in terms of volume fractions) vs distance between SLAB predictions and experimental data by Han et al. (2014) (P=300 bar, d_f= 1 mm) 29

Figure 3.13: Comparison of hydrogen concentration (expressed in terms of volume fractions) vs distance between SLAB predictions and experimental data related to Okabayashy et al. (2005) 31

Figure 3.14: Predicted values of hydrogen concentration vs experimental values of hydrogen concentration, expressed in terms of volume fraction 31

Figure 3.15: Blast wave pressure at fixed location 32

Figure 3.16: Sachs-scaled positive -phase duration for the TNO model by Crowl and Louvar (2011) 34

Figure 3.17: Sachs-scaled “side-on” overpressure for the TNO model by Crowl and Louvar (2011) 34

Figure 3.18: Interaction of a blast wave with a rigid structure (Crowl, 2013) 40

Figure 3.19: Pressure-impulse diagrams of RC column at multiple damage levels 43

Figure 3.20: Median pressure-impulse diagram of RC associated with a near collapse 44

Figure 3.21: Pressure-impulse diagrams for different pre-compression levels 45

Figure 3.22: Parameters that characterize the flame shape: flame length (L_f) and flame width (W_f) (Imamaura et al, 2008) 49

Figure 3.23: Validation of flame length evaluated with literature correlation and with SLAB against experimental data 51

Figure 3.24: Single point source model (Hankinson and Lowesmith, 2012) 52

Figure 3.25: Variation of radiative fraction (χ_{rad}) with the factor $\tau_G \alpha_P T_f^4$ for different hydrocarbon flames, proposed by Molina et al. (2007) 53

Figure 3.26: Weighted multi point source model by Hankinson and Lowesmith (2012) 54

Figure 3.27: Line source model by Zhou and Jiang (2016) 56

Figure 3.28: Experimental apparatus (Mogi et al., 2009) 59

Figure 3.29: Validation of procedure for the heat flux prediction against experimental data 59

CHAPTER 4

Figure 4.1: Peak of overpressure (a) and impulse (b) versus hole diameter at different value of operating pressure (d=0.508 m, L=1000 m, R=500 m, atmospheric stability class D, v= 5 m/s, explosivity class 9) 67

Figure 4.2: Peak of overpressure (a) and impulse (b) versus hole diameter at different value of operating pressure (d=0.508 m, L=1000 m, R=500 m, atmospheric stability class D, v= 5 m/s, explosivity class 9) 68

Figure 4.3: Blast probability for the blast strength 6 and atmospheric stability classes D5(a) and F2 (b) 69

Figure 4.4: Blast probability for the blast strength 9 and atmospheric stability classes D5(a) and F2 (b) 70

Figure 4.5: Comparison between blast demand and capacity of RC columns for explosivity class 6 (a) and 9 (b), for atmospheric conditions D5 and F2 72

Figure 4.6: Comparison between blast demand and capacity of TSM walls for explosivity class 6 (a) and 9 (b), for atmospheric conditions D5 and F2 73

Figure 4.7: Case-study TSM building with respect to the pipeline 76

Figure 4.8: Structural components over the building façade 76

Figure 4.9: Assessment of blast impact on structural components Pier 1 (a) and Pier 2 (b) 77

Figure 4.10: Natural gas pipelines: Peak of overpressure (a) and impulse (b) versus hole diameter at different value of operating pressure (d=1.257 m, L=1000 m, R=500 m, atmospheric stability class C, v= 10 m/s, explosivity class 6) 78

Figure 4.11: Natural gas pipelines: Peak of overpressure (a) and impulse (b) versus pipeline length from the centre of compression at different value of pipeline diameters (P_o=5000 kPa, R=500 m, full bore rupture, atmospheric stability class C, v= 10 m/s, explosivity class 6) 79

Figure 4.12: Probability of death due to lung haemorrhage for explosive class 9 and atmospheric stability class F2 82

Figure 4.13: Probability of death due to head impact for explosive class 9 and atmospheric stability class F2 82

Figure 4.14: Probability of death due to whole body impact for explosive class 9 and atmospheric stability class F2 83

Figure 4.15: Probability of injury due to eardrum rupture for explosive class 9 and atmospheric stability class F2 84

Figure 4.16: Radiative heat flux versus hole diameter (d=0.508 m, r= 200 m,L=1000 m, atmospheric stability class F, v= 2 m/s) 85

Figure 4.17: Radiative heat flux versus hole distance to the center of the jet fires (d=0.508 m, d_{hole} = d (full rupture) ,L=1000 m, atmospheric stability class F, v= 2 m/s) 85

Figure 4.18: Probability of fatality due to radiative heat flux (W/m^2) at different distances at t=60 s 87

Figure 4.19: Probability of overall injuries due to radiative heat flux (W/m^2) at different distances at t=60 s 88

Figure 4.20: Probability of injury due to first-degree burns at different distances at t=60 s 88

Figure 4.21: Probability of injury due to second-degree burns at different distances at t=60 s 89

Figure 4.22: Probability of fatality due to radiative heat flux (W/m^2) at different distances at t=300 s 90
Figure 4.23: Probability of overall injuries due to radiative heat flux (W/m^2) at different distances at t=300 s 91
Figure 4.24: Probability of injury due to first-degree burns at different distances at t=300 s 92
Figure 4.25: Probability of overall injury due to second-degree burns at different distances at t=300 s 92
Figure 4.26: Probability of fatality due to radiative heat flux (W/m^2) at different distances at t=600 s 93
Figure 4.27: Probability of overall injuries due to radiative heat flux (W/m^2) at different distances at t=600 s 94
Figure 4.28: Probability of injury due to first-degree burns at different distances at t=600 s 94
Figure 4.29: Probability of injury due to second-degree burns at different distances at t=600 s 95
Figure 4.30: Maximum value of radiative heat flux (kW/m^2) vs distance (m) for an exposure time of 30 min 96
Figure 4.31: Annual risk per 1,000 km of damage to people (first, second degree burns and fatality) vs safety distance, in the case of atmospheric stability class F2, at t=60 s. 97
Figure 4.32: Annual risk per 1,000 km of damage to people (first, second degree burns and fatality) vs safety distance, in the case of atmospheric stability class F2, at t=300 s. 97
Figure 4.33: Annual risk per 1,000 km of damage to people (first, second degree burns and fatality) vs safety distance, in the case of atmospheric stability class F2, at t=600 s. 98

List of Tables

CHAPTER 1

Table 1.1: Main hydrogen properties 4

CHAPTER 2

Table 2.1: Hydrogen production in Europe 10

Table 2.2: Extension of hydrogen pipelines (h2tools, data update in January 2016) 11

Table 2.3: Probability of pipeline rupture (source: Air Liquide, 2005) 14

CHAPTER 3

Table 3.1: Meteorological conditions by Pasquill-Guifford stability classes 20

Table 3.2: Experimental conditions related to the trials of Shirvill et al. (2006) 24

Table 3.3: SLAB simulation parameters for experiments by Shirvill et al. (2006) 24

Table 3.4: Experimental conditions adopted by Han et al. (2014) 27

Table 3.5: SLAB simulation parameters for experiments by Han et al. (2014) 28

Table 3.6: SLAB simulation parameters for experiments by Okabayasky et al. (2005) 30

Table 3.7: Guidelines for the choice of the class number 35

Table 3.8: Main features of hydrogen pipelines around the world, related to a study carried out by Bedel and Junker (2006) 36

Table 3.9: SLAB simulations parameters 37

Table 3.10: Classes of overpressure and impulse 39

Table 3.11: Probit functions for damage caused by explosions 47

Table 3.12: Threshold harm criteria 48

Table 3.13: Values used in the procedure for the heat flux predictions 57

Table 3.14: Classes of radiative heat flux (kW/m^2) 60

Table 3.15: Probit Functions for fires 63

Table 3.16: Threshold harm criteria of Thermal Doses required to give Pain, Burns and Fatal Outcomes 64

Table 3.17: Damage to structures and equipment due to thermal radiation for 30 min exposure times 65

CHAPTER 4

Table 4.1: Pipeline operating parameters and source release properties employed in the simulations 66

Table 4.2: Blast demand radius (m) at different levels of peak overpressure and impulse for explosivity class 6 and atmospheric stability class D5 74

Table 4.3: Blast demand radius (m) at different levels of peak overpressure and impulse for explosivity class 6 and atmospheric stability class F2 74

Table 4.4: Blast demand radius (m) at different levels of peak overpressure and impulse for explosivity class 9 and atmospheric stability class D5 75

Table 4.5: Blast demand radius (m) at different levels of peak overpressure and impulse for explosivity class 9 and atmospheric stability class D5 75

CHAPTER 1

Hydrogen

1.1 Introduction

In recent years, the increasingly massive depletion of energy resources and the gradual change in climatic conditions have become a topic of particular interest worldwide.

Incorrect use and exploitation of natural resources has led to their exhaustion. In reality, the progressive decrease in environmental resources is also linked to the increase in population: the great demographic growth leads to a decrease in the availability of resources.

Furthermore, the use of traditional fuels contributes to the increase in pollution, since it causes ever more greenhouse gas production. The more the concentration of these gases increases, the more the amount of heat in the atmosphere increases and, therefore, the temperature of our planet rises, making the survival of living species increasingly difficult.

In order to overcome these problems, an effort to realize a gradual replacement of traditional fuels by alternative fuels, essentially represented by energy carriers, has been made.

Concerning its definition, an alternative fuel should have certain qualities.

First of all, it must be energy efficient, competitive from the economic point of view, tolerable from an environmental point of view, available, cheap and safe (Balat, 2008).

In the scenario described above, hydrogen is considered one of the most promising fuels of the future, being convenient from an energy point of view, at low polluting impact and a renewable fuel.

Hydrogen is not a primary energy source existing in nature, but it must be produced; in other words, it is defined as an energy carrier.

Several production methods to produce hydrogen are known and they are related to both renewable and traditional energy sources.

Nowadays, the hydrogen production is based mostly on fossil fuels. Well-established technologies (i.e. steam reforming of methane, partial oxidation of natural gas, coal gasification) are widespread, characterized by high efficiencies and low product costs. But innovative technologies based on renewable sources must be developed or improved so that hydrogen

can become more and more competitive. Alternative methods to produce hydrogen employ biomass, through pyrolysis/gasification processes, water, through electrolysis, direct thermal decomposition, thermochemical processes and photolysis (Baykara, 2018).

One of the major obstacles to the diffusion of hydrogen as an alternative fuel is related to the public perception of hydrogen as a “no-safe” fuel.

Certainly, hydrogen is not safer than the current energy sources (i.e. methane, gasoline), but it is not even more dangerous if compared to the other fuels. It must be handled accurately, taking in consideration its properties and the hazards that an inappropriate use can cause (Saffers and Molkov, 2014).

However, beyond the subjective "perception of risk", a careful analysis resizes the concept of hydrogen hazard.

In 2001 Swain (Swain, 2001) carried out the first comparison between a hydrogen and a gasoline fuel leak and ignition. As shown in Figure 1.1, the hydrogen-powered vehicle was undamaged, after both 3 s (left) and 60 s (right) from the fire initiation, on the contrary the gasoline-powered vehicle presented evident severe damage.

Figure 1.1: *Hydrogen jet fire and gasoline fire*

1.2 Hydrogen properties relevant to safety

Hydrogen is the most abundant element in the Universe. It is very rare in the Earth's atmosphere, in which is present with a concentration of about 1 ppm and practically non-existent at pure state on the surface and in the subsoil of the Earth. It is present in combination with other elements.

First element of the periodic table, with an atomic number of 1.008 g/mol, hydrogen represents the lightest founded element, consisting of one proton and one electron. Protium, deuterium and tritium are the three isotopes of hydrogen. At its elementary state, it exists below diatomic molecule form (H_2), whose atoms are held together by covalent bonds.

In atmospheric conditions and at room temperature (298 K), hydrogen is colourless, odourless, tasteless and not detectable in any concentration by human sense. It is a highly flammable gas, non-corrosive and non-toxic.
In order to investigate the physical properties, the phase diagram of hydrogen, shown in Figure 1.2, is taken into consideration (Molkov, 2012).

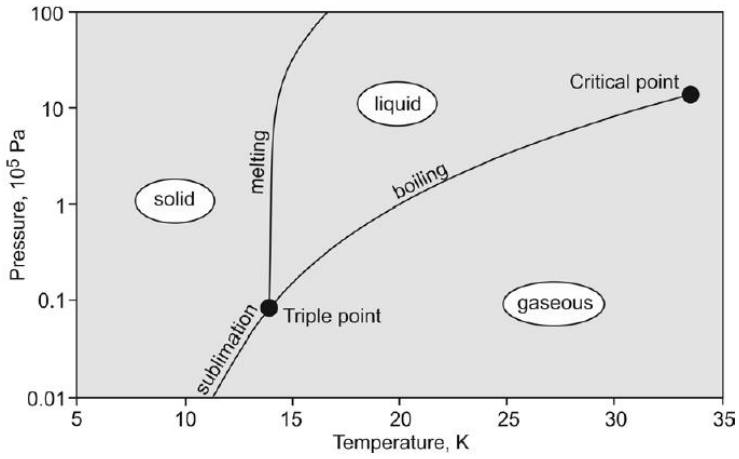

***Figure 1.2**: The phase diagram of hydrogen*

Hydrogen critical conditions are characterized by a temperature of 33.15 K and a pressure of 12.96 x 10^5 Pa. The point in which all three phases can coexist, called "triple point", is represented by a temperature of 13.8 K and a pressure of 0.072 x 10^5 Pa.

At ambient pressure (1.01325 x 10^5 Pa), the boiling temperature is 20.37 K, which corresponds to a value of density of 70.90 kg/m^3.

Hydrogen is characterized by a very low density (0.083 kg/m^3) under normal conditions, and so it is stored at high pressure or cryo-compressed or as liquid, in order to increase its capacities. A high diffusivity (approximately 3 times that of the methane) characterizes the tiny molecules of hydrogen and its values are included in a range from 6.1 x 10^{-5} and 6.8 x 10^{-5} m^2/s.

The specific heat of gaseous hydrogen at constant pressure (c_p) is 14.85 kJ/(kg K) in normal conditions (NTP) and 14.304 kJ/(kg K) in standard conditions (STP). The specific heat ratio (γ) is 1.39 at NTP and 1.405 at STP (Molkov, 2012).

Hydrogen presents a thermal conductivity higher than the other gases: 0.187 W/(m K) at NTP and 0.01694 W/(m K) at STP.

At ambient conditions, the hydrogen reactivity is rather slow, but the presence of an activated agent, i.e. a catalyser or a spark, can accelerate the reaction and make it happen explosively.

The main characteristic properties of hydrogen, which are taken into account in the aspects of use in safety, are the wide range of flammability, 4% to 75% by volume in air at STP, and the very low ignition energy. The minimum ignition energy for a stoichiometric hydrogen-air mixture is 0.018 mJ, 16 times lower than methane, and its autoignition temperature is 783 K.

The characteristic invisible flame of hydrogen can reach high values of temperature. For a stoichiometric mixture (constituted by 29.59 vol % hydrogen and 70.41 vol % air), the adiabatic flame temperature is 2403 K (in air). Hydrogen has a heat of combustion higher than other fuels (119.93 MJ/kg) and a burning velocity ranging between 2.65 and 3.46 m/s, one order of magnitude larger than methane (Rigas and Amyotte, 2013).

Similarly to many real gases, hydrogen suffers an inverse Joule-Thompson effect. Following an expansion, its temperature increases; however, this increase in temperature is not normally sufficient to ignite a hydrogen-air mixture. Further hazards may be considered when handling liquid hydrogen, because it evaporates easily.

The main hydrogen properties are summarized in Table 1.1.

Molecular weight	(g/mol)	2.016
Density	gas (kg/m^3)	0.0838
	liq (kg/m^3)	70.9
Boiling Temperature (at 1 atm)	(K)	20.37
Freezing Temperature	(K)	13.8
Critical point	T (K)	33.15
	P (Pa)	12.96 x 10^5
Triple point	T (K)	13.8
	P (Pa)	0.072 x 10^5

Diffusivity	(m^2/s)	6.1×10^{-5}
Stoichiometric mixture	(% vol)	29.59
Ignition energy	(mJ)	0.018
Flammability range (in air)	(% vol)	4 -75
Adiabatic flame Temperature	(K)	2403
Autoignition Temperature	(K)	783
Latent heat of vaporization	(kJ/kg)	445.6

Table 1.1: *Main hydrogen properties*

Another property of hydrogen which must be taken into consideration in a safety assessment is the buoyancy.

On Earth, hydrogen is the element with the highest buoyancy, being its density lower than that of the air and so it is inclined to not accumulate in the atmosphere, but rapidly to disperse. Above a temperature of 22 K, pure hydrogen presents positively buoyant.

The hydrogen dispersion is more influenced by the buoyancy than by the diffusivity.

As a consequence, a hydrogen release is diluted quickly in the air and its concentration falls out of the flammability range.

The buoyancy effects in unintended hydrogen releases must be taken into account in the evaluation of the type of jet generated. Based on this effect, three types of jets can be identified: momentum-dominant jets, buoyancy-dominant jets and transitional jets, as shown in Figure 1.3 for a horizontal jet (Molkov, 2012).

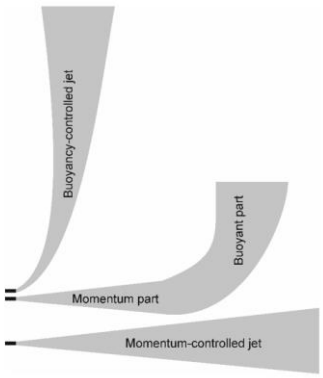

Figure 1.3*: Momentum-controlled jet, transitional jet and buoyancy-controlled jet for a horizontal jet.*

1.3 Hazards related to the use of hydrogen

Hazard can be defined as "a chemical or physical condition that has the potential for causing damage to people, property and the environment" (Molkov, 2012).

Regarding the impact on the environment, since the hydrogen exists naturally in the atmosphere, it does not contribute to alter the environmental stability; the hydrogen gas will be dissipated rapidly in air. When used as a fuel, it does not generate fumes or smoke and, above all, its combustion does not produce greenhouse gases, so hydrogen will not contribute to the atmospheric pollution.

Moreover, hydrogen will not play a part in the groundwater contamination, being a gas at normal atmospheric conditions (HyResponse Report, 2016 (a)).

On the contrary, the impact of hydrogen on people and property is different.

Hydrogen is not considered a carcinogen and no cases of mutagenicity, embryotoxicity, teratogenicity or reproductive toxicity have been shown at present. Hydrogen should not be ingested and, if inhaled, can create a flammable mixture within the human's lungs. It is defined as a simple asphyxiating gas, since a reduction in oxygen concentration in air due to hydrogen may cause breathing problems (dyspnoea). Symptoms as headaches, dizziness, unconsciousness, nausea, vomiting can be present in individual exposition or breathing these atmospheres. Liquid hydrogen can cause hypothermia, also.

In addition to the harms related to people exposure in an area in which an accidental release of hydrogen has occurred, the other harmful effects due to hydrogen combustion have to be considered.

Direct contact with hydrogen flames and radiant heat flux from hydrogen fires, and overpressure and impulse following an explosion are the main harms at which people and property are exposed.

1.4 Thesis objectives

The aim of this thesis is the assessment of damage to people and buildings following a hydrogen pipeline failure.

First of all, a historical analysis of accidents involving hydrogen has been carried out, in order to define the main causes and the related consequences. Mechanical failure of

components of facilities, pipelines or tanks is considered the most common source of accidents.

The first objective is to investigate the potential scenarios connected with a rupture of pipelines transporting gaseous hydrogen. An uncontrollable leakage of gas will mix with air and create a flammable cloud. If a source of ignition is present, a fire or an explosion can occur.

The second objective is the evaluation of the consequences of a jet fire and an explosion on people and properties in the proximity of the accidental event. In the case of a fire, the main hazard to humans and surroundings is connected with the heat radiation, in the case of an explosion the main hazard is related to the overpressure and the impulse generated.

In order to establish the probability that an explosion and a jet fires can cause a given effect, a probabilistic risk assessment procedure for the estimation of damage on two types of buildings (i.e. reinforced concrete and tuff stone masonry buildings) and on people involved in the accident has been proposed.

SLAB one-dimensional integral model has been used to evaluate the atmospheric dispersion of gaseous hydrogen release and, in order to characterize the jet release and the flammable cloud size, a release rate model has been incorporated in this dispersion model.

The overpressure and the impulse resulting from the explosion were estimated through the Multi-Energy Method. Pressure-impulse diagrams has been used to assess the damage to the building structures.

SLAB model has been employed to evaluate the flame length: the distance at which a hydrogen concentration corresponding to the limit lower flammability (4%) has been considered. Empirical correlations of literature have been applied to determine the radiative heat flux. The point source model has been employed to estimate the radiative heat flux with the radiant fraction calculated through the correlation proposed by Molina et al. (2007). In order to ensure their applicability, a validation against experimental data has been carried out.

Finally, damage to people involved in the failure of gaseous hydrogen pipelines were estimated through the Probit functions, which causative variables are represented by the key parameters of the two accidental events considered, overpressure and impulse in the case of the explosions and radiative heat flux in the jet fires one.

Several parameters related to the pipeline characteristics (i.e. pipeline diameter, operating conditions), source release properties (i.e. hole diameter, length of the pipeline from the compression stations) and the atmospheric conditions were taken into consideration to assess the hazards connected with the pipeline failure.

Finally, a minimum safety distance between hydrogen pipelines and people and buildings has been estimated and the procedure proposed can be a useful tool in the design of future pipeline networks and in the assessment of the existing ones.

1.5 Thesis structure

The thesis is structured in five chapters.

In the first chapter a brief overview on the hydrogen potential capabilities as an energy carrier is given, investigating on its physical and combustion properties and the hazards related to an inappropriate handling.

In chapter two, the main methods of delivering hydrogen to the point of use are described. From the performed analysis, it resulted that the most efficient method to transport large quantities of hydrogen is via pipeline. The potential risks connected to failure of a hydrogen gaseous pipeline has been investigated to preserve the health of the people and the integrity of properties in the environment surrounding the area of the accidental event. The potential scenarios have been delineated, also. Fires and explosions were identified as the most frequent events that can occur. A probabilistic procedure to assess the risks connected to jet fires and explosions involving a rupture of a pipeline carrying gaseous hydrogen has been proposed.

Chapter three describes the consequence of a pipeline failure and the effects that it can cause. Both damage to different types of buildings and to people have been taken into consideration. In order to characterize the accidental events that can occur and the quantities that represent them, the dispersion and explosion models and the radiation procedure used in this work have been preliminarily analysed and validated against experimental data.

Chapter four presents the results obtained from the performed analysis, in terms of probability of damage and minimum safety distance.

In the end, chapter five gives the conclusions of the thesis and future work suggestions.

CHAPTER 2

Hydrogen accidents

2.1 Introduction

In order to be considered a successful energy carrier, hydrogen must be economically competitive and the individual technological components must be connected through an infrastructure that provides a safe and environmentally friendly energy system throughout production, from distribution to final use.

The hydrogen market involves two segments: “merchant hydrogen” and “captive hydrogen”. The term “merchant” refers to hydrogen generated in a central production plants and provided to consumers through a pipeline network, tanks or truck delivery; instead, the terms “captive” specifies hydrogen produced directly on the point of use. Currently, the hydrogen market is dominated by the captive hydrogen, which covers 95% of it and it is presumed that it will continue to control it until 2021. In any case, lately, the merchant hydrogen market is expanding and in the USA it has reached about 7% per year. North America represents the widest market for merchant hydrogen (Bezdek, 2019).

Hydrogen production plants are located all over the World, as shown in Figure 2.1 (h2tools database, 2019).

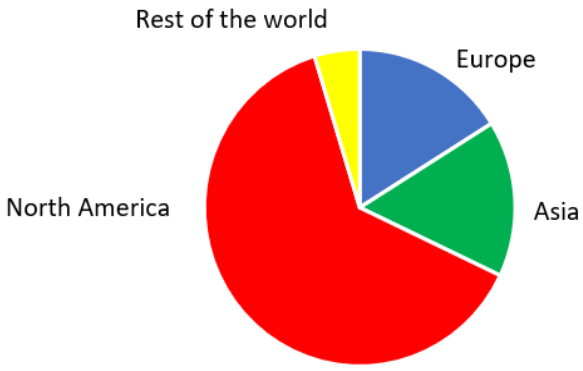

***Figure 2.1**: Hydrogen Production Plant Distribution in the World*

Nowadays, hydrogen is used in many types of industries and for different processes. Most of all, the hydrogen produced is employed in the chemical industry to produce ammonia,

methyl alcohol, fertilizers for agriculture and petroleum products, and in the metallurgical industry for metal treatment. Furthermore, hydrogen is an excellent fuel that can be used to produce energy, in burning hydrogen alone or added to other fuels or directly obtaining electrical energy through a fuel cell. In Figure 2.2 the capacity (Nm^3/h) of the various hydrogen plants diffuse in the World is illustrated (h2tools database, 2019). Data were updated in January 2016 and are related to existing and operating medium and large plants. Many companies have invested in this market and these investments are destined to grow. A recent agreement has been stipulated between the Linde Group and the Praxair Inc, to supply a hydrogen plant in Louisiana, with a production capacity of over 190,000 Nm^3/hr, coming on stream in 2021 (Linde Engineering News, 2019).

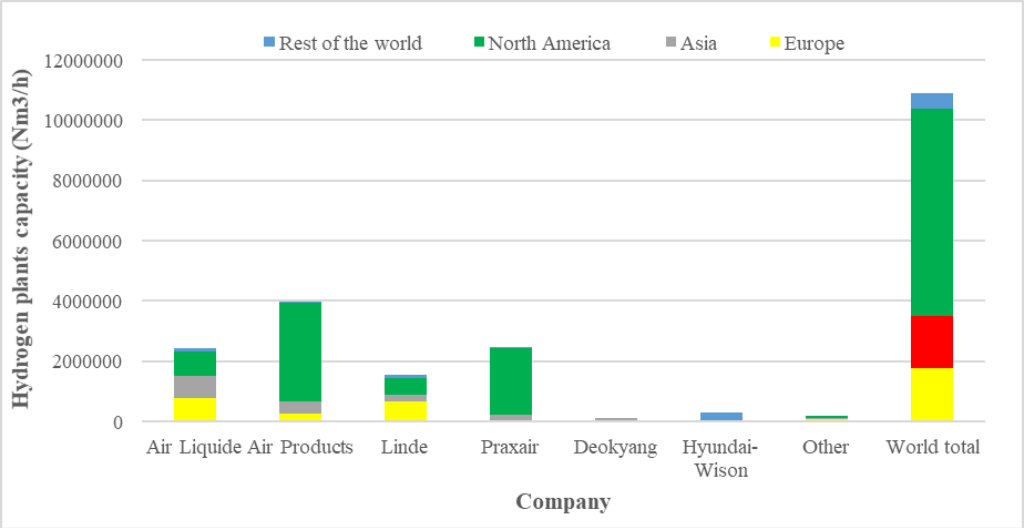

***Figure 2.2**: Capacity (Nm^3/h) of hydrogen production plants*

In recent years, also Europe has been interested in this market and the investments have been increasingly substantial, as shown in Table 2.1 (Eurostat, accessed on 2019).

	2010	2011	2012	2013	2014
Million Nm^3	17.799	17.961	18.345	18.240	18.633

***Table 2.1**: Hydrogen production in Europe*

Generally, hydrogen production plants are located in large industrial sites; consequently the hydrogen produced, regardless of the method used, must be transported from the point of production to the point of utilization (Jo and Ahn, 2006). The hydrogen distribution infrastructure needed for distributing hydrogen to the nationwide network must be increasingly developed.

Hydrogen delivery can be carried out through transmission and distribution lines. The former deliver hydrogen from a production plant to a single point, the latter from a production plant to a distributed network of refuelling stations located in a city or a region.

Currently, the means of transportation which are used in the hydrogen distribution are: compressed tube trailers, cryogenic liquid trucks and compressed gas pipelines. Since the compressed tube trailers cannot handle large capacities of gas (~300 kg of hydrogen), they can be employed only at small scales and used primary for distances of 200 miles or less, and hence they are inefficient from an energetic point of view to meet market demands. Higher volumes can be carried by cryogenic liquid trucks (~ 400-4000 kg of liquid hydrogen), but the high cost and high energy use in the liquefaction process represent the main disadvantages in the use of this kind of delivery (Balat, 2008).

Compressed gas pipelines are the most suitable options to transport large quantities of hydrogen, for high efficiency and low costs.

The major companies have built hydrogen pipeline networks to ensure a stable and uninterrupted hydrogen supply, as shown in Table 2.2 (h2tools database, 2019).

USA have got the largest hydrogen pipeline network, with 2608 km, followed by Europe with 1598 km.

Hydrogen pipelines		
Company	**km**	**Miles**
Air Liquid	1936	1203
Air Product	1140	708
Linde	244	152
Praxair	739	459
Others	483	300
Word total	**4542**	**2823**

Table 2.2: *Extension of hydrogen pipelines (h2tools database, data update in January 2016)*

Pipelines are usually located in industrial areas, but they can also be found in rural and populated zones (Zhang, 2018). For example, in Europe, from Rotterdam to Dunkerque, via Antwerp, a hydrogen pipeline network extends for 900 km.

In view of this, the potential risks due to a failure of a hydrogen gaseous pipeline must be investigated to preserve the health of the people and the integrity of properties in the environment surrounding the area of the accidental event.

2.2 Elements of risk analysis

According to the AIChE/CCPS (2000), *Risk* is "a measure of human injury, environmental damage or economic loss in terms of both the incident likelihood and the magnitude of the loss or injury" (Crowl and Jo, 2011). The combination of a risk analysis and a risk evaluation is called risk assessment.

In order to perform a correct risk assessment, hazards must be identified, possible accident scenario delineated, acceptance criteria specified and the consequences evaluated.

Several methodologies to perform a risk assessment have been reported in literature and applied in different fields. For example, recently, a quantitative risk assessment on a hydrogen refuelling station has been performed (La Chance et al., 2009, Russo et al., 2018).

The risks associated with hydrogen transportation across cities and the countryside by pipelines or tube trailers are investigated in a study carried out by Gerboni and Salvador (2009). Historical analysis of hydrogen accidents is a useful tool to identify the possible hazards and establish the main causes and consequences related to an accidental event.

Several types of accidents have been identified. Generally, six causes are considered the most frequent: i) third parties operations, that are related to activities or interferences caused by others in the proximity of pipelines and not due to an inaccurate management; ii) corrosion, related both to the feature of the transported materials and to the pipe coating; iii) mechanical failure, related to the cracks that occur when the system is subjected to excessive stresses with respect to those the system permits; iv) operational errors, which are caused by an incorrect system management; v) natural events, such as floods, earthquakes, frost; vi) other or unknown causes (Papadakis, 1999).

Various databases were generated in order to collect incidents and to learn from the past.

MHIDAS (Major Hazard Incident Accident Data Service) database contains data related to hazardous materials accidents. It reports that the mechanical failure is the most recurrent

cause of an accident involving hydrogen, analysing a total of 118 accidents (1934-2009), as illustrated in Figure 2.3 (Gerboni and Salvador, 2009).

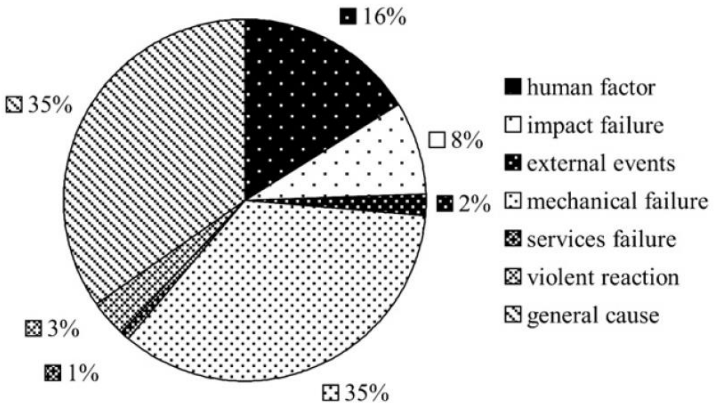

***Figure 2.3**: Main causes of accidents involving hydrogen (data from Gerboni and Salvator, 2009)*

Data has been confirmed by HIAD (Hydrogen Incident and Accident Database), that collects almost 300 hydrogen events, accidents, incidents and near misses (HIAD database, accessed on April 2019). In addition, HIAD presents different sections, depending on the hydrogen system of interest (industry, laboratories, transport).

Valves, flanges, pumps and compressors are some of the components most subjected to mechanical failures, and, since they are additional elements to the main body of the pipeline, an assessment of events involving a failure of hydrogen transportation entails such components to be accounted for.

Due to its low viscosity, hydrogen is much more predisposed to leakages from piping connections than hydrocarbons (HYPER, 2008).

An accurate incidents analysis gives information both about frequency of the initiating event and about the consequences of event (Mirza, 2011).

Investigating on several incidents involving hydrogen pipeline, the probability of pipeline rupture has been evaluated, highlighting that the failure can resolve in a full bore rupture or in a small/partial leak. Air Liquide (2005) has estimated the probability of pipeline rupture in year per km of length of pipeline, as shown in Table 2.3.

Probability of pipeline rupture year x km	
Full bore rupture	6.50E-06
Large leak	
Small leak Out corridor	1.00E-04
Small leak In corridor	2.00E-05

Table 2.3: *Probability of pipeline rupture (source: Air Liquide, 2005)*

The following step of the assessment was to analyse the consequences of an accidental pipeline failure carrying gaseous hydrogen. This type of event can lead to various outcomes. A useful tool to delineate the potential accident scenarios is represented by the event tree analysis. An example of an event tree related to a pipeline accident is reported in Figure 2.4. As shown, hydrogen atmospheric dispersion is the scenario that occurs with a major frequency, but following this event no significant harmful consequences are found.

The next question for an event tree is the probability of ignition. An accurate analysis discerns the ignition into two categories: immediate and delayed, because the consequences that this may cause are different. If an immediate ignition occurs, jet fires is the unique accident that takes place. At a delayed ignition, instead, a hydrogen cloud may form and successively explode. The probability that one of two above-mentioned events takes place will depend on the different features of the surrounding environment (open, confined, ventilated) and on the degree to which it mixes with the air, as well as the power of ignition source.

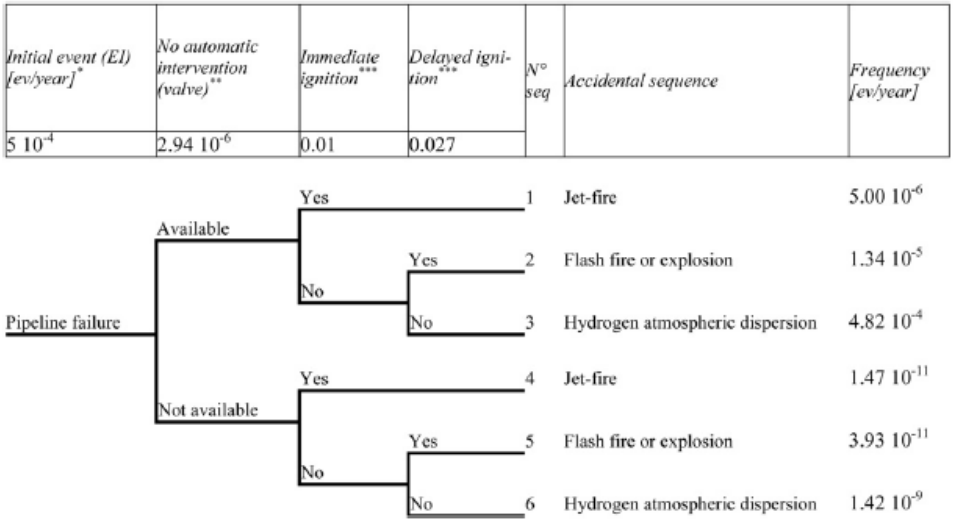

* data from Air Liquide: probability of pipeline rupture [year x km] of 2 x 10^{-5}, assuming a pipeline length of 25 km;
** data from OREDA (Sintef Technology and Society. Offshore reliability data handbook. In: OREDA 2002. 4th ed. Høvik, Norway;
*** data from the statistic report: Available at: http://www.ntsb.gov/publictn/2002/HZM0202.pdf

Figure 2.4*: Example of an event tree constructed for a failure of a pipeline carrying hydrogen (data from Gerboni and Salvator, 2009)*

The frequency of occurrence of explosions and jet fires are 1.34 x 10^{-5}/year and 5.00 x 10^{-6} /year, respectively, as reported by Gerboni and Salvator (2009).

Finally, it is important to quantify the damage and the consequences for people and property in the surrounding area.

The major damage related to the accidental scenarios described above is the collapse of buildings under explosions, and both direct and indirect effects of blast and thermal radiation on people.

In the case of an explosion, local damage to structural elements of buildings, exposed to severe overpressure, can result in a progressive collapse of the whole structure.

In the case of fires, structural components are less affected by smoke and temperature.

2.3 Methodology

In order to estimate the damage to people and buildings involved in an explosion or in a fire due to a high-pressure hydrogen pipeline failure, in this work a probabilistic risk assessment procedure is proposed.

Several probabilistic risk assessment methodologies are proposed in literature. One of the most used is based on the Bayesian Belief Networks (BBN); it is applied to predict the structural stability of civil structures and in process industries.

Risk analysis framework, suggested by Ellingwood (2006), and reported by Russo and Parisi (2016), permits to estimate the annual probability of a structural collapse C caused by an extreme event H, as a combination of the conditional probability of the event of progressive collapse given the local damage (LD) event occurs (Pr[C|LD]) and the conditional probability of local damage given the extreme event H (PR[LD|H]), multiplied by the mean annual rate of occurrence of H (λ_H) (Equation 2.1):

$$\Pr[C] = \Pr[C|LD]\,\Pr[LD|H]\,\lambda_H \quad (2.1)$$

Then, the evaluation of the probability of a progressive collapse can be estimated using the following equation:

$$\Pr[C] = \Pr[C|LD]\,\Pr[LD] \quad (2.2)$$

In the case of an explosion, caused by an accidental release of hydrogen, the annual probability of local structural damage is evaluated as follows:

$$\Pr[LD] = \Pr[LD|E]\,\Pr[E|R]\,\lambda_R \quad (2.3)$$

where E is the explosion event, R is the pipeline rupture, λ_R is the annual mean rate of pipeline rupture occurrence, in a year per 1,000 km.

The terms Pr[LD|E] and Pr[E|R] indicate the conditional probability of the local damage given the extreme event E and the conditional probability of extreme event E given R, respectively.
Pr[E|R] represents the blast hazard function that provides the probability of occurrence of the explosion as a consequence of the pipeline rupture. Pr[LD|E] represents the blast fragility of the structural components.
Multi-Energy Method is used to calculate the blast hazard.

This approach is then extended to the evaluation of the annual probability of damage to people subjected to an extreme event (i.e. explosion, jet fire), following a failure of a hydrogen pipeline, through the Equation 2.4:

$$Pr[D] = Pr[D|E]Pr[E|R]\lambda_R \quad (2.4)$$

where D is the damage to people; E is the accidental event; R is the pipeline rupture; λ_R is annual rate of pipeline rupture occurrence, in a year per 1,000 km.
Probit equations are employed to calculate the damage probability.

CHAPTER 3

Consequences of accidents involving gaseous hydrogen

3.1 Introduction

Pipeline carrying gaseous substances, following an accidental event can result in full rupture or in a hole in the pipe and can cause a release of a large quantity of gas, with consequent diffusion and formation of a cloud.

In order to assess the consequences that can derive from it, after identifying the accident, a release model is developed to describe how the material was released and, subsequently, the concentrations of the released material are estimated by dispersion models.

Finally, the effects that the failure can cause in the surrounding environment are evaluated.

Release models (or source models) are a useful tool to calculate the amount of substance released. These models are built upon basic equations or empirical relationships, that represent the chemical-physical phenomena occurring during the release.

3.2 Hydrogen release through a hole

Gaseous hydrogen discharges through a hole in a pipe can be described taking into account the free expansion release source models, as shown in Figure 3.1 (Crowl and Louvar, 2011). When a high-pressure gas flows and expands through a hole, its pressure energy is converted to kinetic energy.

The released gas flow is obtained solving a mechanical energy balance, considering that density, temperature and pressure are not constant, but they vary considerably between upstream and downstream. An isentropic transformation is assumed.

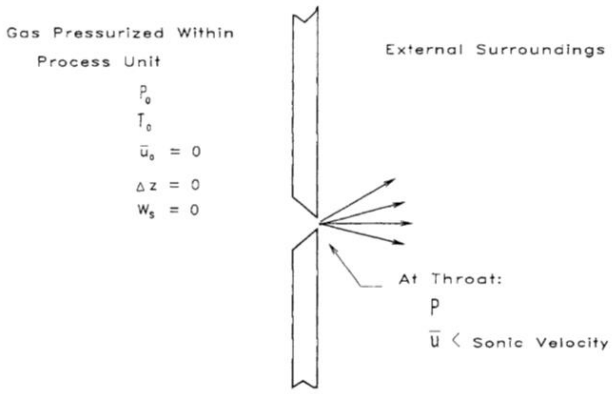

***Figure 3.1**: A free expansion gas leak*

During the expansion, the gas velocity changes with time. The maximum flow rate is found at the hole, where the higher value of downstream pressure is reached. This pressure is called choked pressure (P_{choked}) and is evaluated through the following Equation:

$$\frac{P_{choked}}{P_0} = \left(\frac{2}{\gamma+1}\right)^{\frac{\gamma}{\gamma-1}} \quad (3.1)$$

where P_o is the pressure in the initial condition and γ is the ratio of the heat capacities at pressure and volume constant ($\gamma=C_p/C_v$). In these conditions, the velocity of the gas at the hole is the velocity of sound. These assumptions allow to define a peak initial release, calculated with Equation 3.2:

$$Q_{peak} = \frac{\pi\, d^2\, \alpha}{4} \sqrt{\gamma\, \rho_0\, P_0 \left(\frac{2}{\gamma+1}\right)^{\frac{\gamma+1}{\gamma-1}}} \quad (3.2)$$

assuming that α is the ratio of effective hole area to the pipe sectional area (dimensionless hole size), d is the pipe diameter, ρ_0 and P_0 are the stagnation density and pressure of gas at initial conditions, respectively, and γ is the specific heat ratio of gas.

After reaching the initial peak, the release rate decays over time until it achieves a steady-state; Equation 3.3 allows to obtain this value:

$$Q_{steady-state} = \frac{Q_{peak}}{\sqrt{1+(4\,\alpha^2 f_F \frac{L}{d})\left(\frac{2}{\gamma+1}\right)^{\frac{2}{\gamma-1}}}} \quad (3.3)$$

where f_F is the Fanning friction factor and L is the pipe length from the hydrogen supply station to the release point.

The correlation of Nikuradse has been adopted to value the Fanning friction factor, as proposed by Molkov (2012):

$$\frac{1}{\sqrt{f_F}} = 0.869 \ln\left(Re\sqrt{f_F}\right) - 0.8 \quad (3.4)$$

A value of 0.005643 for f_F has been obtained.

Overestimated values of the mass flow rate of the discharged mass, applied for a gaseous hydrogen release through high pressure pipe, were noted.

A study of the physical properties of the gaseous hydrogen stored at high pressures showed a different behaviour of this gas compared to ideal gases. In order to describe the characteristics of real gas, the Abel-Noble equation of state (Equation 3.5) is taken into account and

incorporated in the Equation 3.2, for the computation of ρ_0. This equation permits to evaluate the compressibility factor z, expressed in terms of co-volume (b):

$$z = 1 + \frac{b\,\rho_0}{R_{H2}\,T} \qquad (3.5)$$

where b is 7.69 10^{-3} m^3/kg, R_{H2} is the hydrogen gas constant, i.e. the ratio of the universal gas constant R to the molecular mass of hydrogen (4124.24 J/kg/K).

3.3 Hydrogen dispersion

Gaseous hydrogen, leaking from a pipeline involved in an accidental event, diffuses into the surrounding environment and various outcomes can arise, depending on the conditions in which the spill occurs.

Several dispersion models are present in the literature to describe the ways in which the gas disperses away from the discharge point and to estimate the downwind concentrations of the released gas. The dispersion calculations also permit to define the area involved in the event (Crowl and Louvar, 2011).

Depending on the duration of the release, continuous or instantaneous, a characteristic plume or puff can be generated, respectively, as shown in Figure 3.2 (a) and (b).

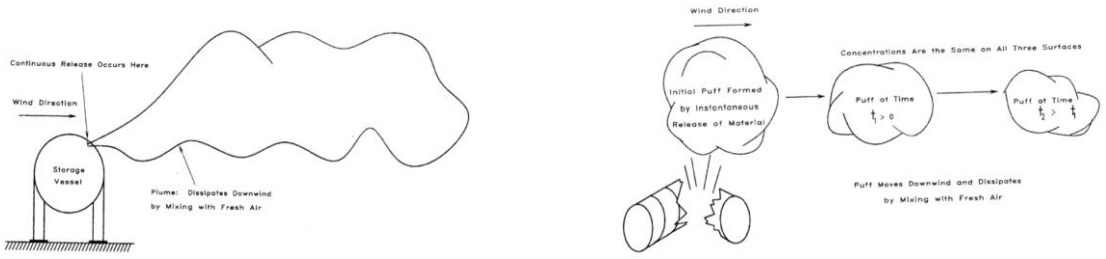

(a) *(b)*

Figure 3.2: *Characteristic plume following a continuous gas release (a) and puff following an instantaneous gas release (b).*

As the gas moves away from the point of release, where the concentration is maximum, it is diluted due to turbulence phenomena and dispersion in air and therefore its concentration is lower.

Several parameters can affect the dispersion and allow a different process evolution. These parameters are essentially characteristic of the environment in which the release takes place,

as the wind speed, the atmospheric stability, the ground conditions, the height of the release above ground level, the momentum and the buoyancy of the gas released.

The meteorological conditions influence the dispersion of the gas in the atmosphere, so a careful evaluation is necessary in order to optimally define the development of the event.

In fact, a high wind speed value allows a greater dispersion of the gas, being diluted faster by a greater quantity of air. Atmospheric stability tends to be classified according to three main classes: stable, neutral and unstable. Pasquill et al. (1961) have established six stability classes, identified with letters A (the least stable conditions) to F (the most stable one), as reported in Table 3.1:

Surface wind speed, m/s	Daytime insolation			Nighttime conditions		Anytime
	Strong	Moderate	Slight	Thin overcast or >4/8 low cloud	≥3/8 cloudiness	Heavy overcast
<2	A	A–B	B	F	F	D
2–3	A–B	B	C	E	F	D
3–4	B	B–C	C	D	D	D
4–6	C	C–D	D	D	D	D
>6	C	D	D	D	D	D

A: Extremely unstable conditions
B: Moderately unstable conditions
C: Slightly unstable conditions
D: Neutral conditions
E: Slighrly stable conditions
F: Moderately stable conditions

Table 3.1: *Meteorological condition by Pasquill-Guifford stability classes*

The wind speed and the quantity of sunlight are taken into consideration in the definition of these stability classes.

Furthermore, the ground characteristics contribute to improving or worsening the phenomenon of dispersion, since it is possible to create mechanical mixing on the surface; the presence of trees and buildings increases mixing, while open areas make it decrease.

Initially, the dispersion is influenced by the speed of the discharge and therefore the momentum will prevail. Departing from the discharge point, the buoyancy comes into play; the denser fluids of the air will tend to fall back to the ground, while the lighter ones will remain suspended. The fundamental parameter is therefore density, on the basis of which a general subdivision can be made between compounds released in heavy gases (density greater than air), neutral gases (same density) and light gases (lower density).

3.3.1 The SLAB model and its validation for hydrogen dispersion

The models used to describe the dispersion phenomenon in the atmosphere can be classified into two families: integral models and three-dimensional models. The integral models solve the mass, energy and momentum balances in simplified forms in order to obtain equations of simple numerical integration; in this way, more determining factors can be taken into account in the economy of the dispersive phenomenon, above all the buoyancy phenomena, but the integral models do not yet allow the modelling of complex geometries.

Three-dimensional models are exploited by computational fluid dynamics (CFD). As the previous ones, they numerically integrate the fundamental balances, but they are able to be applied to any type of fluid in any geometry, even very complex. Furthermore, these models take into consideration turbulence models, but their weaknesses are the high costs and the long calculation times. On the contrary, the integral models require lower costs and relatively low computational times.

In this work, the modelling of the dispersion phenomenon has been performed using the one-dimensional integral model SLAB developed by Lawrence Livermore National Laboratory (Ermark, 1990).

SLAB is a computer model that simulates the jet evolution of a release and its dispersion in the atmosphere. Various types of releases can be considered, e.g. a ground-level evaporating pool, an elevated horizontal or vertical jet and an instantaneous volume source.

The conservation equations of mass, momentum, energy and species are employed to evaluate the atmospheric dispersion of the release. Three steps are planned in the simulation: source identification and initialization of the event of dispersion, valuation of cloud dispersion and valuation of the time-averaged concentration.

Depending on the source type and the loss duration, both modes of atmospheric dispersion, i.e. steady state plume and transient puff mode, are taken into consideration. Figure 3.3 shows the cloud dispersion for heavy gas in the plume dispersion mode, reproduced by SLAB.

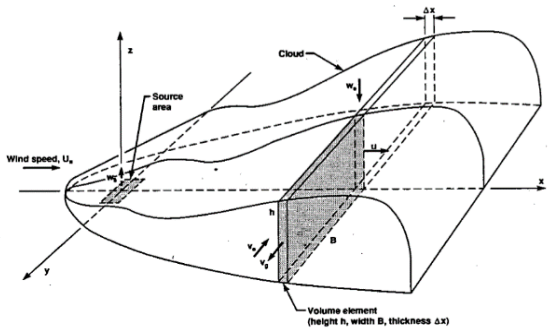

***Figure 3.3**: Dispersion cloud in the plume dispersion model by SLAB*

Several information is required to obtain a correct and fairly complete simulation that describes how the phenomenon of dispersion develops. Data concerning source, spill, field and meteorological properties are used as input parameters and employed to describe the generating cloud.

The most significant output of the simulation is the time-averaged concentration, expressed as the time-averaged volume fraction, as shown in Equation 3.6:

$$C(x,y,z,t) = CC(x) \times [\text{erf}(x_A) - \text{erf}\,(x_B)] \times [\text{erf}(y_A) - \text{erf}(y_B)] \times [\exp(-z_A^2) + \exp(-z_B^2)] \quad (3.6)$$

assuming the following expression for the terms presents in the previous equation:

$$x_A = (x - x_c + b_x)/(\sqrt{2} \times \beta_x)$$

$$x_B = (x - x_c - b_x)/(\sqrt{2} \times \beta_x)$$

$$y_A = (y + b)/(\sqrt{2} \times \beta_C)$$

$$y_B = (y - b)/(\sqrt{2} \times \beta_C)$$

$$z_A = (z - z_C)/(\sqrt{2} \times sig)$$

$$z_B = (z + z_C)/(\sqrt{2} \times sig)$$

in which erf and exp are the error and the exponential function, respectively; x, y and z are the coordinates of the reference system; z_c is the profile centre height (m), b_x is the half-length parameter (m), b is the half-width parameter (m). β_C, β_x and sig are parameters listed in the output.

It was assumed that the concentration profiles have a Gaussian shape and are evaluated in the downwind direction. A weakness of this model is that is does not consider the gas flow around obstacles and does not take into account complex terrain.

The SLAB model is usually employed to simulate dispersion of heavy gas. In order to apply it in the case of hydrogen dispersion, a validation against available experimental data in literature has been realized.

Shirvill et al. (2006) have investigated hydrogen dispersion experiments carried out by Shell Global Solutions and the Health and Safety Laboratory (HSL) to describe the jet releases of hydrogen.

The experimental tests consisted of controlled releases of hydrogen, realized at pressures varying between 1 and 15 MPa. The Figure 3.4 (a) and (b) show the test facility; gaseous hydrogen was released horizontally through different orifices (1, 3, 4, 6 and 12 mm), located at 1.5 m above the ground.

a) b)

Figure 3.4*: Experimental setup related to the trials of Shirvill et al (2006)*

Oxygen concentration measurements within the generated cloud were carried out to assess the hydrogen concentration. The following relationship has been used:

$$C_{H_2} = 100\% \times (V_0 - V_m)/V_0 \quad (3.7)$$

where: V_0 is the sensor output in air and V_m is the sensor voltage in a reduced-oxygen atmosphere. 13 CiTicel AO2 Oxygen sensors, located at different distances from the nozzle, were employed to observe oxygen concentration. Measurements of wind speed and direction were performed.

The experimental conditions used in the trials are summarized in Table 3.2.

Run	Pressure [MPa]	Temperature [°C]	Leak diameter [mm]
1	12	20	4
2	13	18	4
3	12.6	17	4
4	13.7	17	3
5	12.3	15	3
6	11.9	15	3
7	10	14	3
8	9.9	14	3
9	9.3	13.5	4
10	9.4	13	4
11	7.7	13	4
12	7.4	14	3
13	7.4	13.5	3
14	5.0	12.5	3
15	5.6	13	3
16	5.1	14.5	4
17	5.4	14.5	4
18	4.3	14	6
19	4.1	14	6
20	2.3	13.5	6
21	2.6	14	4
22	2.5	14.5	3
23	1.1	14.5	12

***Table 3.2**: Experimental conditions related to the trials of Shirvill et al. (2006)*

Simulations were carried out to validate the SLAB model. SLAB Simulations conditions for the run 3, 4, 7, 11 are reported in Table 3.3.

Parameter	Assumptions RUN 3	Assumptions RUN 4	Assumptions RUN 7	Assumptions RUN 11
Source type	Horizontal jet release	Horizontal jet release	Horizontal jet release	Horizontal jet release
Temperature of source material (K)	206.35	206.29	204.39	203.93
Continuous source duration (s)	0.0	0.0	0.0	0.0
Source height (m)	1.5	1.5	1.5	1.5
Concentration averaging time (s)	0.01	0.01	0.01	0.01
Maximum downwind distance (m)	11	11	11	11
Surface roughness height (m)	0.003	0.003	0.003	0.003
Wind velocity (m/s)	1.2	1.2	1.2	1.2
Height of wind measurement (m)	1.5	1.5	1.5	1.5
Ambient temperature (K)	287	287	287	287
Relative humidity (%)	75	75	75	75
Pasquill atmospheric stability class	6	6	6	6

***Table 3.3**: SLAB simulation parameters for experiments by Shirvill et al. (2006)*

Comparisons between experimental data and simulation results in terms of centreline hydrogen concentration decay as a function of distance are reported in Figures 3.5, 3.6, 3.7 and 3.8 for run 3, 4, 7 and 11, respectively.

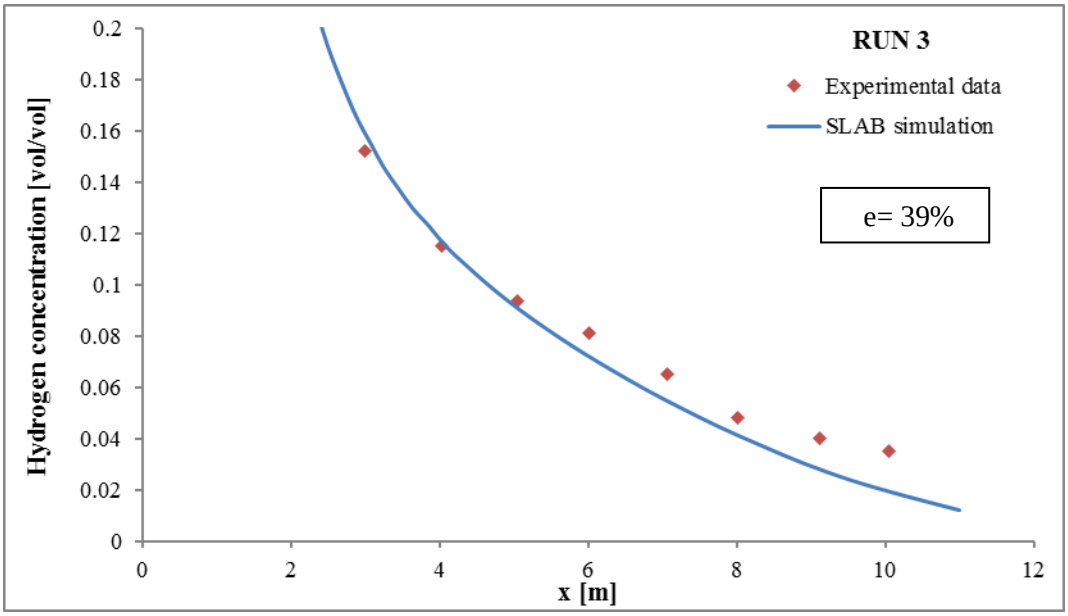

***Figure 3.5**: Comparison of hydrogen concentration (expressed in terms of volume fractions) vs distance between SLAB predictions and experimental data by* Shirvill et al. (2006) *in the conditions of RUN 3.*

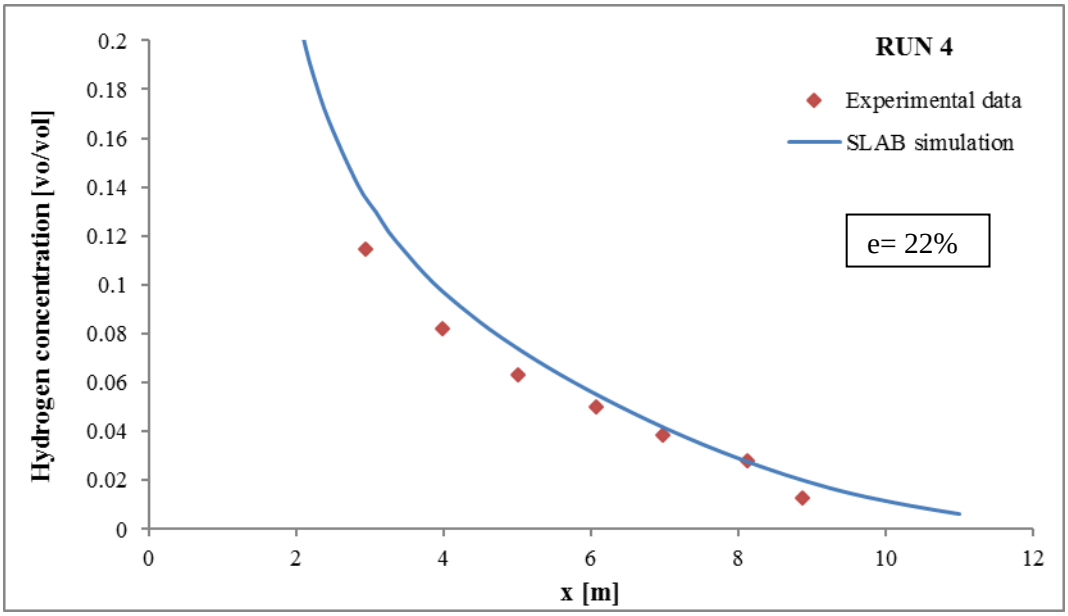

***Figure 3.6:** Comparison of hydrogen concentration (expressed in terms of volume fractions) vs distance between SLAB predictions and experimental data by Shirvill et al. (2006) in the conditions of RUN 4.*

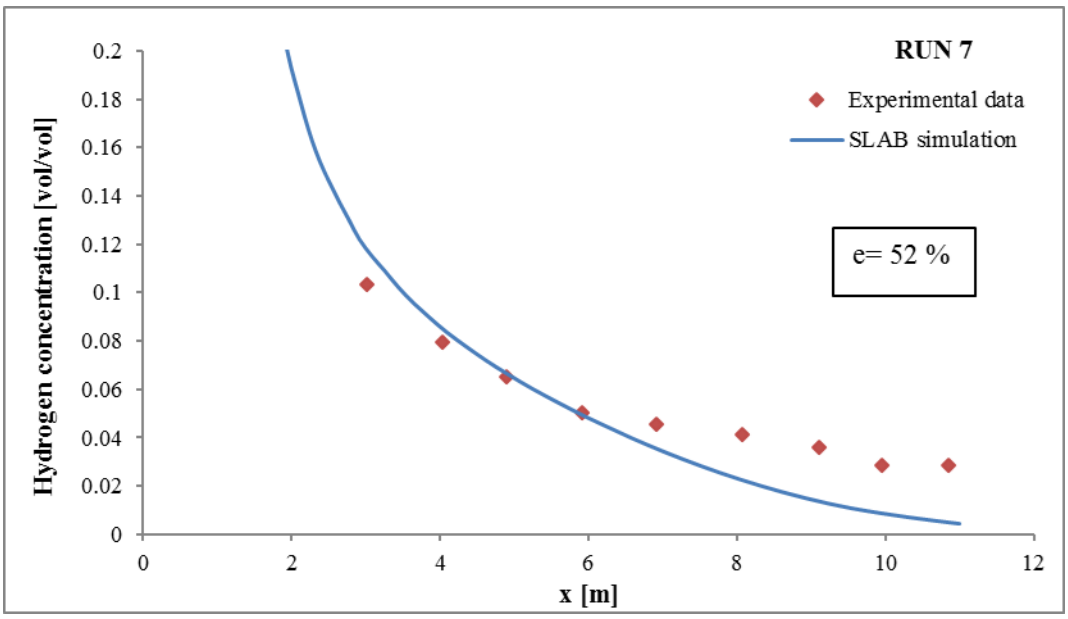

***Figure 3.7**: Comparison of hydrogen concentration (expressed in terms of volume fractions) vs distance between SLAB predictions and experimental data by Shirvill et al. (2006) in the conditions of RUN 7.*

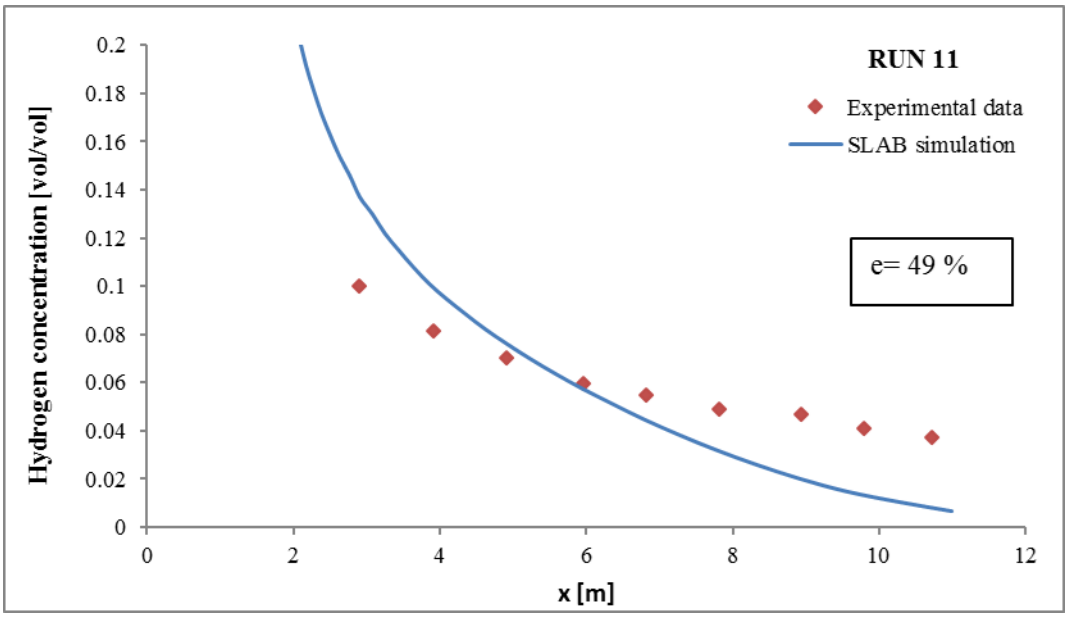

***Figure 3.8**: Comparison of hydrogen concentration (expressed in terms of volume fractions) vs distance between SLAB predictions and experimental data by Shirvill et al. (2006) in the conditions of RUN 11.*

A reasonable agreement between predictions and experiments has been shown in most cases considered. The prediction of the relative error (e), calculated through the Equation 3.8, has been evaluated.

$$e = \frac{100}{N_{exp}} \sum_{i=1,}^{N_{exp}} \left| C_{H_2-pred} - C_{H_2-exp} \right| / C_{H_2-exp} \quad (3.8)$$

As reported by the graphs, it is noted that the relative error is 39% for the Run 3, 22% for the Run 4, 52 % for the Run 7 and 49% for the Run 11. The data disagreement is due to the fact that the jet is affected by a crosswind during the experimental tests.

Another set of data used in the model validation are related to the experimental trials conducted by Han et al. (2014) to investigate the behaviour of high-pressure gaseous hydrogen released through small orifices.

The experimental setup, reported in Figure 3.9, consisted of a vessel containing hydrogen, on top of which a release hole was located. Three different hole diameters (0.5, 0.7 and 1 mm) were chosen and value of 100, 200, 300 and 400 bar have been taken into account as release pressure.

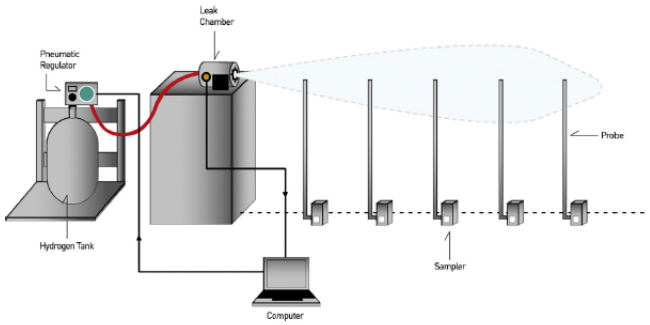

***Figure 3.9**: Experimental setup considered by Han et al.* (2014)

To analyse the dispersion characteristics, the hydrogen concentration was detected along the jet centreline, considered horizontal. A Nd-YAG laser sheet was used to visualize the hydrogen jet. The experimental conditions are summarized in Table 3.4.

Case	Pressure [bar]	Leak diameter [mm]
1	100	1
2	100	0.7
3	100	0.5
4	200	1
5	200	0.7
6	200	0.5
7	300	1
8	300	0.7
9	300	0.5
10	400	1
11	400	0.7

***Table 3.4**: Experimental conditions adopted by Han et al.* (2014)

SLAB simulations conditions are reported in Table 3.3.

Parameter	Assumptions
Source type	Horizontal jet release
Temperature of source material (K)	206 K
Continuous source duration (s)	12
Source height (m)	1
Concentration averaging time (s)	0.01
Maximum downwind distance (m)	10
Surface roughness height (m)	0.003
Wind velocity (m/s)	2
Height of wind measurement (m)	1
Ambient temperature (K)	288
Relative humidity (%)	75
Pasquill atmospheric stability class	6

***Table 3.5**: SLAB simulation parameters for experiments by Han et al. (2014)*

The comparisons of centreline hydrogen concentration decay as a function of distance are shown in Figure 3.10, 3.11 and 3.12 for a pressure release of 100, 200 and 300 bar, respectively, in the case of a leak diameter of 1 mm.

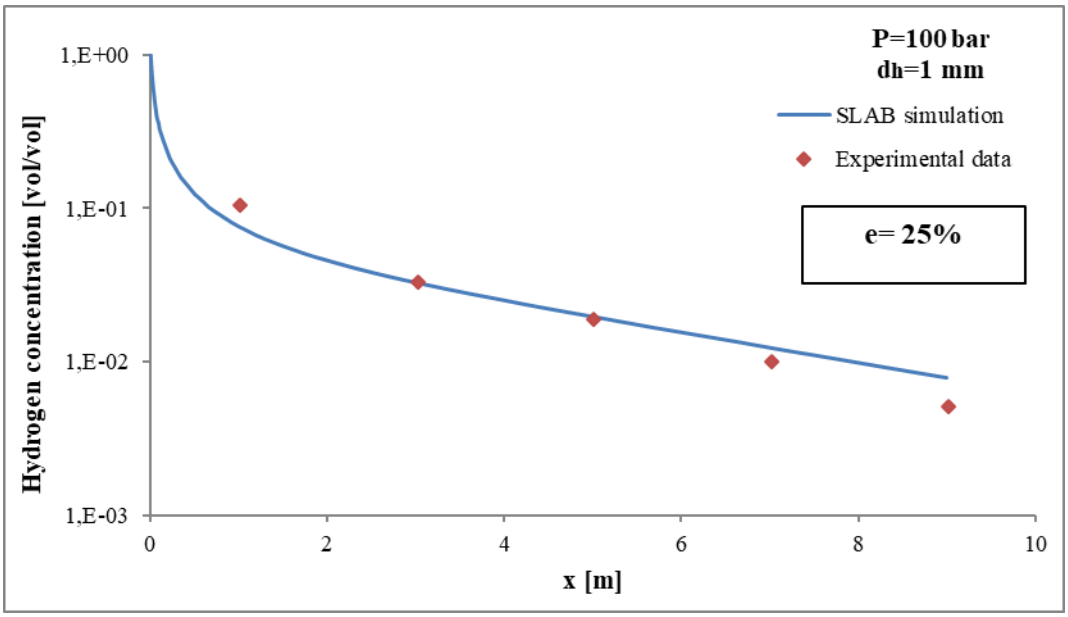

***Figure 3.10**: Comparison of hydrogen concentration (expressed in terms of volume fractions) vs distance between SLAB predictions and experimental data by Han et al (2014) (P= 100 bar, d_h=1 mm).*

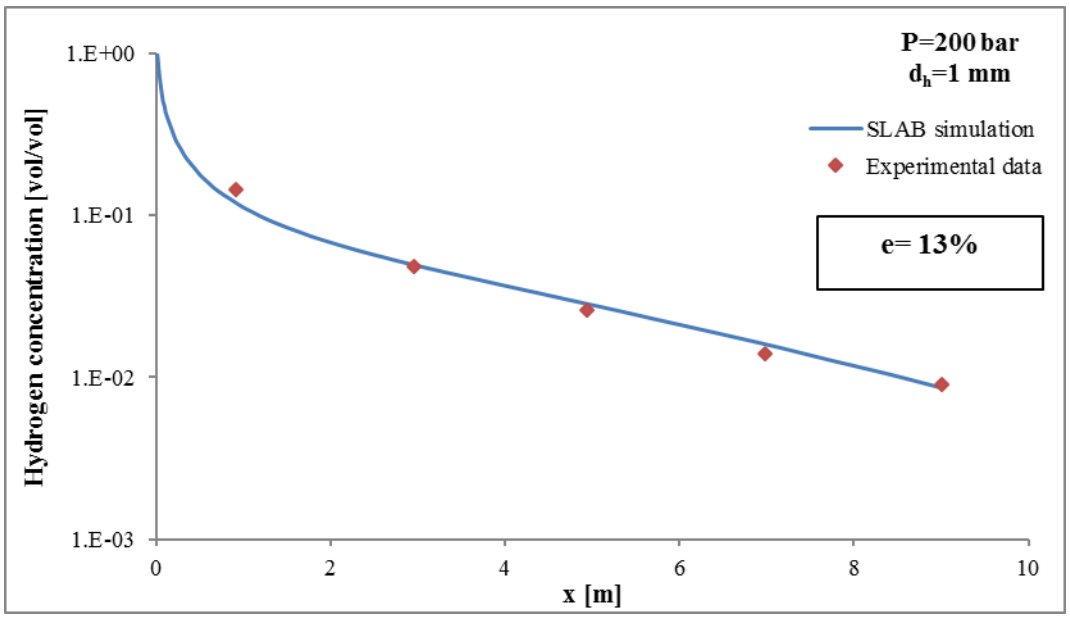

***Figure 3.11**: Comparison of hydrogen concentration (expressed in terms of volume fractions) vs distance between SLAB predictions and experimental data by Han et al. (2014) (P= 200 bar, d_h=1 mm).*

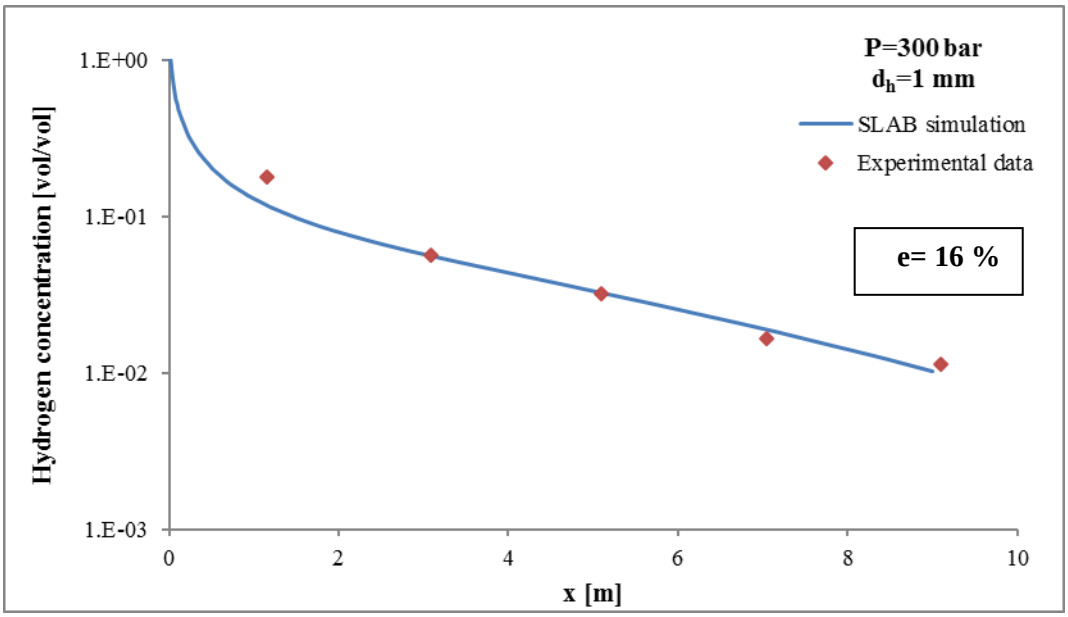

***Figure 3.12**: Comparison of hydrogen concentration (expressed in terms of volume fractions) vs distance between SLAB predictions and experimental data by Han et al. (2014) (P= 300 bar, d_h=1 mm).*

SLAB model predicts optimally experimental data in the conditions considered, summarized in Table 3.5. The fairly low values of the relative errors estimated (25%, 13% and 16%, related to a d_{hole} of 1 cm and pressure of 100, 200 and 300 bar, respectively) confirm this trend.

Therefore, the small discrepancies between the experimental measurements and the predictions could be due only to the viscous dissipation of the flow passing through a small hole.

Okabayashy et al. (2005) have carried out experimental tests to estimate the dispersion concentration range following a leakage involving hydrogen refuelling stations. Five high-pressure tanks, with a total volume of 2500 L, and containing gaseous hydrogen stored at 65 MPa and released to 40 MPa were used to perform the trials. Leakage from hole with diameter varying between 0.25 mm and 2 mm were analysed. Measurements of concentrations along the jet have been realized, considering stable wind conditions (1 m/s), and eight sensors located at different distances from the hole were employed.

Table 3.6 summarizes the SLAB conditions used in the simulations.

Parameter	Assumptions
Source type	Horizontal jet release
Temperature of source material (K)	205.34 K
Continuous source duration (s)	1
Source height (m)	1
Concentration averaging time (s)	0.01
Maximum downwind distance (m)	20
Surface roughness height (m)	0.003
Wind velocity (m/s)	0.2
Height of wind measurement (m)	1
Ambient temperature (K)	288
Relative humidity (%)	75
Pasquill atmospheric stability class	6

Table 3.6*: SLAB simulation parameters for experiments by Okabayasky et al. (2005).*

The comparison between simulated data and experimental data in the case of d_f= 2 mm and P=200 bar, is reported in Figure 3.13. As shown, simulation results reproduce experimental data reasonably, with a relative error of 28 %.

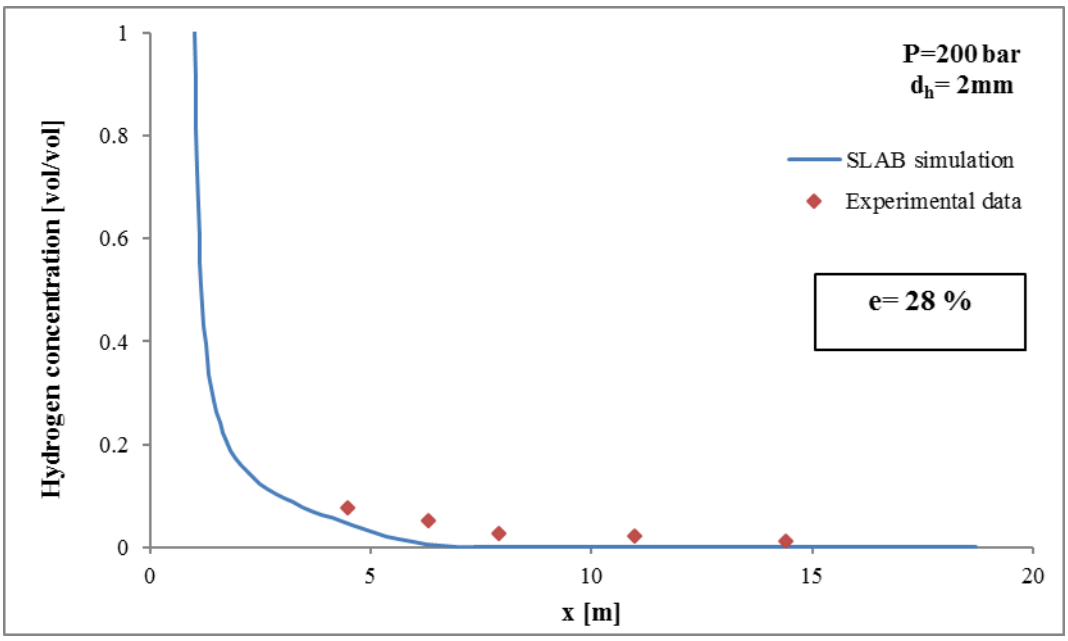

***Figure 3.13**: Comparison of hydrogen concentration (expressed in terms of volume fractions) vs distance between SLAB predictions and experimental data related to Okabayashy et al. (2005).*

This reproducibility of the data can also be seen in the simulations made in the other cases considered, whose simulation conditions are summarized in Table 3.6:

Finally, all the experimental results obtained were collected and reported in the Figure 3.14.

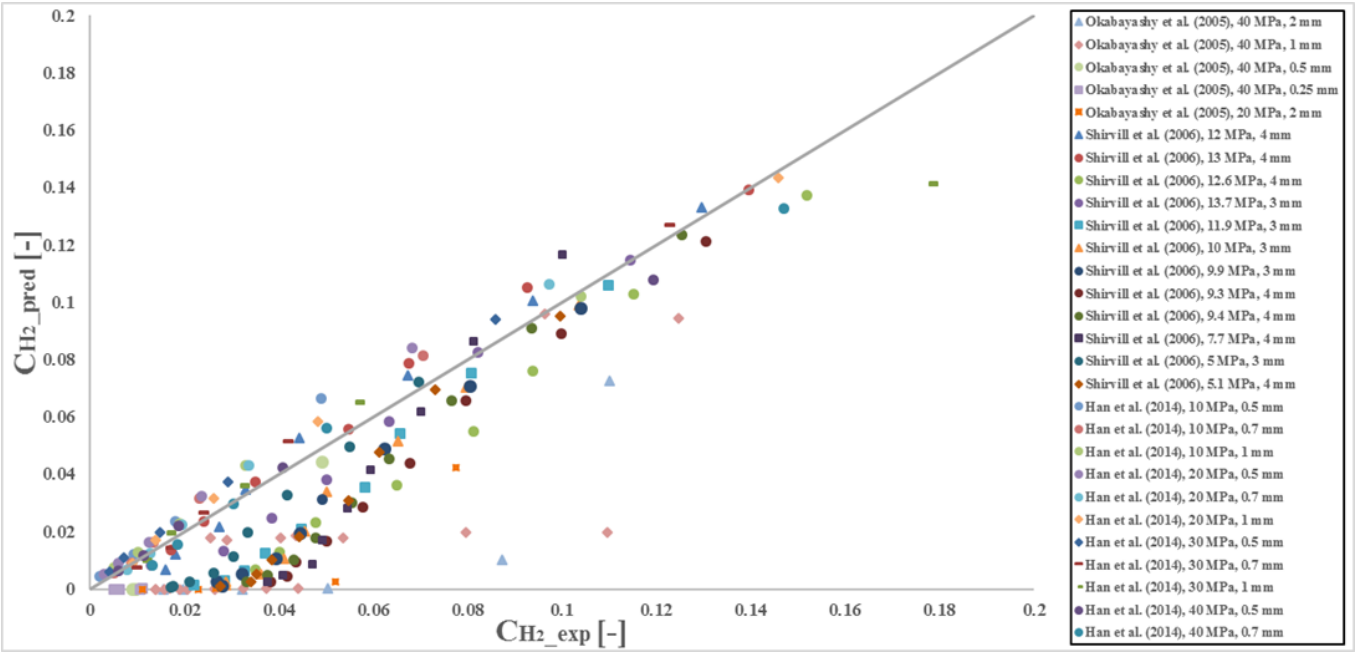

***Figure 3.14**: Predicted values of hydrogen concentration vs experimental values of hydrogen concentration, expressed in terms of volume fraction.*

A very effective graphical representation between simulated data and measured data is given by the graph shown in figure 3.14 where estimated values (C_{H2_pred}) against measured data (C_{H2_exp}) are reported. In this graph, it is possible to evaluate the dispersion of data around the right identity.

As shown, SLAB model underestimates some experimental data especially those by Shirvill et al. (2006).

The relative error, calculated through the Equation 3.8 is 45%.

Restricting the field of interest to concentrations greater than the lower flammability limit (4%), the relative error decreases considerably (e=30%).

3.4 Hydrogen explosions

Following an accidental release of a gas in the atmosphere, a vapour cloud is created and dispersed through the surrounding environment. The cloud will mix with air and the presence of a source of ignition can generate a fire or a vapour cloud explosions (VCE), if the ignition is immediate or delayed, respectively.

An explosion is defined as "a rapid expansion of gases resulting in a rapidly moving pressure or shock wave" (Crowl and Louvar, 2011).

The pressure variation as a function of time for a typical shock wave is represented in Figure 3.15:

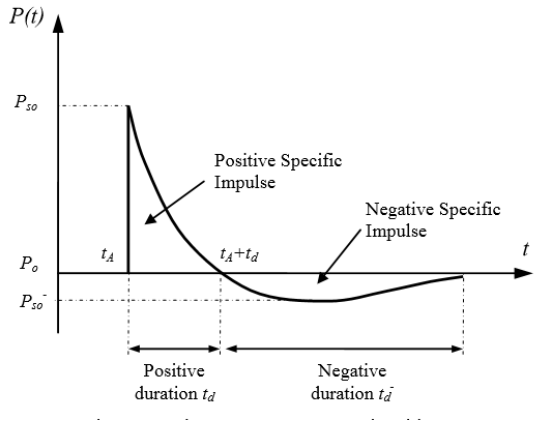

Figure 3.15: *Blast wave pressure at a fixed location*

As shown, when the arrival time (t_A) is reached, suddenly the pressure rises to a peak value of overpressure (P_{so}) with respect to the ambient pressure (P_0) and then decreases to the ambient level. A positive duration t_d and a negative duration t_{d-} can be identified, representative of a positive specific impulse and of a negative specific impulse, respectively.

3.4.1 Multi-Energy Method

The quantification of the main parameters of an explosion (overpressure and impulse) is evaluated using simplified models (i.e TNT equivalence, TNO Multi-Energy, Baker-Strehlow). These models are based on data relating to real accidental events.

The TNT method, although it is very simple to use, has not been taken into consideration for assessing the effects of the explosion, since it tends to overestimate the overpressure at the center of the gaseous cloud and to underestimate it as the distance from the cloud increases. It approximates the effects of the explosion of a gaseous cloud with those of a punctual explosion of a TNT charge which releases the same amount of energy. However, the main uncertainty in the use of this method lies in the estimate of the explosion efficiency. Few correlations exist between the quantity of combustion energy of a VCE and the equivalent weight of TNT required to model its blast effects.

The main assumption of the TNO Multi-Energy method (TNO is the acronym of Netherlands Organization for Applied Scientific Research) is that the level of congestion influences strongly the energy of the explosion, more than the amount of fuel present in the cloud (TNO, 2005). After identifying the confined volumes in the considered process and indicating the degree of confinement, the evaluation of the consequences of an explosion is carried out by consulting graphs showing semi-empirical curves, called “blast charts”. These graphs present a number representative of the curves of the blast strength in terms of positive phase duration and “side on” overpressure as a function of the combustion energy-scaled distance, as shown in Figures 3.16 and 3.17 (Crowl and Louvar, 2011).

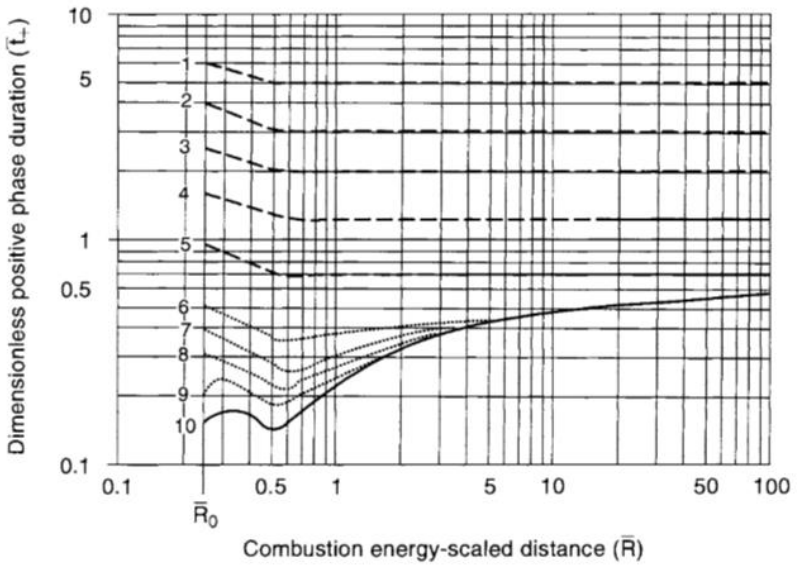

***Figure 3.16**: Sachs-scaled positive-phase duration for the TNO model by TNO (2005)*

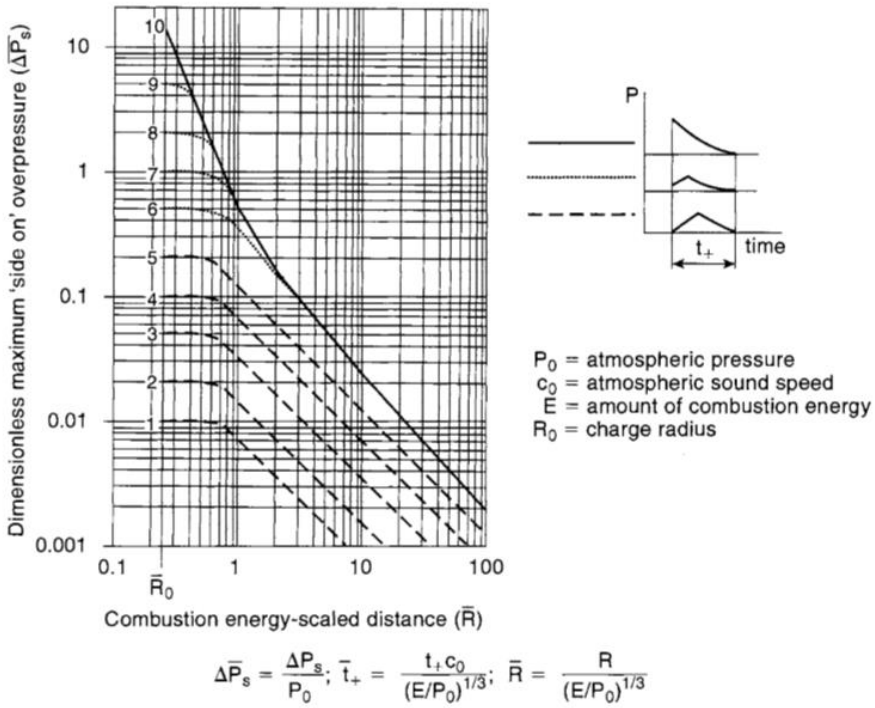

***Figure 3.17**: Sachs-scaled "side-on" overpressure for the TNO model by TNO (2005)*

The major difficulty in the use of this method is the choice of the class number, linked to the selection of different factors, i.e. ignition energy, obstacle density, degree of confinement. Some authors proposed some guidelines that help the user in the final decision on the choice of the class number. Kinsella (1993) suggested guidelines widely used in many safety

processes, but these do not consider the high reactivity of the fuel. Handling hydrogen, this aspect can not be overlooked.

In the case of hydrogen explosions, the positive overpressure and positive impulses have been evaluated in a comparison study between the use of TNO Multi-Energy and Baker-Strehlow-Tang (BST) methods by Melani et al. (2009). They have considered a considerable number of large-scale experiments, since both methods depend on the subjective choice of some parameters, the Mach number for the BST and the class number for the TNO, respectively. Results have shown that the TNO Multi-Energy method reproduces the experimental data in a better way than the BST method. However, while in the case of BST the choice of an appropriate Mach number is well directed, in the TNO method the choice of the class number is more subordinate to the decision of the single user. Some guidelines for choosing the class number for the application of the TNO Multi-Energy in the hydrogen explosions field have been suggested by the authors, in order to make the TNO Multi-Energy method application as objective as possible. They are reported in Table 3.7.

High fuel reactivity			
Ignition power	Obstruction	Volume (m^3)	Class number
Low (0 to 150 J)	0 to 1 %	≅ 5 to 2094	3
	1 to 15 %	5 to 300	5 or 6
	4.40 %	≅ 17	7 or 8
High (150 to 5.2 x 10^4 J)	0 %	300	9

***Table 3.7**: Guidelines for choosing the class number for the TNO Multi-Energy method applied to hydrogen explosion*

In this thesis, the TNO Multi-Energy method was incorporated, together with a release rate model, into the one-dimensional SLAB model, described above, in order to evaluate the dispersion process and any explosion that might result therefrom.

3.4.2 SLAB + TNO model for blast hazard evaluation

The consequences of gaseous hydrogen accidental releases from high-pressure pipeline were investigated developing a C++ code that incorporates the SLAB one-dimensional integral model. A release rate model (see equation (3.3) and (3.5)), pipeline operation properties (i.e. pipeline diameter, operating pressure) and source release properties (i.e. hole diameter, length of the pipeline from the compression station, wind velocity, atmospheric stability) are introduced in SLAB, to estimate the flammable vapour cloud. In order to calculate the

overpressure and impulse generated by a possible explosion, the TNO method is used and the data reported on blast charts are parameterized and incorporated in the C++ code.

In order to evaluate the blast probability, statistical data of the operative parameters and several information about the source release properties are needed.

The US Pipeline and Hazardous Material Safety Administration (PHMSA, 2016) provides data related to the hydrogen pipelines, about diameter, length and location of transmission and gathering lines. In addition, other details are found in literature (Bedel and Junker, 2006), as reported in Table 3.8.

Location	Pipe material	Years of operation	Diameter (mm)	Length (km)	Service pressure (MPa) and hydrogen purity (%)	Satus
AGEC, Alberta, Canada	Gr.290 (5LX X42)	Since1987	273 (Thickness: 4.8)	3.7	3.8 (99.9%)	Operational
Air Liquide, Texas/Louisiana, USA	API 5LX42, X52, X60 and other	?	76 - 356	390	5.1	Operational
Air Liquide, France, Belgium, Netherlands	Seamless Carbon steel	Since1966	Up to 304.8	879	6.5-10 (pure and raw H2)	Operational
Air Products, Houston, USA	-	Since1969	114.3 – 324	100	0.345 – 5.516 (pure H2)	Operational
Air Products, Louisiana	ASTM 106	?	101.3 – 304.8	48.3	3.447	Operational
Air Products, Sarnia	-	-	-	~3	-	Operational
Air Products, Texas	Standard natural gas line pipe (steel)	>10	114.3	8	5.5 (pure H2)	Operational
Air Products, Texas	steel, Schedule 40	>8	219	19	1.4 (pure H2)	Operational
Air Products, Netherlands	-	-	-	45	(flow rate : 50 t/day)	Operational
South Africa	-	-	-	80	-	-
Chemische Werke Huis AG, Ruhr, Germany	Seamless equipment to SAE 1016 steel	Since1938	168-273	215	Up to 2.5 (pure H2)	Operational
Cominco B.C., Canada	Carbon Steel (ASTM 210 seamless)	Since1964	5 (Thickness: 0.8)	6	>30 (62-100 %)	Stand-by
Gulf Petroleum Cnd, Petromont – Varrnes	Carbon Steel, seamless, Schedule 40	-	168	16	93.5% H2-7.5% CH4	Operational
Hawkeye Chemical, Iowa	ASTM A53 Gr. B	3	152.4	3.2	2.8	Operational
ICI Billingham, UK	Carbon Steel	-	-	15	30 (pure H2)	-
LASL, New Mexico	ASME A357 Gr. 5	-	25.4	6.4	13.8	Abandoned
Los Alamos, New Mexico	5Cr-Mo (ASME A357 Gr. 5)	>8	30	6	13.8 (pure H2)	Abandoned
Linde, Germany	-	-	-	1.6 – 3.2	-	-
NASA-KSC, Florida	Stainless steel 316 (austenitic)	>16	50	1.6-2	42	Operational
NSA-MSFC, Alabama	ASTM A106-B	-	76.2	0.091	34.5	Abandoned
Philips Petroleum	ASTM A524	4	203.2	20.9	12.1 – 12.8	Operational
Praxair, Golf Coast, Texas, Indiana, California, Alabama, Louisiana, Michigan	Carbon Steel	-	-	450	H2 commercial grade (14 M Nm3/day)	Operational
Rockwell International S.	Stainless steel -116	>10	250	-	>100 (ultra pure H2)	-

***Table 3.8**: Main features of hydrogen pipelines around the world related to a study carried out by Bedel and Junker (2006)*

Studies carried out by Air Liquide (2005) allowed the determination of the probability of hydrogen pipeline failure. It was estimated that the pipe rupture frequency per length of pipeline is 0.126/year per 1,000 km.

As regards the frequency of different leak sizes and their relative probability, detailed information is collected in the report of European Gas Pipeline Incident Group (EGIG, 2015). Depending on the leak size diameter, small, medium and rupture breaches are defined. When the diameter of the hole (d_{hole}) is smaller than or equal to 0.02 m the breach is considered small (pinhole/crack); when the diameter of the hole is larger than 0.02 m and smaller or equal to the diameter of the pipe, the breach is classified as medium. Finally, when the hole diameter is larger than the pipe diameter, this is identified as a rupture. The relative

probabilities evaluated are 48% for small failure, 39% for medium ones and 13% for a full rupture of the pipeline.

Statistical data are employed in the simulations that are run by varying the parameters mentioned above in the following ranges: d= 0.1016-0.508 m, P_0= 649-12800 kPa, L= 50-10000 m, R= 10-2000 m, d_{hole}=0.02 m-d. In particular, the total breakage of the pipeline was also considered, at which corresponds the greatest release flow rate.

SLAB simulation conditions used in the model are summarized in Table 3.9.

Parameter	Assumptions
Source type	Horizontal jet release
Temperature of source material	200 K
Continuous source duration	600 s
Source height	1 m
Concentration averaging time	10 s
Maximum downwind distance	300 m
Surface roughness height	0.003 m
Wind velocity	2-5 m/s
Height of wind measurement	10 m
Ambient temperature	285 K
Relative humidity	75%
Pasquill atmospheric stability class	A, C, D, F

Table 3.9: *SLAB simulation parameters.*

The gas release jet is assumed horizontal, considering this one as the worst-case scenario with respect to the vertical one, since the gas disperses less quickly. The jet is located at 1 m above the ground level.

The source conditions are related to the conditions of the material after it has fully expanded, adiabatically. The temperature of source material (T_s) is calculated according to the Equation 3.9, proposed by SLAB:

$$T_s = \left(\frac{1}{\gamma}\right) \times \left[1 + (\gamma - 1)\left(\frac{P_a}{P_0}\right)\right] \times T \qquad (3.9)$$

in which γ is the specific heat ratio, P_a is the atmospheric pressure, P_0 and T the operative pressure and temperature, respectively.

Firstly, several simulations were carried out to define the dispersing cloud extensions and, consequently, a value of 300 m has been assumed as a maximum downwind distance, in order to correctly define the computational domain.

Pasquill atmospheric stability classes (Pasquill, 1961), denoted as A (extremely unstable), C (slightly stable), D (neutrally stable) and F (moderately stable) were used in the simulations and two values of wind velocity, 5 and 2 m/s, were taken into account. It was assumed that the wind direction is parallel to the gas jet. Both classes related to night (A and C) and daily (D and F) atmospheric conditions were analysed, since the dispersion is influenced by several factors (i.e. air humidity, temperature). Furthermore, a conservative approach led to investigate the worst-case scenario for the weather condition (F2) too.

Finally, in order to evaluate the potential explosive behaviour of the hydrogen in these conditions, two explosivity classes, 6 and 9, are employed in the TNO method. These classes differ in the ignition power, low in the case of class 6, high in the case of class 9 (see Table 3.7).

Preliminary simulations allowed the determination of the range of values of overpressure and impulse obtained in the cases taken into consideration. According to these results, 17 classes of overpressure and 13 classes of impulse were chosen. A range of values of overpressure and impulse defines each of these classes, whose mean value is indicative of each class of overpressure and impulse. The values are reported in Table 3.10:

Class	**Overpressure (kPa)**		**Impulse (kPa * ms)**	
	Range	**Mean**	**Range**	**Mean**
1	101-102.99	1	1-249	125
2	103-104.99	3	250-449	350
3	105-108.99	6	450-499	500
4	109-112.99	10	500-999	750
5	113-116.99	14	1000-1999	1500
6	117-121.99	18	2000-2999	2500
7	122-127.99	24	3000-3999	3500
8	128-133.99	30	4000-4999	4500
9	134-139.99	36	5000-9999	7500
10	140-169.99	54	10000-14999	12500
11	170-199.99	84	15000-19999	17500
12	200-239.99	119	20000- 39999	30000
13	240-299.99	169	40000- 79999	60000

14	300-399.99	249	-	-
15	400-549.99	374	-	-
16	550-607.775	478	-	-
17	607.776-608.8	507	-	-

***Table 3.10**: Classes of overpressure and impulse*

3.5 Damage to structural components: Blast fragility

Explosions can cause damage to the structural components of buildings in the vicinity of the accidental event.

The assessment of the effects of a blast wave on a structure requires considerations about the loading and the response of the structure to the loading. The loading is defined as the force arising from the blast wave acting on the structure (Crowl, 2003). Depending on the loading, the response of the structure can be different; it can occur a collapse of the entire structure or a partial destruction. Figure 3.18 depicts the interaction of the shock wave with a rigid structure. The shock wave can interact with the structure directly (Figure 3.18 (1)) or can hit the front of the structure (Figure 3.18 (2)), generating a reflected shock wave that leads to an overpressure. The shock wave achieved when a reflected shock occurs is greater than the incident side-on one, the values of the reflected overpressure are lower than the incident side-on overpressure ones, instead. The reflected wave travels to the ends of the structure and diffracts on the side of the structure (Figure 3.18 (3)). Different intensity of force can be caused by the vortices created. Drag forces due to the transient blast wind act on the structure, also (Figure 3.18 (4)).

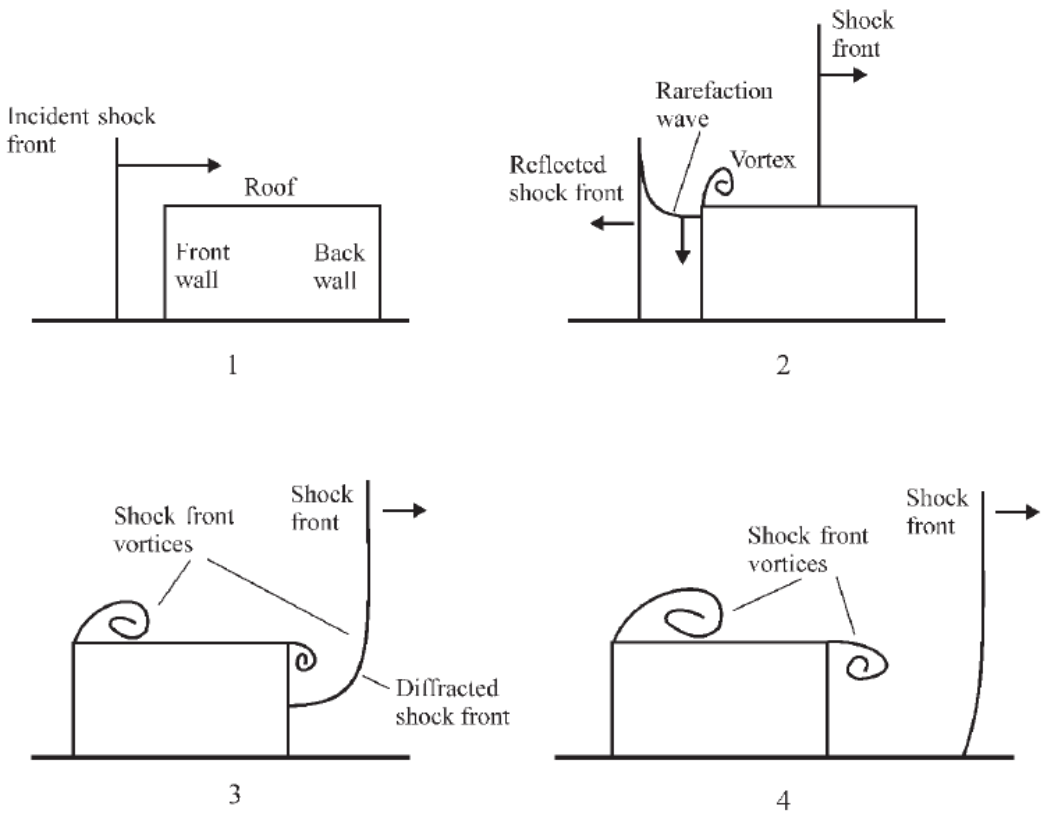

Figure 3.18: *Interaction of a blast wave with a rigid structure (Crowl, 2003)*

Depending on the strength and mass of the structure, on the ductility of the materials of construction, the response of the structure to the blast wave can be different.

An efficacious method that allows the prediction of the behaviour of the structures involved in an explosion is represented by the use of the pressure-impulse diagrams. Typically, two methods are taken into consideration to estimate these kinds of damage: pressure-impulse diagrams and nonlinear dynamic analysis of single-degree-of-freedom (SDOF) systems. While the SDOF systems permit to capture a single failure mode of real physical objects, the pressure-impulse diagrams consider several failure modes (e.g. shear, flexural, mixed flexural-shear) in an integrated manner.

Pressure-impulse diagrams are obtained from data of either numerical simulations, experimental tests or numerical-experimental procedures.

They correlate a specific damage level to a combination of overpressures and impulse, involving a particular structural element (Ngo et al., 2007) and are associated with the peak response and its relative damage or, in a more simplified approaches, with the estimation of the collapse pressure. The collapse pressure, defined as the peak overpressure that produces damage in quasi-static conditions, is a parameter often taken into account in the structural

safety and it is assumed as the threshold value for the collapse, as considered in a several building design codes (e.g. Eurocode 1-Part 1-7 (2006) and Italian Building Code (DM, 2018)).

In this thesis, in order to evaluate their failure mode, the behaviour of two different kinds of structural components are analysed with pressure-impulse diagrams: reinforced concrete (RC) columns and tuff stone masonry (TSM), that represent typical structural elements of Euro-Mediterranean modern and ancient buildings, respectively.

Iso-damage curves, that are the graphical representation of critical combinations of peak overpressure (P) and impulse (I) that cause the same level of blast damage, are reported on pressure-impulse diagrams. Based on the type of structural component and on its typical failure manner, different damage measures (DMs) allow the quantification of the level of blast damage.
The hyperbolic curves drawn on the P-I diagrams are defined by the following equation:

$$(P - P_0)(I - I_0) = \alpha \left(\frac{P_0}{2} + \frac{I_0}{2}\right)^{\beta} \quad (3.10)$$

in which: P_0 and I_0 are the overpressure and the impulse asymptotes, respectively; α and β are constants. These parameters are chosen taking into consideration several elements, i.e. the geometrical and mechanical aspects of the structural building component and the threshold level of damage. Furthermore, in the P-I diagrams it is possible to identify two regions, one concerning the safety conditions, the other one the failure conditions, depending on the DM selected and the DM value that represents the level of blast damage. The safety region is located below in the P-I diagram, while the failure conditions are defined considering three regions of structural behaviour (quasi-static, dynamic and impulsive loading), depending on the duration of the pressure-time history of blast loading compared to the natural vibration period of the structural component.
Failure results when the peaks of overpressure and impulse reach the pressure asymptote P_o and the impulse asymptote I_o in the quasi-static conditions and impulsive loading, respectively.
An intermediate structural response is obtained in the dynamic blast loads region, in which the failure takes place when the peaks of overpressure and impulse reach one of the critical combination in the P-I diagrams.

3.5.1 Reinforced concrete columns

Literature data suggest values of 12 and 1.5 for the constant α and β, respectively, concerning the blast capacity of reinforced concrete (RC) columns (Shi et al., 2008). Validation of these values against experimental data has been performed (Woodson et al., 1999, 2000).

Concrete is a mixture of cement paste and a conglomerate. The cement is composed of limestone, sand or clay, bauxite and iron. In order to improve the tensile strength of concrete, steel bars are added and the reinforced concreate is obtained.

A dimensionless parameter (the damage index, D) is used to describe the limit level of blast damage:

$$D = 1 - \frac{N_{uR}}{N_{uD}} \tag{3.11}$$

where N_{uD} and N_{uR} are the initial and the residual axial load-bearing capacities of the RC column, respectively.

The D index, ranging between 0 and 1, allows the definition of the structural capacity loss.

P-I diagrams, in which pressure and impulse asymptotes rise with the level of axial capacity loss, selected for structural safety verification, are a useful tool to determinate the blast capacity of RC columns.

A study carried out by Parisi (2015) is taken into consideration to evaluate the blast capacity of RC columns. P-I diagrams with a uniform probability of failure, i.e. the same probability of overcoming a threshold level of damage, D_{LS}, (indicating with LS the limit state used for performance design or analysis) are considered.

Three levels of damage are proposed in these probabilistic P-I diagrams:

- D_{LS}= 0.2 corresponding to a minor damage
- D_{LS}= 0.5 corresponding to a moderate damage
- D_{LS}= 0.8 corresponding to near collapse

A pressure-impulse diagrams of a RC column at multiple damage levels are shown in Figure 3.19:

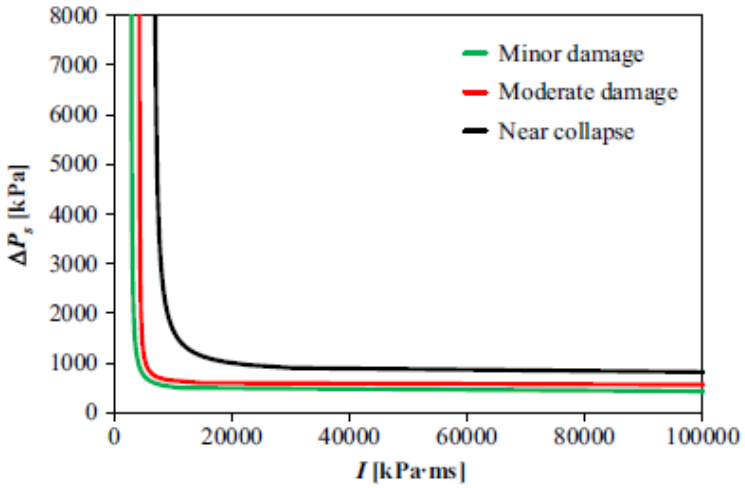

***Figure 3.19**: Pressure-impulse diagrams of RC column at multiple damage levels.*

The asymptotes into Equation 3.10 depend on several properties of the column. In this thesis, typical RC columns designed for gravity-loads buildings according to past (non-seismic) Italian codes are chosen. Columns with a concrete cover c=30 mm and nominal height H=3.00 m, a usual value for inter-storey height in residential buildings, were investigated. It was decided to consider the pressure-impulse diagrams related to the condition near collapse of RC columns, because the near collapse of RC columns can lead to big losses as a consequence of a progressive collapse of the building structure (Adam et al., 2018; Brunesi and Parisi, 2017).

In the Figure 3.20 the P-I diagrams for two types of columns are reported: gravity-loads designed columns and earthquake-resistant columns, respectively. As shown, the curve related to the gravity-loads designed columns is lower than the earthquake-resistant one and this reveals a better behaviour of the RC columns, in terms of resistance. Typical gravity-load designed columns used in Italy in the RC buildings are taken into account: i) concrete strength class C20/25, considering that 20 and 25 are the cylinder and cube characteristic compressive strengths of concrete, respectively; ii) steel type FeB44k, approximately corresponding to the current B450C, characterised by ribbed bars and squared cross section with size 300×300 mm^2.

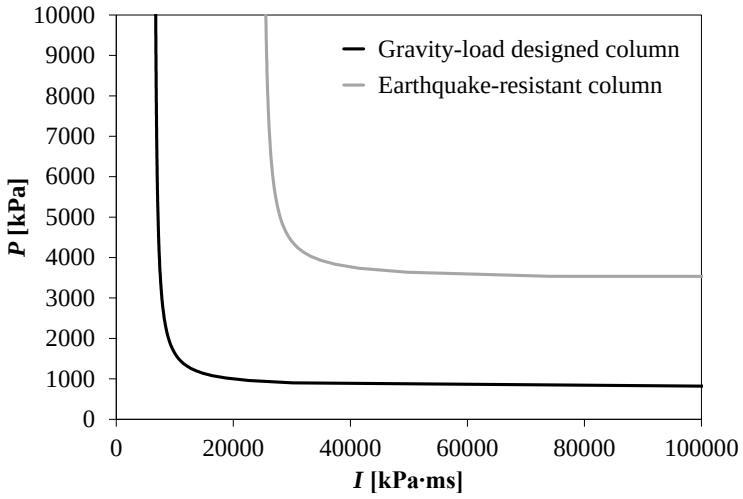

***Figure 3.20**: Median pressure-impulse diagram of RC associated with a near collapse*

3.4.2 Tuff stone masonry walls

Tuff stone load-bearing walls, characterizing the masonry buildings, can be affected by flexural out-of-plane failure, following an explosion. Compared to RC columns, these walls have a less compressive strength, a less capability of tolerating tensile stresses and a different response sensitivity to axial loading.

Tuff stone masonry (TSM) walls considered in this study present the following characteristics: height h_w = 3.00 m, slenderness ratio λ= 10 and pre-compression level P_v/f_m = 25% , considering that λ is the ratio between h_w and thickness t_w (supposed to be 300 mm); P_v is the average compressive stress due to gravity loads and f_m is the peak compressive strength of masonry.

The P-I diagram reported in Figure 3.21 shows the effect of pre-compression levels on the blast resistance of TSM walls, highlighting that a higher value of pre-compression level improves the blast resistance of TSM walls, where low pre-compression levels present a $P_v/f_{m=}$ 10%, and for medium and high pre-compression levels P_v/f_m equals to 25% and 50%, respectively.

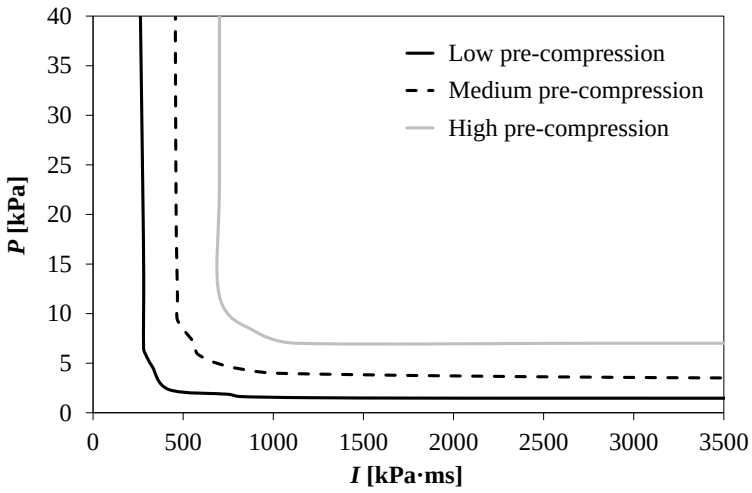

Figure 3.21: *Pressure- impulse diagrams for different pre-compression levels*

Since high pre-compression levels are rarely achieved, a medium pre-compression level, reached typically in load-bearing walls located at the ground floor, has been chosen.

The assessment of the structural failure of TSM walls, considering the material deformations and the modest strength of masonry, both in tension and shear sliding, has been carried out investigating selected P–I diagrams derived through nonlinear dynamic analysis of elastic finite element models with tie-break resisting force, according to a previous study by Parisi et al. (2016). TSM walls with material density ρ= 1360 kg/m3; Poisson's ratio ν= 0.25; Young's modulus E = 2159 MPa; and peak compressive strength f_m = 3.96 MPa, were taken into consideration.

3.6 Comparison between hydrogen and natural-gas pipelines

The methodology proposed in section 3.3.2 has been employed taking into consideration also pipelines carrying out natural-gas in order to realize a comparison with hydrogen pipelines.

The same SLAB input parameters have been assumed (i.e. horizontal jet release, atmospheric conditions, surface roughness) (Russo, 2014, 2016).

The atmospheric stability classes A, C, D and F and wind velocity in the range 2-30 m/s were analysed.

Similarly, to the approach adopted in the case of simulations performed for hydrogen, statistical data on pipeline operations properties (i.e. pipe diameter, operating pressure) were required (EGIG, 2011). Values of operative pressure between 2000 and 8500 kPa and pipe diameters ranging between 0.127 and 1.257 m were assumed. As regards the pipeline length

from the gas supply station to the release point (L) as well as the distance to the centre of explosions (R), the same ranges used for the hydrogen simulations were considered (L= 50-10000 m, R=10-2000 m).

From the analysis of literature, it results that the mean annual failure rate of natural-gas pipeline is 0.351 per 1,000 km/year (EGIG, 2011) and this value was used in the simulations.

3.7 Damage to people involved in an explosion

The overpressure generated by explosion, following a hydrogen pipeline accidents, can pose several damages to people in the proximity.

It is usual to distinguish the effects of explosions in direct and indirect effects. In fact, a sudden change in pressure can damage the pressure-sensitive organs, such as lungs and ears (main direct effect) (HyResponse, 2016 (a)). However, people can be also indirectly damaged, hit by fragments either connected with the equipment damage or structure collapse or thrown away by overpressure and, subsequently, impacting stationary objects or structures (TNO, 1989). All these effects can cause damage in terms of injury or fatality.

Commonly, the consequences of an accident event are evaluated using a probability of harm to people, based on a harm criterion (La Chance, 2011).

A particularly convenient method to estimate the level of harm to people, following an accident event, and to quantify the exposure in terms of its intensity, duration and consequences, uses the Probit Functions (Probability unit), characterizing the dose-effect relationship (TNO, 1989; Crowl, 2011; HSE, 2013). A dose level (V) is transformed into a probability of injury or fatality with the Probit Function. Equation 3.12 allows the evaluation of the Probit variable Y (Crowl, 2011):

$$Y = k_1 + k_2 \ln V \tag{3.12}$$

in which k_1 and k_2 are empirical constants related to a specific hazard and V is the causative factor, representing the dose. Then, the following equation is used to perform the conversion from Probit to percentage:

$$P = 50\left[1 + \frac{Y-5}{|Y-5|}\, erf\left(\frac{|Y-5|}{\sqrt{2}}\right)\right] \tag{3.13}$$

where erf is the error function. This equation expresses the percentage of people that suffers a particular damage. Different Probit functions are available in the literature, representative of relevant considered damage, as listed in Table 3.11.

Damage	Probit Equation
Death due to lung haemorrhage (Eisenberg, 1975)	$Y= -77.1+ 6.91 \ln [P_s]^a$
Death due to lung haemorrhage (HSE, 1991)	$Y= 1.47+ 1.371 \ln [P_s]^a$
Death due to lung haemorrhage (TNO, 1989)	$Y= 5- 5.74 \ln [4.2 P_a/P_{ef} +1.3/I_{sc}]^b$
Death due to head impact (TNO, 1989)	$Y= 5- 8.49 \ln [2430/P_s +4 x10^8/P_s I]^c$
Death to whole body impact (TNO, 1989)	$Y= 5- 2.44 \ln [7380/P_s +1.3 x10^9/P_s I]^c$
Injuries due to impact (Eisenberg, 1975)	$Y= -39.1+ 4.45 \ln [I]^d$
Injuries due to eardrum ruptures (Eisenberg, 1975)	$Y= -15.6+ 1.93 \ln [P_s]^a$
Death due to impact (Eisenberg, 1975)	$Y= -46.1+ 4.82 \ln [I]^d$
Injuries due to eardrum ruptures (TNO, 1989)	$Y= -12.6+ 1.524 \ln [P_s]^a$
a: P_s= peak overpressure [Pa] b: P_a= atmospheric pressure [Pa], $I_{sc} = I/ (P_a^{1/2} x m^{1/3})$, m= mass of person=70 kg, P_s= peak overpressure [Pa], $P_{ef} = P_s + 5 x P_s^2/ (2 x P_s +1.4 x 10^6)$ c: P_s= peak overpressure [Pa],I= impulse of the shock wave [Pa x s] d: I= impulse of the shock wave [Pa x s]	

***Table 3.11**: Probit functions for damage caused by explosion*

Since it is more accurate to use models that provide a probability of damage as a function of the peak overpressure and the correlated impulse, TNO Probits have been chosen to evaluate the probability of harm to people (TNO, 1989). Furthermore, in the Probit equation related to the deaths due to lung haemorrhage, the causative variable is represented by a combination of overpressure, impulse and dynamic pressure (P_{ef}) and mass of person, fixed at value of 70 kg.

Several national and international sources, incorporating codes, guidelines and best practices, provide harm criteria. In Table 3.12 the harm effect to people from overpressure and impulse are listed, as reported in literature.

Effects on people	Ps [kPa]	I [kPa x ms]
Death from lung haemorrhage	82.7 – 103.4 (a)	180 (b)
Death from head impact	55.16 (c)	-
Death from whole-body displacement	75.84 (d)	370 (b)
Injuries from ear-drum rupture	13.8 (a)	-

(a) Jeffries et al., 1997
(b) NFPA, 2011
(c) AIChE, 1999
(d) Federal Emerg. Manag, agency, 1987

***Table 3.12**: Threshold harm criteria*

Higher threshold values of overpressure (82.7-103.4 kPa) are imposed in the case of death due to lung hemorrhage, as reported in Jeffries et al. (1997).

Furthermore, a distinction must be made between people located inside a building and people located in the open air. In fact, following the collapse of the structural components of a building, people can suffer indirect damage.

Finally, in order to mitigate the consequences of an accidental event involving hydrogen high-pressure pipeline, opportune distances between the source of risk and the target (people or structures) might be established.

Safety distances are defined as "the minimum separation between a hazard source and an object (human, equipment or environment) which will mitigate the effect of a likely foreseeable incident and prevent a minor incident escalating into a larger incident" (EIGA, 2015).

3.8 Hydrogen Jet Fires

The accidental release of high-pressure gaseous hydrogen can also result in a jet fire, which could lead to a series of disastrous events.

Jet fires typically arise from the combustion of a gas or a liquid released from a pressurized process unit. Depending on leakage diameter and source pressure, turbulent hydrogen-jet flames resulting from ignition of accidental releases can pose hazards associated with

radiation. Knowing the flame length and the resulting radiative heat flux is an important aspect related to safety.

3.8.1 Flame length and validation of the SLAB model

Generally, the definition of the experimental flame length is based on the visible flame and it is estimated through a simple observation or analysing photographs of the flame emissions (Schefer, 2007).

The flame length is defined as the horizontal distance from the nozzle outlet to the visible flame top (Imamaura et al., 2008). The flame length (L_f) and the flame width (W_f) are the parameters that represent the flame shape, as illustrated in Figure 3.22:

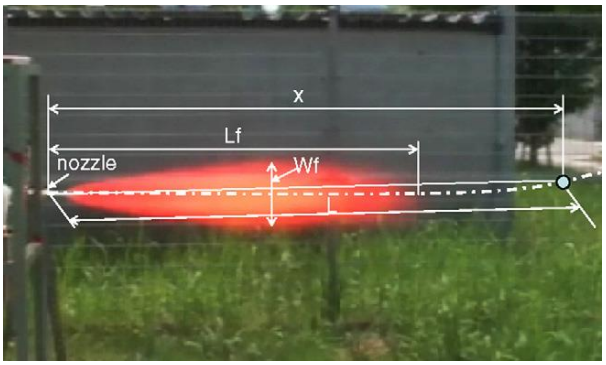

***Figure 3.22**: Parameters that characterize the flame shape: flame length (L_f) and flame width (W_f) (Imamaura et al, 2008)*

Numerous parameters help to define the features of the flame length and they may be taken into consideration in order to estimate the damage caused by a jet fire from a hydrogen release.

Schefer et al. (2006, 2007), performing various experiments, taking into account vertical jets, arising from high-pressure sources up to 413 bar and nozzle diameters ranging between 1.91 and 7.94 mm, demonstrated that the flame length linearly decreases with the mass flow rate, which decreases as the pressure is reduced. They confirmed that the ratio of the measured flame width to length is approximately 0.17, as reported in literature (Turns and Myhr, 1991).

Imamaura et al. (2008) investigated the thermal properties of hydrogen jet flames and confirmed the dependence of the flame length on the nozzle diameter, mass flow rate and release pressure. Experiments are carried out on horizontal jets, taking into consideration nozzle diameters ranging between 1 and 4 mm and spouting pressures up to 3 MPa. The flame length observed was proportional to the value of $P^{0.4\text{-}0.5}$ and $m^{0.4\text{-}0.5}$.

Experimental measurements carried out by Mogi et al. (2009) on flame arising from horizontal jets highlighted that the flame length is proportional to the spouting pressure when it is higher than the critical pressure, otherwise, i.e. when the spouting pressure is lower than the critical pressure, the flame length is about constant. Release pressure up to 40 MPa and nozzle diameters varied from 0.1 to 4 mm are investigated. The flame size obtained was proportional to the nozzle diameter and to the spouting pressure with a factor of 0.43.

In literature, several correlations for the determination of the flame length (L_f) and width (W_f) have been proposed.

Iwasaka et al. (1979) proposed the empirical formulas reported below (Equation 3.14 and 3.15), as a function of the release pressure P and of the hole diameter d_{hole}:

$$\frac{L_f}{d_{hole}} = 544 \times P^{0.384} \tag{3.14}$$

$$\frac{W_f}{d_{hole}} = 78.7 \times P^{0.451} \tag{3.15}$$

The previous relationships are validated only for spouting pressure up to 10 MPa.

The experimental equations proposed by Mogi et al. (2009), instead, covers values of spouting pressure ranging between 0.01 MPa and 40 MPa and hole diameter between 0.1 and 4 mm (Equation 3.16 and 3.17):

$$\frac{L_f}{d_{hole}} = 524.5 \times P^{0.436} \tag{3.16}$$

$$\frac{W_f}{d_{hole}} = 85.1 \times P^{0.436} \tag{3.17}$$

According to the literature (HyResponse, 2016 (a)), in this thesis, the flame length has been evaluated as the distance from the nozzle to an axial location (x) where the hydrogen concentration is 4% (corresponding to the LFL). The profile of hydrogen concentration as a consequence of a release jet is calculated with the integral model SLAB.

The ability of the SLAB model to predict hydrogen concentration at different distances from the release has already been analysed (see paragraph 3.3.1). Herein it is reported a comparison between the flame lengths evaluated with SLAB and experimental data available in literature relevant to horizontal jets. Experimental data provided by Mogi et al. (2009) and Proust et al. (2011) have been considered. Mogi et al. (2009) carried out trials in a range of pressure from 4 to 35 MPa and hole diameter varied from 0.1and 4 mm. The experiments of Proust et al. (2011) are related to pressure from 900 to 1 bar and diameter between 1 and 3 mm.

In addition, a comparison between the flame lengths calculated through literature correlations (Equation 3.14 and 3.16) and experimental data has been carried out, too.

The results are reported in Figure 3.23:

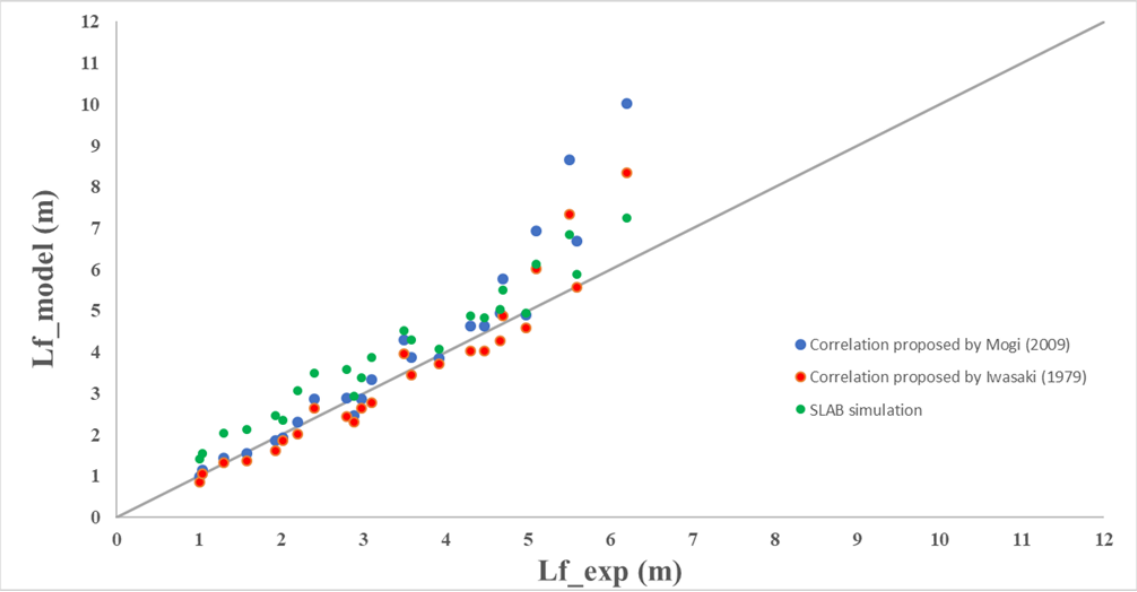

***Figure 3.23**: Comparison of flame length evaluated with SLAB and with literature correlations (Eq. 3.14 and 3.16) and experimental data*

From the analysis of the results, a good agreement between calculated and experimental data is observed, especially for the lowest values of pressure. However, SLAB tends to overestimate the experimental data, while the correlation proposed by Iwasaki tends to

underestimate them. The calculated relative error (e=23 %) confirms that the SLAB model reproduces the experimental data quite accurately. The major deviations are related to experimental data obtained at a pressure of 700 and 500 bar. However, the operative conditions adopted in this work do not cover this range of pressure.

3.8.2 Radiative heat flux: literature review

The first way to transfer heat to the surrounding area by the flame is represented by radiation. Consalvi and Nmira, (2019) carried out a thorough analysis of the literature involving the mechanisms of radiant heat flux generated by hydrogen flames.

The hydrogen flames are not characterized by the presence of soot and, therefore, the only species responsible for the radiation are the H_2O^* molecules in the excited state.

In order to estimate the radiative heat flux, the major semi-empirical models considered are the point source model and the surface emitter model (TNO, 2005).

The point source model does not consider the flame shape in the calculation of the incident radiation, but it assumes that the flame is described as a single point located on the centreline of the flame, as shown in Figure 3.23 (Hankinson and Lowesmith, 2012). The radiative heat flux (kW/m^2) at a distance S (m) to the target object is estimated through the Equation 3.18:

$$q = \frac{\chi_{rad}\ m_{fuel}\ \Delta H_c\ \tau}{4\pi S^2} \qquad (3.18)$$

in which: χ_{rad} is the radiated heat fraction, m_{fuel} and ΔH_c are the mass flow rate (kg/s) and the combustion heat of fuel (kJ/kg), respectively, and τ is the atmospheric transmissivity.

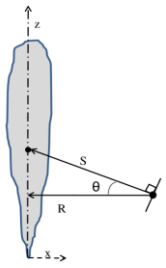

***Figure 3.24**: Single point source model (Hankinson and Lowesmith, 2012)*

As shown in the previous equation, a quantity that characterizes the radiative heat flux is the radiated heat fraction (χ_{rad}), defined as the fraction of the total radiative power emitted from the flame (S_{rad}) and the total heat released by the chemical reaction ($m_{fuel}\ \Delta H_c$):

$$\chi_{rad} = \frac{S_{rad}}{m_{fuel}\,\Delta H_c} \tag{3.19}$$

If the irradiated fraction is not known, the point source model in conjunction with experimental measurements of radiative heat flux (q^{meas}) can be used to evaluate it, as follows:

$$\chi_{rad} = \frac{q^{meas} S^2}{m_{fuel}\,\Delta H_c\,\tau} \tag{3.20}$$

A conservative approach considers the vertical flame, since the greater quantity of radiative heat flux is generated by these flames.

Experiments performed by Schefer et al. (2006, 2007) showed that the dependence of hydrogen jet flame radiant fractions on the flame residence time is logarithmic, as well as for hydrocarbons. However, the radiant fraction of hydrogen jet fires is about a factor of two lower than the hydrocarbon flames that also generate soot and CO_2.

Based on these observations, Molina et al. (2007) proposed a unified expression that considers the flame as a blackbody emitter. To take into account the different radiative characteristics of the different combustion products, the logarithmic dependence of the radiant fraction on the flame residence time (τ_G) has been modified and τ_G has been multiplied by $\alpha_P\ T_f^4$, where α_P is the Plank's mean absorption coefficient of the product species, i.e. H_2O for hydrogen flames. T_f can be approximated with the adiabatic flame temperature. Figure 3.25 shows this dependence.

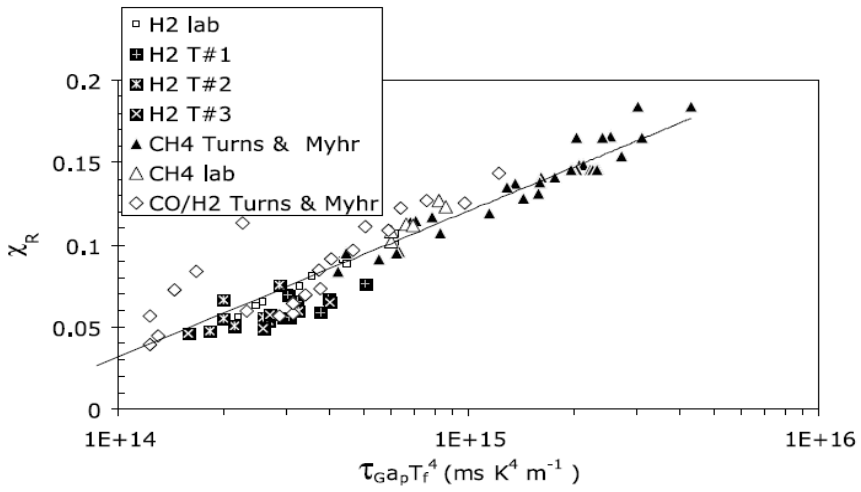

Figure 3.25*: Variation of radiative fraction (χ_{rad}) with the factor $\tau_G\,\alpha_P\,T_f^4$ for different hydrocarbon flames, proposed by Molina et al. (2007)*

The correlation suggested by Molina et al (2007) shows some limitations. The large-scale hydrogen flames have a greater thickness than the laboratory scale flames, considered optically thin, and so an underestimation of the radiation fraction values can be introduced. Furthermore, a momentum-controlled regime is assumed.

Hankison and Lowesmith (2012) have developed a weighted multi-point source model, in order to avoid erroneous results for the radiative heat flux in the near field of the flame. It is assumed that the radiation is emitted from a number N of point sources chosen along the flame axis, and the incident radiation is determined as the sum vector of the radiation from each source point. The procedure that describes how the point sources are weighted is the following:

$$w_j = jw_1 \qquad \text{for j= 1,…, n}$$

$$w_j = \left[n - \frac{n-1}{N-(n+1)}\,(j-(n+1))\right] w_1 \qquad \text{for j= n+1,…,N} \qquad (3.21)$$

$$\sum_{j=1}^{N} w_j = 1$$

where n is the number of point sources ($1 \leq n \leq N$).

According to this model, the radiative heat flux is evaluated through the vector sum given by:

$$q = \sum_{j=1}^{N} \vec{q_j} = \sum_{j=1}^{N} \frac{w_j \chi_{rad} m_{fuel} \Delta H_c \tau}{4\pi S_j^{\rightarrow 2}} \cos\varphi_j \qquad (3.22)$$

where w_j is the weighting of the jth source point by Equation 3.20 and φ_j is the angle between the normal of the target receiver and the line of sight to the jth source point, as shown in Figure 3.26:

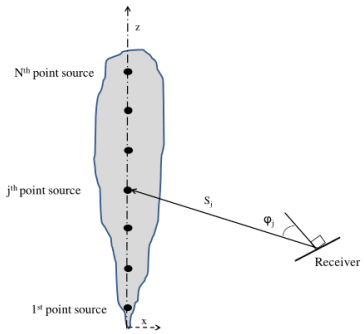

***Figure 3.26**: Weighted multi point source model by Hankinson and Lowesmith (2012)*

Differently from the point source model that does not consider the flame shape, in the surface emitter model this property has a central role. Taking into account a solid shape for the flame, usually conical or cylindrical, the radiative heat flux is evaluated through the following equation:

$$q = F \times E \times \tau \tag{3.23}$$

where F is the view factor, τ is the atmospheric transmissivity and E is the emissive power per flame surface (kW/m^2), evaluated as fraction of total heat released from the chemical reaction and the flame surface area (A_f), using the Equation (3.24):

$$E = \frac{\chi_{rad}\, m_{fuel}\, \Delta H_c}{A_f} \tag{3.24}$$

The cylindrical solid flame model has often been used to predict the radiant heat flux from jet flames, yet with considerable departure from the measurement results. The key reason is that a single constant emissive power over the whole flame surface, as well as e.g. three constant emissive powers, over three regions of the flame, respectively, cannot correlate the real variation of the emissive power over the flame surface. In particular, experimental investigations show that the emissive power first increases and finally decreases along the flame length of vertical small jet fires.

Zhou et al. (2014, 2016) proposed a thermal radiation prediction model and found that the line source model describing the heat flux radiated from a horizontal jet fire was more similar to experimental data than the point source model and multipoint source model. Specifically, it is able to provide a good prevision for jet fires both on small scale and large scale. On the contrary, the single point model can be used in the far field, but it is not valid in the near field, and the multipoint and the solid flame models are valid in the near field only (Huang et al., 2018).

The line source model (Zhou and Jiang, 2016) assumes that all the thermal energy is radiated from the centreline located inside the jet flame volume, with a length equal to the flame length (L). Flame lift-off is also taken into account. The line source model for horizontal jet fire is expressed as follows:

$$q = \int_S^{S+L} \frac{\tau\, E'}{4\pi R^2} \cos\theta \, dz \tag{3.25}$$

where E' is the emissive power per line length (EPPLL), S is the flame lift-off distance and R is the distance between any point at the centreline and the target. Different expressions for

the radiant heat flux have been presented according to the shape of the flame (i.e. combinations of cone, cylinder, ellipse). The line source model was found to well predict the radiant heat flux of both small and large jet flames, yet with the flame shape simulated by the back-to-back cone and the cone–cylinder combined shape, respectively (Figure 3.27 (a) and (b)).

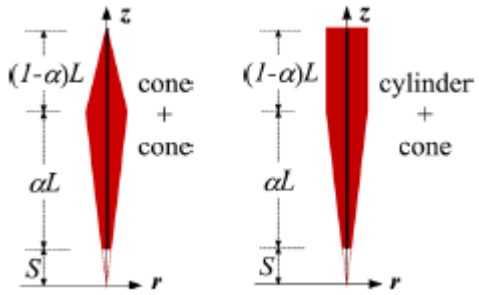

(a) *(b)*

Figure 3.27: *Line source model by Zhou and Jiang (2016)*

Among the semi-empirical models described above, the point source models have been especially validated against experimental tests of hydrogen jet fires (Schefer et al, 2006, 2007).

Radiant heat flux predictions derived from conventional single point source models have been observed to under-predict measured values by 40% or more, particularly in the near-field (Ekoto et al., 2012). On the contrary, weighted source flame radiation models have demonstrated substantial improvement in the heat flux predictions. These updated methods are still constrained by the fact that the flame is assumed to have a linear trajectory and flame, despite buoyancy effects that can result in significant flame deformation. Ekoto et al. (2014) have proposed a radiant heat flux predicted model for horizontally jet to predict flame centreline trajectories accounting for buoyancy effects.

3.8.3 Prediction of Radiative Heat flux

In this thesis, the radiative heat flux has been evaluated according to a procedure based on work carried out in HySAFER centre (HyResponse Report, 2016 (b)).

The radiative heat flux is obtained as follows:

$$q = F \times S \times \tau \qquad (3.26)$$

where: F is the view factor, S the surface emissive power and τ the atmospheric transmissivity.

In the previous Equation, the surface emissive power is defined as the product of the radiant fraction (χ_{rad}), the mass flow rate (m, kg/s) and the gas heat of combustion ($\Delta H_{c,\,H2O}$, MJ/kg):

$$S = \chi_{rad} \times m \times \Delta H_c \tag{3.27}$$

The mass flow rate is calculated through the Equation 3.3, illustrated in the section 3.1.

In order to evaluate the radiant fraction the expression used in the model was derived by Molina et al. (2007):

$$\chi_{rad} = 0.08916\, log_{10}\left(t_f \times \alpha_f \times T_{ad}^4\right) - 1.2172 \tag{3.28}$$

where: T_{ad} is the adiabatic flame temperature (K), α_f is the Plank's mean absorption coefficient for the product species (m^{-1}) and t_f is the flame residence time (ms), evaluated through the correlation of Turns and Myhr (1991) (Equation 3.30):

$$t_f = \frac{\pi}{12}\frac{\rho_f W_f^2 L_f Y_s}{m} \tag{3.29}$$

where: W_f and L_f are the width and the length of the visible flame, respectively; Y_s is the hydrogen stoichiometric mass fraction, m is the mass flow rate (kg/s).

The following equation is used for the flame density evaluation:

$$\rho_f = \frac{P_{amb} \times MW_{st}}{R_u \times T_{ad}} \tag{3.30}$$

In Table 3.13 the numerical values used for the heat flux prediction are reported:

Adiabatic Temperature (T_{ad})	2390 K
Plank's mean absorption coefficient for the product species (α_f)	0.23 m^{-1}
H_2 stoichiometric mass fraction (Y_s)	0.0281
Ambient pressure (P_{amb})	101325 Pa
Stoichiometric molecular weight (MW_{st})	24.52 g/mol
Universal gas constant (R_u)	8314.47 g/(kmol*K)

***Table 3.13**: Values used in the procedure for the heat flux predictions*

The estimate of view factor (F) and atmospheric transmissivity (τ) depends on the model chosen to represent the flame.

As regards the view factor, according to the analysis of the literature reported above, different models are available in order to characterize the flame. On the basis of preliminary numerical evaluations against experimental data carried out in order to establish the most suitable model to use, the point source model has been assumed in the evaluation of the radiative heat flux, allowing a good compromise between accuracy and ease of calculation.

Regarding the atmospheric transmissivity (τ), an accurate estimation is important, since the atmosphere absorbs and scatters the thermal radiation. The correlation proposed by Pieterson and Huerta (1985) (reported by AIChE, 2000) (Equation 3.31) has been used:

$$\tau = 2.02(P_w \times x)^{-0.09} \quad (3.31)$$

where: P_w is the water partial pressure (Pa) and x is the distance from the flame surface to the target (m).

Mudan and Croce (1988) (reported by AIChE, 2000) suggested for the water partial pressure the expression below (Equation 3.32):

$$P_w = 101325\ (RH) \exp\left(14.4114 - \frac{5328}{T_a}\right) \quad (3.32)$$

where: P_w is the water partial pressure (Pa), RH is the relative humidity (percent) and T_a is the ambient temperature (K).

The procedure proposed was validated against experimental data from the literature.

Mogi et al. (2005, 2009) performed a series of experiments to investigate the hazards of high-pressure hydrogen jet diffusion flames. Hydrogen releases, oriented horizontally, through circular nozzle varying between 0.1 and 4 mm were analysed. The pressure in the four storage tanks (0.046 m^3 each) was 45 MPa and hydrogen was released with a pressure ranging from 0.01 to 40 MPa. The trigger was realised using a torch burner fuelled with liquefied petroleum gas. In order to visualize the hydrogen jet flame an aqueous Na_2CO_3 solution was atomized above the fuel injection nozzle. The thermal radiation was analysed using radiometers located at 1.5, 2.5 and 3.5 m from the flame axis.

The experimental setup was illustrated in Figure 3.28:

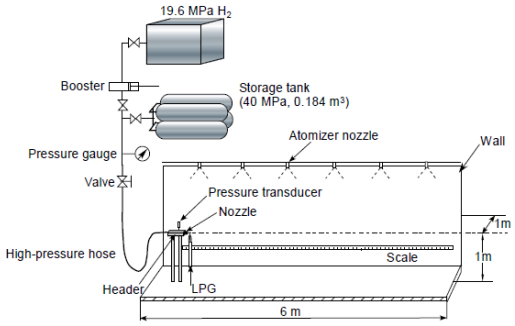

***Figure 3.28**: Experimental apparatus (Mogi et al., 2009)*

Results of validation are reported in Figure 3.29, and are relevant to the available experimental data in terms of radiative heat flux measured at the radiometers, for the scenarios characterized by release pressures of approximately 35, 30, 20, 10, 7 and MPa for d_h= 2 mm, and of approximately 30, 35 and 20 MPa for d_h= 0.4 mm, respectively. As shown in the graph, predicted data present a quite good agreement with experimental data. Major deviations are calculated only at the nearest radiometer (1.5 m from flame axis).

The value of the global relative error (e=27%) was deemed to assure a satisfactory conservative approximation of the estimated radiative heat fluxes by using this procedure. Moreover, as the distance from the flame axis increases, the relative error progressively becomes smaller (overall 30% at 1.5 m, 28% at 2.5 m, 23% at 1.5 m, respectively).

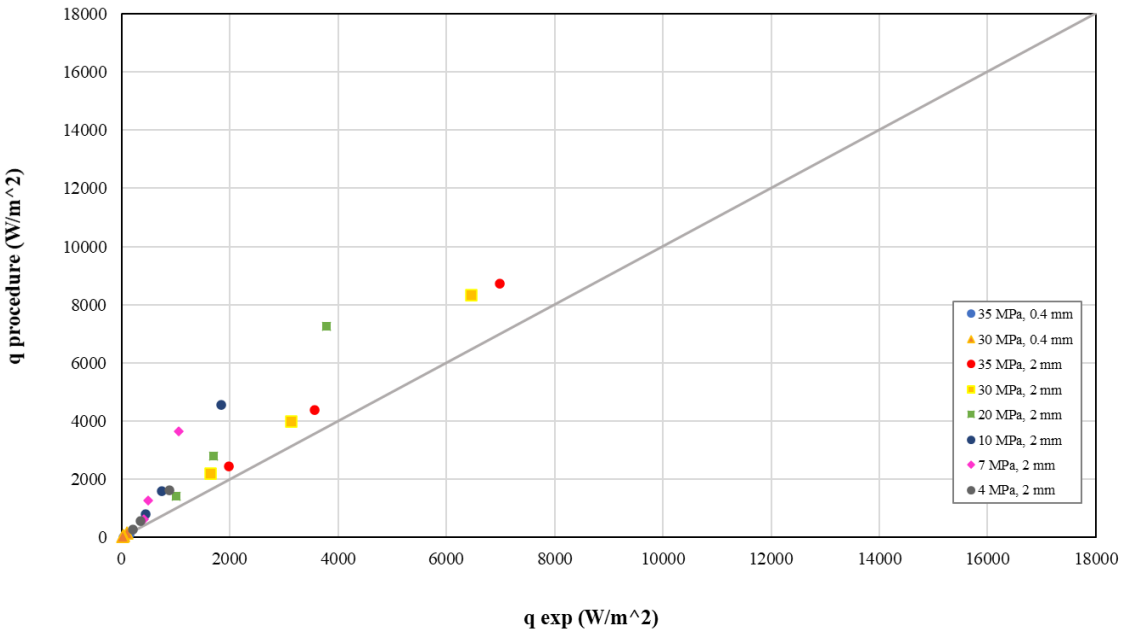

***Figure 3.29**: Comparison of heat flux predicted and experimental data*

3.8.3 SLAB + point source model for radiative heat flux

The methodology previously proposed to perform a quantitative risk assessment in the case of gaseous hydrogen explosions has been then employed in the event of hydrogen jet fires.

The values of hydrogen concentration calculated by using SLAB, in the operative conditions illustrated above, have been employed in order to define the flame length and the flame width (W_f=0.17 L_f).

According to the literature, in the case of jet fires shorter distances with respect to explosions are required for risk analysis. Values between 10 e 700 m were assumed, after a preliminary assessment that confirmed the absence of damage for distances greater than 700 m.

The calculated results have been classified in 14 classes of radiation heat flux. Each class has been chosen taking into account the threshold values of thermal dose for different damage. The mean value of each class was adopted as representative of the class.

The classes of radiative heat flux chosen in order to estimate the damage are reported in Table 3.14:

Class	**Range (kW/m^2)**		**Mean (kW/m^2)**
1	0	799	400
2	800	1699	1250
3	1700	2599	2150
4	2600	4999	3800
5	5000	9999	7500
6	10000	19999	15000
7	20000	29999	25000
8	30000	39999	35000
9	40000	49999	45000
10	50000	99999	75000
11	100000	149999	125000
12	150000	499999	325000
13	500000	999999	75000
14	1000000	1635000	1317500

***Table 3.14**: Classes of radiative heat flux (kW/m^2)*

3.9 Damage to people involved in a jet fire

People involved in a jet fire can suffer damage due to exposition to flames because of high air temperature or high radiative heat fluxes generated by fires.

Similarly to the case of explosions, harm criteria in terms of injuries or fatalities may be considered.

Both physiological and pathological effects due to heat radiation can be manifested.

Physiological effects result from the hot and humid conditions to which people are exposed and are identified by an increase of the heartbeat, sweating and rise of body temperature.

Pathological effects are connected to the burns caused by the heat generated by the fires.

Depending on the duration of the exposition and on the intensity of the heat fluxes, first, second or third burns may occur.

In order to assess the consequences of a jet fire on people, Probit Functions are used.

In literature several Probit Functions are reported, in order to evaluate the damage to people involved in fires.

Eisenberg et al. (1975) (reported by Hymes et al., 1996)**,** in a report on the hazards from marine spill drafted for the US Coastguard, proposed the following Probit equation for thermal radiation leading to fatalities:

$$Y = -14.9 + 2.56 \log\ (q^n t) \qquad (3.33)$$

where: Y is the Probit Function, t is the exposure time (s), q is the effective radiation intensity (kW/m^2), and the exponent n is equal to 4/3.

The study carried out by Eisenberg was referred to flash fires, in particular to the consequences of the thermal component of the nuclear flash. The value of exponent n suggested was valid for the spectral range of radiation, representative of heat generated by chemical and nuclear fireballs.

Crowl and Louvar (2011) reported the Probit Correlation suggested by Eisenberg, related to a fire, adapting them also to pool fires, also:

$$Y = -14.9 + 2.56\ \ln\left|\left(q^{4/3}\ \times t\right)/10^4\right| \qquad \text{for } \textit{burns deaths from flash fires} \qquad (3.34)$$

$$Y = -14.9 + 2.56\ \ln\left|\left(q_P^{4/3}\ \times\ t_P\right)/10^4\right| \qquad \text{for } \textit{burns deaths from pool burning} \qquad (3.35)$$

where: q and q_P are the effective radiation intensity (W/m^2) from a flash fires and from a pool burning, respectively; t and t_P are the effective time duration (s) of flash fires and pool burning.

Based on data for nuclear explosions, in the "Vulnerability Model" Eisenberg suggested a Probit Function determined from lethality data for different magnitudes of nuclear weapons:

$$Y = -38.48 + 2.56 \ln \left(q^{4/3} \times t\right) \quad \text{for } \textit{lethality} \quad (3.36)$$

where t is in s and q in W/m^2.

However, nuclear explosions are characterized by wave-lengths of heat radiation into the range of the visible, while the wave-length of fires of hydrocarbons is mainly into the infrared zone.

Since the radiation that affects humans increases with increasing wave-length, for fires of hydrocarbons a radiation dose lower than the radiation dose from nuclear explosions is required (TNO, 1989).

As a consequence of these considerations, on the basis of Eisenberg's data, Stoll et al. (1969) proposed the following Probit functions for fires of hydrocarbons:

$$Y = -36.38 + 2.56 \ln \left(q^{4/3} \times t\right) \quad \text{for } \textit{lethality} \quad (3.37)$$

$$Y = -39.83 + 3.0186 \ln \left(q^{4/3} \times t\right) \quad \text{for } \textit{first-degree burn} \quad (3.38)$$

$$Y = -43.14 + 3.0186 \ln \left(q^{4/3} \times t\right) \quad \text{for } \textit{second-degree burn} \quad (3.39)$$

La Chance et al. (2011), from the analysis of the literature, have highlighted Probit functions that take into considerations the clothing:

$$Y = -37.23 + 2.56 \ln \left(q^{4/3} \times t\right) \quad \text{for } \textit{fatality} \quad (3.40)$$

$$Y = -29.02 + 1.99 \ln \left(F \times t \times q^{4/3}\right) \quad \text{for } \textit{fatality} \quad (3.41)$$

where: t is in s; q is in W/m^2.

In the Equation 3.41, the clothing is taken into account for 14%; instead, in the Equation 3.42, the clothing is considered through the terms F. The terms F is equal to 0.5 for normally clothed population; equal to 1 when clothing ignition occurs.

In Table 3.15 the Probit Functions reported in literature and used for various types of fires are summarized.

Probit Function	Type of fires	Damage	Ref.
$Y= -14.9 + 2.56 \ln [(q^{4/3} x t)/10^4]$	pool and flash fires	Fatality	Eisenberg (1975)
$Y= -14.9 + 2.56 \ln [(q^{4/3} x t)/10^4]$	flash fires	Fatality	Crowl (2011)
$Y= -14.9 + 2.56 \ln [(q_P^{4/3} x t_P)/10^4]$	pool fires	Fatality	Crowl (2011)
$Y= -36.38 + 2.56 \ln (q^{4/3} x t)$	fires	Fatality	Tsao & Perry (1979)
$Y= -37.23 + 2.56 \ln (q^{4/3} x t)$	fires	Fatality (for clothing)	Tsao & Perry (1979)
$Y= -29.02 + 1.99 \ln (q^{4/3} x t x F)$	-	Fatality (for clothing)	Less (1994)
$Y= -36.38 + 2.56 \ln (q^{4/3} x t)$	fires	Fatality	TNO (1989)
$Y= -39.83 + 3.0186 \ln (q^{4/3} x t)$	fires	First degree burn	TNO (1989)
$Y= -43.14 + 3.0186 \ln (q^{4/3} x t)$	fires	Second degree burn	TNO (1989)

Table 3.15: *Probit Functions for fires.*

In this thesis, Probit Functions proposed by TNO (Equation 3.37, 3.38 and 3.39) were taken into consideration in order to evaluate the damage caused by a jet fire following an accidental failure of hydrogen pipeline. These Probit equations have been selected because they are valid for general fires, firstly; furthermore, different kinds of damage are contemplated, both in terms of injuries and fatalities.

Several sources were considered in order to establish harm criteria for people involved in jet fires. Table 3.16 reports the ranges of thermal doses required to give pain and burns, as suggested in literature (DNV Technica, 2001).

Effect	Thermal dose ($s^* [kW/m^2]^{4/3}$)
Pain	108- 127
	85-129
Significant injury level/ First degree burns	600- 800
	250- 350
Second degree burns/ 1% lethality level for average clothing	900-1300
	500-3000
Third degree burns/ 50% lethality level for average clothing	>2000-3000

Table 3.16*: Threshold harm criteria of Thermal Doses required to give Pain, Burns and Fatal Outcomes*

3.10 Damage to structures involved in a jet fire

The radiative heat flux resulting from a jet fire can also cause damage to structures located in the proximity to the gas release. The consequent damage essentially depends on how the materials used in the construction of the structure respond to the direct flame impingment and to the radiative heat flux emitted by the flame.

Generally, the most considered construction materials are wood, plastic materials, glass and steel.

Wood and plastic materials are combustibles and so, when they are ignited (270-390°C), can cause secondary fires. On the other hand, the high temperatures achieved by the flame can provoke the rupture of glasses, while steel can be damaged at temperatures as high as 500-600°C, losing strength and stiffness.

On the contrary**,** masonry, reinforced concrete and coated steel might suffer damage due to the radiative heat flux in severe conditions only, if the structure or the equipment is into the flame, for example (TNO, 1989).

Typical heat flux values that can cause damage to structures and equipment are reported by La Chance et al. (2011), as shown in Table 3.17. They refer to an exposure time of 30 min. These values are currently used as criteria in the quantitative risk analysis also in the case of hydrogen fire.

Damage	Thermal radiation intensity (kW/m^2)
Glass breakage	4
Piloted ignition of wood Melting of plastic	12.5- 15
Cable insulation degrades	18-20
Unpiloted ignition of wool Steel deformation	25-32
Process equipment and structural damage	35-37.5
Steel structure collapse	100

Table 3.17: *Damage to structures and equipment for 30 min exposure to thermal radiation*

Conversely, Probit functions that correlate the probability to have a given damage on structures and equipment as function thermal radiation intensity are not available in the literature.

Since damage due to the thermal radiation to be significant require long exposure times (> 30 min), the effect of radiative heat flux on structures can be avoided by interrupting the gas release within 30 min.

CHAPTER 4

Results and discussion

4.1 Introduction

The analyses of the hydrogen properties and of the hazards following an uncontrollable hydrogen release from high-pressure pipelines have highlighted that the most dangerous consequences of an accidental event might be an explosion or a jet fire.

The results of simulations performed in order to evaluate the effects on people and property located in proximity of a failed hydrogen pipeline are presented.

Simulations were carried out varying pipeline operating parameters (i.e. diameter, pressure) and source release properties (i.e. hole diameter, length of pipeline from the supply station to the release point).

In Table 4.1 the numerical values of the pipeline operating parameters and source release properties employed in the simulations are summarized:

Parameter	Assumption
Pipeline diameter (d), m	0.1016- 0.508
Operating pressure (P_0), kPa	649- 12800
Hole diameter (d_{hole}), m	0.02 - d
Pipeline length from the gas supply station to the release point (L), m	50 – 10000
Distances from explosion centre (R), m	10 -2000
Distance from jet fire centre (r), m	10- 700
Wind velocity, m/s	2 and 5
Atmospheric stability class	A, C, D, F

***Table 4.1**: Pipeline operating parameters and source release properties employed in the simulations*

4.2 Blast hazard

The results of simulations are analysed in terms of peak overpressure and impulse as a function of pipeline operating properties and source release.

The Figures 4.1 (a) and (b) show the trend of the peak overpressure and of the impulse versus the hole diameter (d_{hole}) in conditions of atmospheric stability class D5 and explosivity class 9, and assuming a pipeline distance to the centre of explosions R=500 m, a pipe diameter d=0.508 m and a length of pipeline from the point of compression L=1000 m, at different values of pipeline operating pressure. As the pipeline diameter is increased, the blast parameters increased and the maximum levels of reached overpressure and impulse fell in a range of 0.2–0.3 m.

The peak overpressure and the impulse versus the length of pipeline from compression station, at different pipeline diameter and at an operating pressure P_0=3800 kPa, are reported in Figures 4.2 (a) and (b), considering the same ambient and explosive conditions and the same values of parameters.

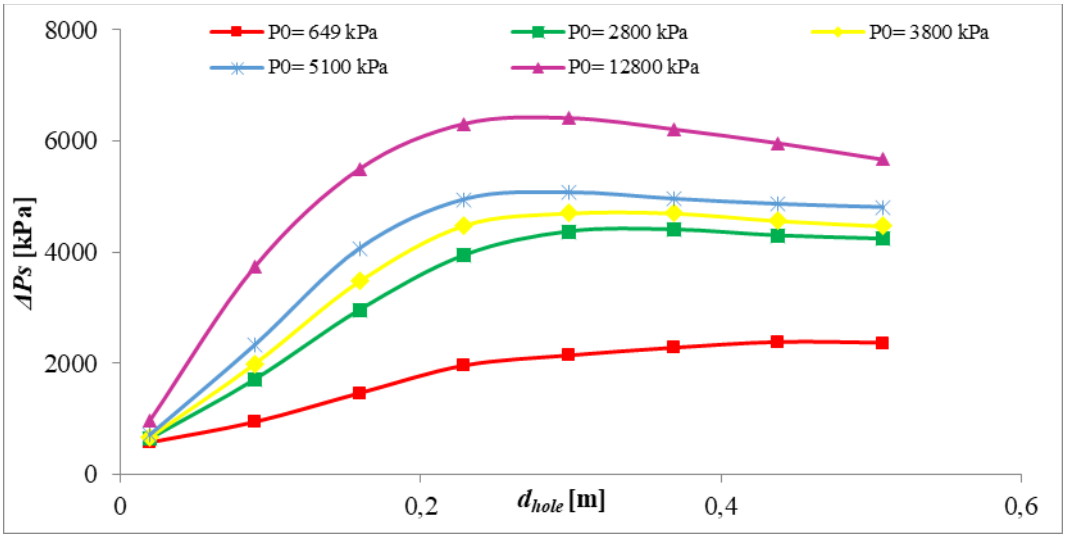

(a)

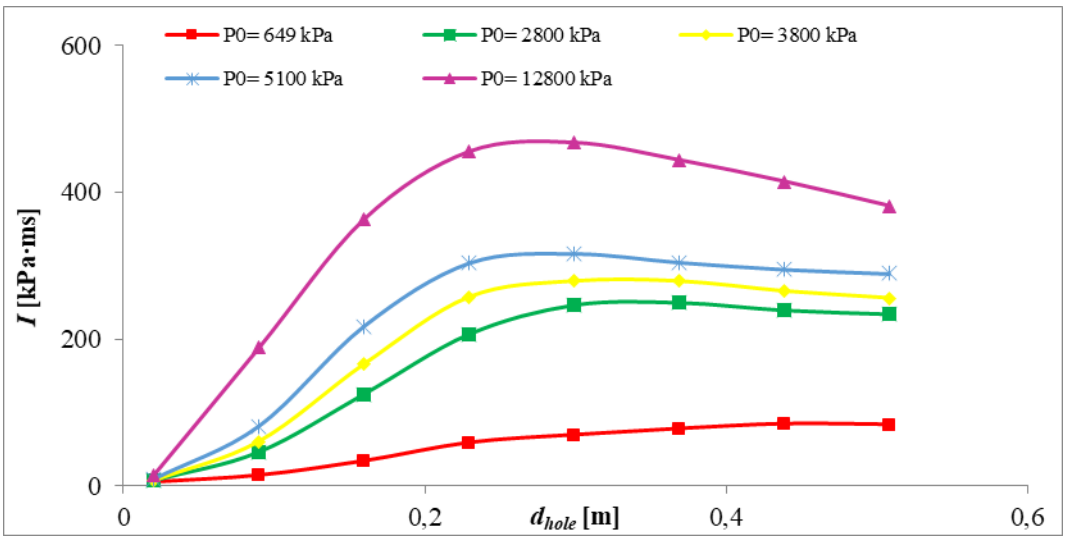

(b)

***Figure 4.1**: Peak of overpressure (a) and impulse (b) versus hole diameter at different value of operating pressure (d=0.508 m, L=1000 m, R=500 m, atmospheric stability class D, v= 5 m/s, explosivity class 9)*

In contrast with the previous figure, as the distance L increases, the inside pressure of the pipeline decreases and so the blast parameters decrease, too. Once the value of 1000 m is reached, the blast parameters take on an almost constant trend, due to the gas release rate remaining near constant.

Similar results were obtained for atmospheric stability class F2 and explosivity class 6.

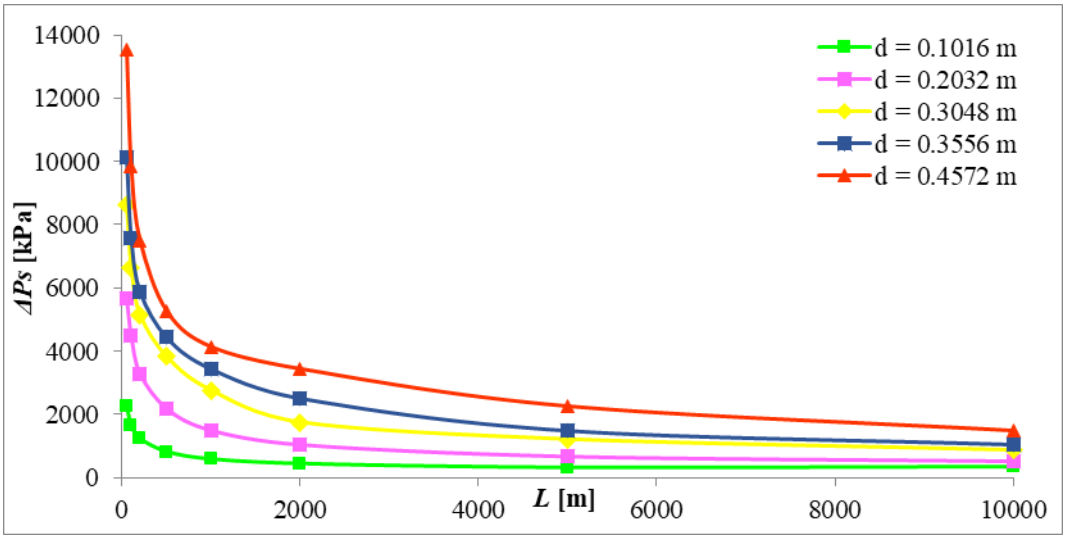

(a)

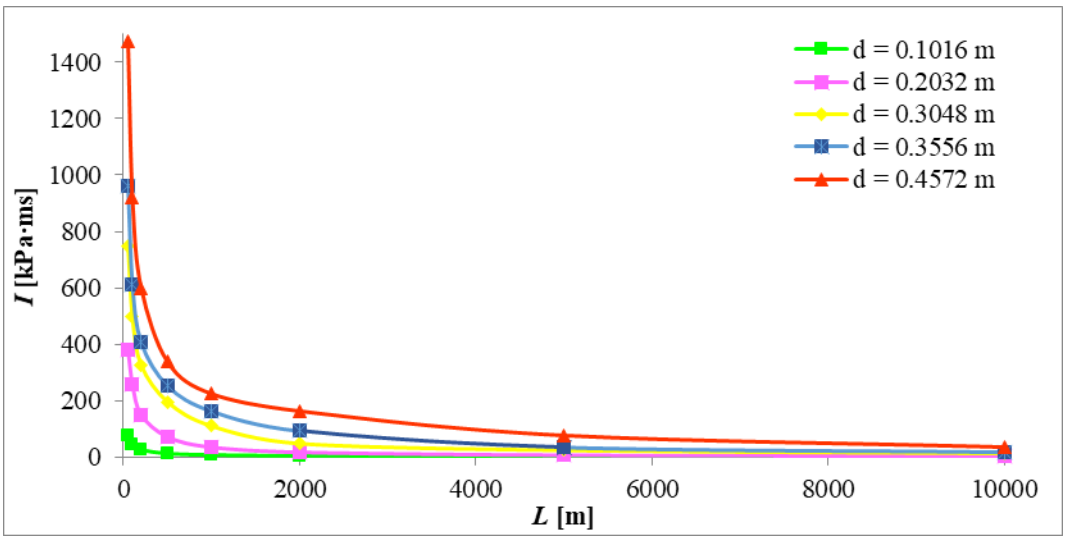

(b)

***Figure 4.2**: Peak of overpressure (a) and impulse (b) versus length from the point of compression at different value of pipeline diameter (P= 3800kPa, R=500 m, d=d_{hole} (full rupture) atmospheric stability class D, v= 5 m/s, explosivity class 9)*

Subsequently, the results of simulations were analysed in probabilistic terms and the probability that a blast would take place was evaluated.

As shown in Figures 4.3 and 4.4 ((a) and (b)), the peak of overpressure and impulse achieve the highest values (507 kPa and 60,000 kPa x ms, respectively) in the case of explosivity class 9. In addition, the highest blast probability is observed at 1 kPa and 125 kPa x ms, corresponding to 33% for blast strength 9 and above to 36% for blast strength 6.

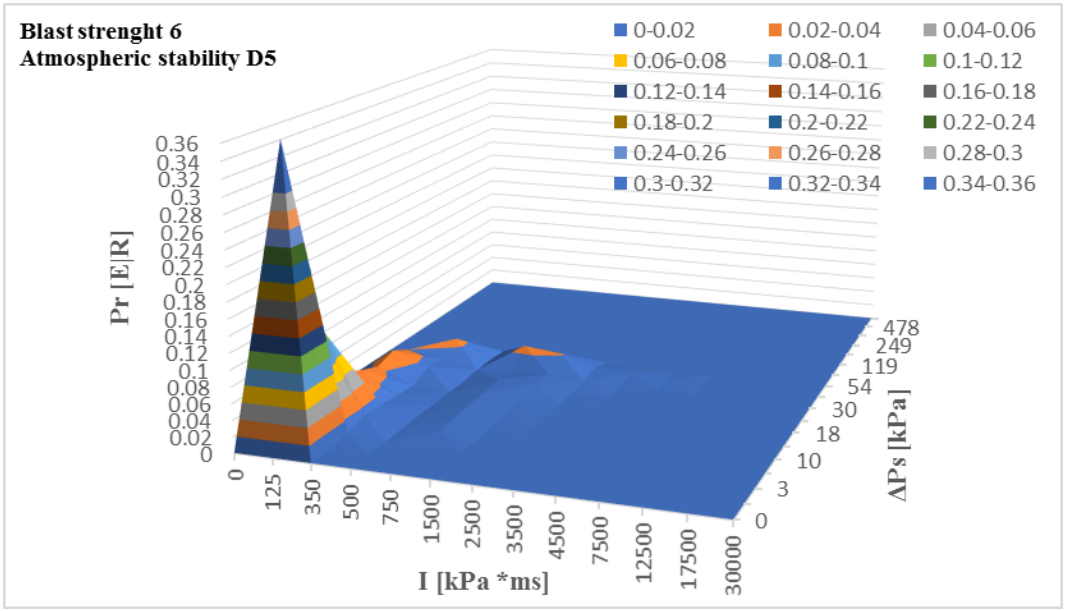

(a)

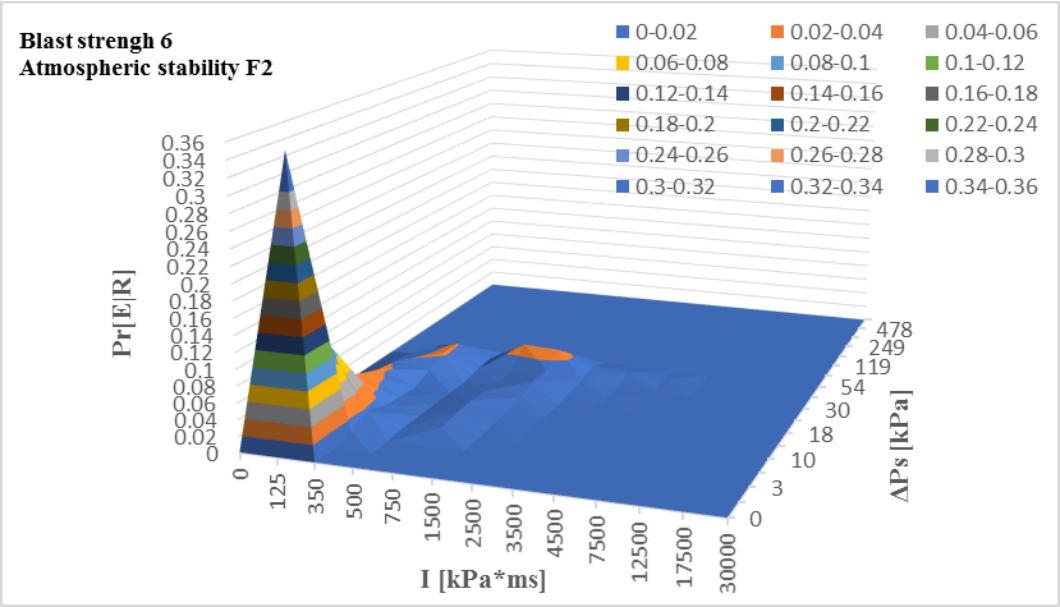

(b)

***Figure 4.3**: Blast probability for the blast strength 6 and atmospheric stability classes D5 (a) and F2 (b)*

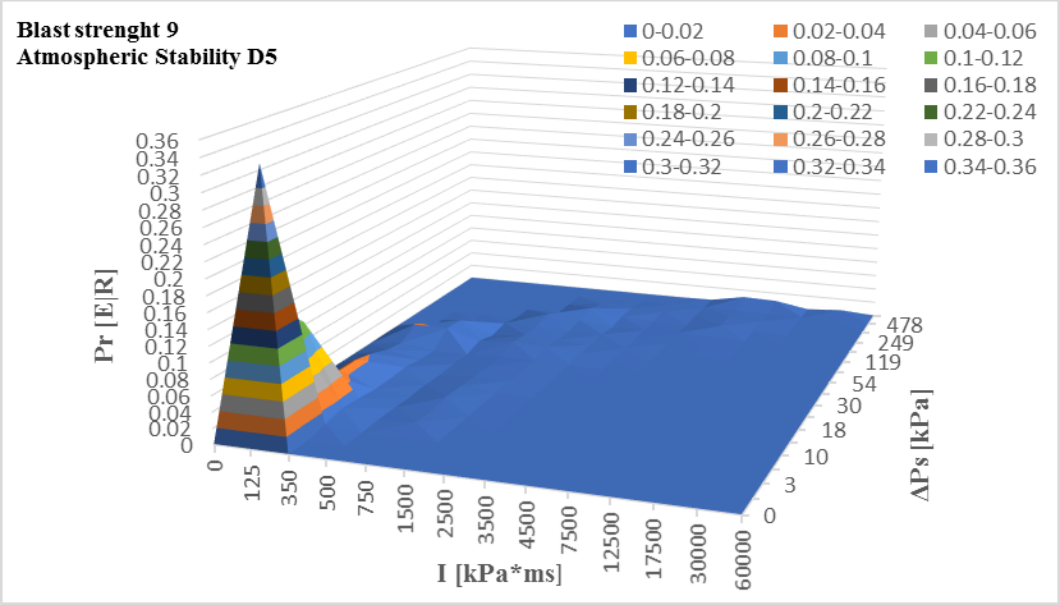

(a)

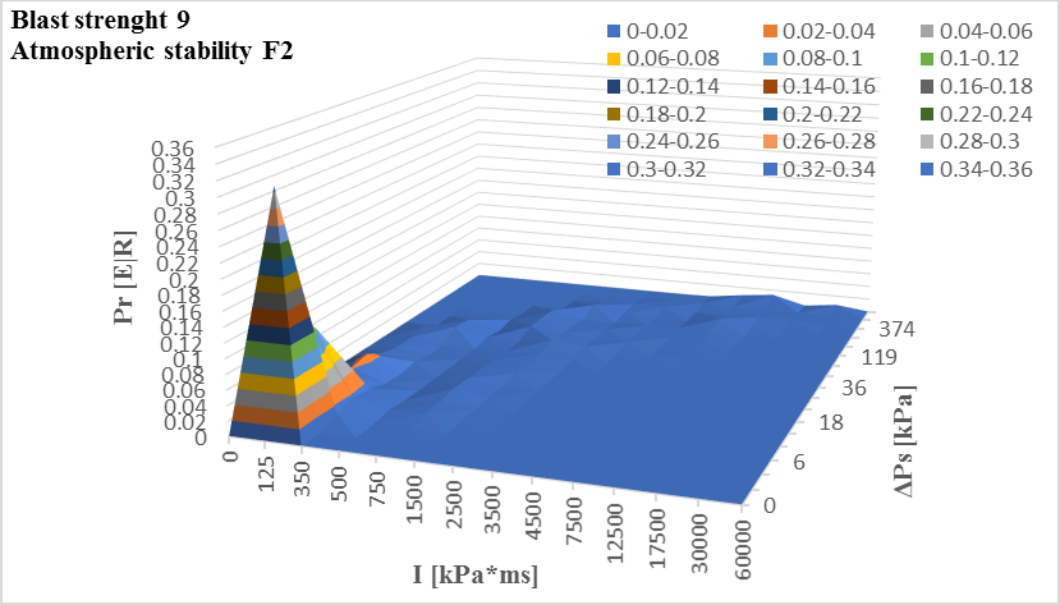

(b)

***Figure 4.4**: Blast probability for the blast strength 9 and atmospheric stability classes D5 (a) and F2 (b)*

4.3 Damage to structural components

The analysis of the results shows that the blast impact of the explosion on the structural building components is completely different in the case of the two types of columns considered, i.e. reinforced concrete columns and tuff stone masonry walls.

The Figure 4.5 (a) and (b) reports the P-I diagrams related to the gravity-load designed RC columns for the two explosive classes taken into account, 6 and 9, respectively, and for the two atmospheric conditions examined, D5 and F2. As shown, both situations resulted safe.

The numerical simulations of hydrogen gas explosions, performed in the above cited conditions, generated several P-I combinations and all these combinations are located in the zone below the P-I capacity curve of the RC columns. In the case of strength 6, the values of peak overpressure and impulse achieved are rather lower than the pressure and impulse asymptotes, P_0= 769 kPa and I_0= 6398 kPa x ms (Parisi, 2015).

In the other case evaluated, the maximum values of peak overpressure and impulse in any conditions did not exceed the asymptote ones, even if they were greater and reached 507 kPa and 300,000 kPa x ms, respectively.

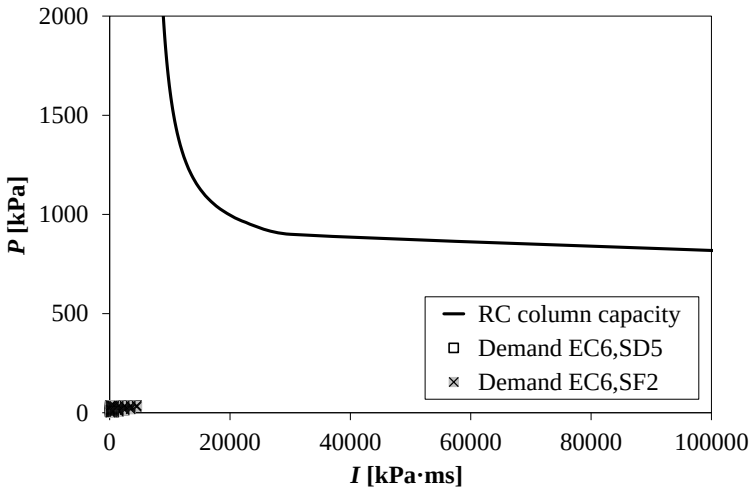

(a)

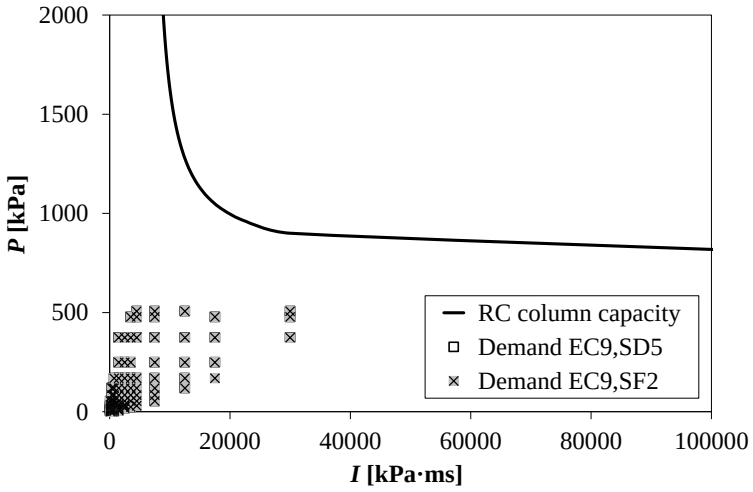

(b)

Figure 4.5*: Comparison between blast demand and capacity of RC columns for explosivity class 6 (a) and 9 (b), for atmospheric conditions D5 and F2.*

On the contrary, a considerable vulnerability to blast loading is shown in the P-I diagrams related to the TSM walls, as reported in the Figure 4.6 (a) and (b). Both the conditions analysed resulted unsafe. Many P-I combinations resulting from the numerical simulations were found above the P-I capacity curve of TSM walls, whose pressure and impulse asymptote are 3.5 kPa and 455 kPa x ms (Parisi et al., 2016), respectively. This trend is observed especially in the case of explosivity class 9.

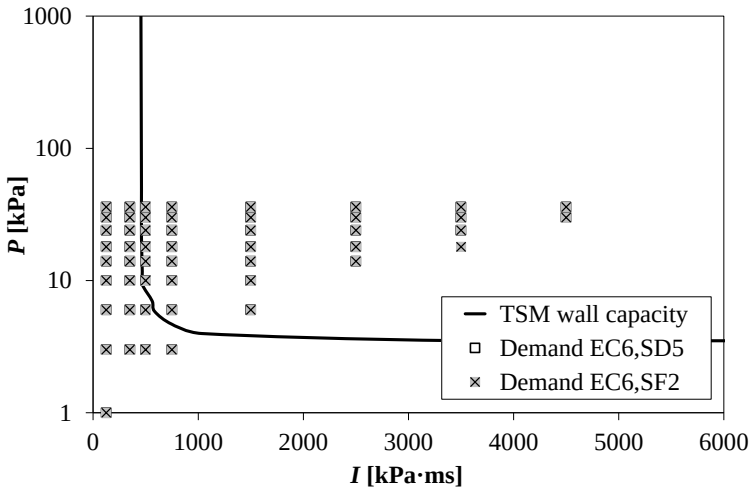

(a)

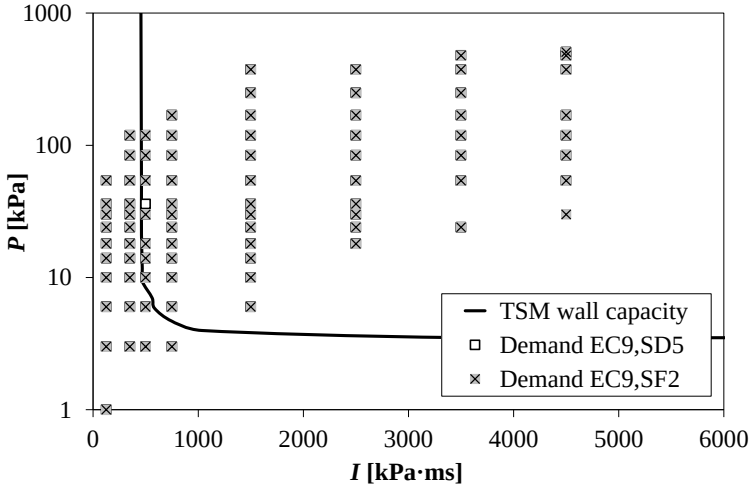

(b)

***Figure 4.6**: Comparison between blast demand and capacity of TSM walls for explosivity class 6 (a) and 9 (b), for atmospheric conditions D5 and F2.*

Finally, the maximum distance from the blast centre (pipeline), at which definite values of overpressure and impulse are reached, was calculated. This distance is called blast demand radius of blast waves and the results obtained in the numerical simulations are reported for explosivity class 6 in Tables 4.2 and 4.3 for atmospheric conditions D5 and F2, respectively, and for explosivity class 9 in Tables 4.4 and 4.5 for atmospheric conditions D5 and F2, respectively.

Both the blast strength considered (class 6 and 9) achieved a value of 2000 m in both ambient conditions (D5 and F2). Instead, taking into account the distances at which damage to TSM load-bearing walls was observed (underlined values in the Table 4.2, 4.3, 4.4, 4.5), a value of 1000 m is obtained in the case of explosivity classes 6 and atmospheric conditions D5 and

F2. The same value is also found in the case of explosivity classes 9 and atmospheric conditions F2, instead in the atmospheric condition D5 the blast demand radius of blast waves is 2000 m for explosivity class 9.

		I [kPa•ms]												
		125	350	500	750	1500	2500	3500	4500	7500	12500	17500	30000	60000
ΔP [kPa]	1	2000	-	-	-	-	-	-	-	-	-	-	-	-
	3	2000	2000	2000	2000	-	-	-	-	-	-	-	-	-
	6	500	500	1000	1000	1000	-	-	-	-	-	-	-	-
	10	100	200	200	500	500	-	-	-	-	-	-	-	-
	14	50	100	100	200	200	500	-	-	-	-	-	-	-
	18	20	50	50	100	200	200	-	-	-	-	-	-	-
	24	20	20		50	100	200	200	-	-	-	-	-	-
	30	10	20	20	50	100	100	200	200	-	-	-	-	-
	36	-	10	10	20	50	50	100	100	-	-	-	-	-
	54	-	-	-	-	-	-	-	-	-	-	-	-	-
	84	-	-	-	-	-	-	-	-	-	-	-	-	-
	119	-	-	-	-	-	-	-	-	-	-	-	-	-
	169	-	-	-	-	-	-	-	-	-	-	-	-	-
	249	-	-	-	-	-	-	-	-	-	-	-	-	-
	374	-	-	-	-	-	-	-	-	-	-	-	-	-
	478	-	-	-	-	-	-	-	-	-	-	-	-	-
	507	-	-	-	-	-	-	-	-	-	-	-	-	-

Table 4.2: *Blast demand radius (m) at different levels of peak overpressure and impulse for explosivity class 6 and atmospheric stability class D5.*

		I [kPa•ms]												
		125	350	500	750	1500	2500	3500	4500	7500	12500	17500	30000	60000
ΔP [kPa]	1	2000	-	-	-	-	-	-	-	-	-	-	-	-
	3	2000	2000	2000	2000	-	-	-	-	-	-	-	-	-
	6	500	500	1000	1000	1000	-	-	-	-	-	-	-	-
	10	100	200	200	500	500	-	-	-	-	-	-	-	-
	14	50	100	100	200	500	500	-	-	-	-	-	-	-
	18	20	50	50	100	200	200	500	-	-	-	-	-	-
	24	20	20		50	100	200	200	-	-	-	-	-	-
	30	10	20	20	50	100	100	200	200	-	-	-	-	-
	36	-	10	10	20	50	50	100	100	-	-	-	-	-
	54	-	-	-	-	-	-	-	-	-	-	-	-	-
	84	-	-	-	-	-	-	-	-	-	-	-	-	-
	119	-	-	-	-	-	-	-	-	-	-	-	-	-
	169	-	-	-	-	-	-	-	-	-	-	-	-	-
	249	-	-	-	-	-	-	-	-	-	-	-	-	-
	374	-	-	-	-	-	-	-	-	-	-	-	-	-
	478	-	-	-	-	-	-	-	-	-	-	-	-	-
	507	-	-	-	-	-	-	-	-	-	-	-	-	-

Table 4.3: *Blast demand radius (m) at different levels of peak overpressure and impulse for explosivity class 6 and atmospheric stability class F2.*

		I [kPa•ms]												
		125	350	500	750	1500	2500	3500	4500	7500	12500	17500	30000	60000
ΔP [kPa]	**1**	2000	-	-	-	-	-	-	-	-	-	-	-	-
	3	2000	2000	2000	2000	-	-	-	-	-	-	-	-	-
	6	500	1000	1000	2000	1000	-	-	-	-	-	-	-	-
	10	100	200	200	500	1000	-	-	-	-	-	-	-	-
	14	100	100	200	200	500	-	-	-	-	-	-	-	-
	18	50	100	100	200	500	500	-	-	-	-	-	-	-
	24	20	50		100	200	500	500	-	-	-	-	-	-
	30	20	50	50	100	200	200	-	-	-	-	-	-	-
	36	20	20		50	100	200	-	-	-	-	-	-	-
	54	10	20	20	50	100	200	200	200	200		-	-	-
	84	-	10	20	20	50	100	100	100	200		-	-	-
	119	-	10	10	20	20	50	50	100	100	200	-	-	-
	169	-	-	-	10	20	20	50	50	100	200	-	-	-
	249	-	-	-	-	10	20	20		50	100	100	-	-
	374	-	-	-	-	10	10	20	20	50	50	100	100	-
	478	-	-	-	-	-	-	10	10	20		50	100	100
	507	-	-	-	-	-	-	-	10	20	20	-	50	100

Table 4.4: *Blast demand radius (m) at different levels of peak overpressure and impulse: explosivity class 9, atmospheric stability class D5.*

		I [kPa•ms]												
		125	350	500	750	1500	2500	3500	4500	7500	12500	17500	30000	60000
ΔP [kPa]	1	2000	-	-	-	-	-	-	-	-	-	-	-	-
	3	2000	2000	2000	2000	-	-	-	-	-	-	-	-	-
	6	500	1000	1000	1000	1000	-	-	-	-	-	-	-	-
	10	100	200	200	500	1000	-	-	-	-	-	-	-	-
	14	100	100	200	200	500	-	-	-	-	-	-	-	-
	18	50	100	100	200	500	500	-	-	-	-	-	-	-
	24	20	50		100	200	500	500	-	-	-	-	-	-
	30	20	50	50	100	200	200	-	500	-	-	-	-	-
	36	20	20		50	100	200	-	-	-	-	-	-	-
	54	10	20	20	50	100	200	200	200	500	-	-	-	-
	84	-	10	20	20	50	100	100	100	200	-	-	-	-
	119	-	10	10	20	20	50	50	100	100	200	-	-	-
	169	-	-	-	10	20	20	50	50	100	200	200	-	-
	249	-	-	-	-	10	20	20		50	100	100	-	-
	374	-	-	-	-	10	10	20	20	50	50	100	100	-
	478	-	-	-	-	-	-	10	10	20	-	50	100	100
	507	-	-	-	-	-	-	-	10	20	20	-	50	100

Table 4.5: *Blast demand radius (m) at different levels of peak overpressure and impulse: explosivity class 9, atmospheric stability class F2.*

4.4 Case study

The methodology proposed has been employed in order to analyse a case study.

The building taken into consideration stands on two levels and its structural components are in TSM. The structure is located in the south of Italy, in a small town near Benevento, at about 580 m above sea level, in Zone 3. The Italian Building Code (DM, 2018) states several zones according to the mean wind speed ($v_{b,o}$) at the sea level, taking into account a return period of 50 y, a time of 10 min, a height of 10 m above the homogeneous and smooth ground. In Zone 3 the mean wind speed is 27 m/s. However, a value of 28.62 m/s was adopted as the mean intensity of wind (v_b), multiplying $v_{b,o}$ by c_a=1.06, a factor that considers the dependence from altitude in the case of interest.

The TSM building is situated at 25 m from the pipeline (Figure 4.7).

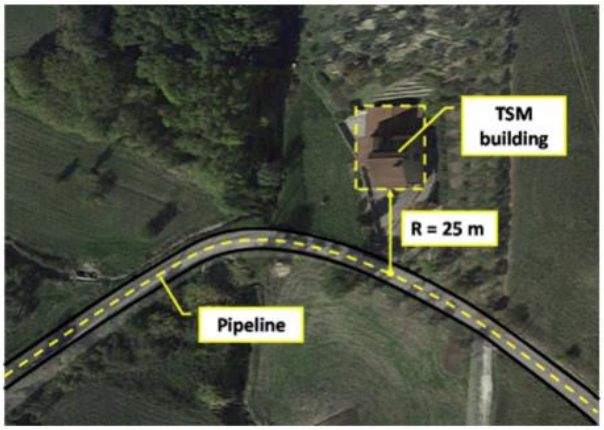

***Figure 4.7**: Case-study TSM building with respect to the pipeline*

In order to assess the blast impact of an accidental explosion, the structural components Piers 1 and 2 over the building façade in closest proximity of the pipeline were identified. As shown in Figure 4.8, Piers 1 is at the ground floor and Piers 2 at the first floor.

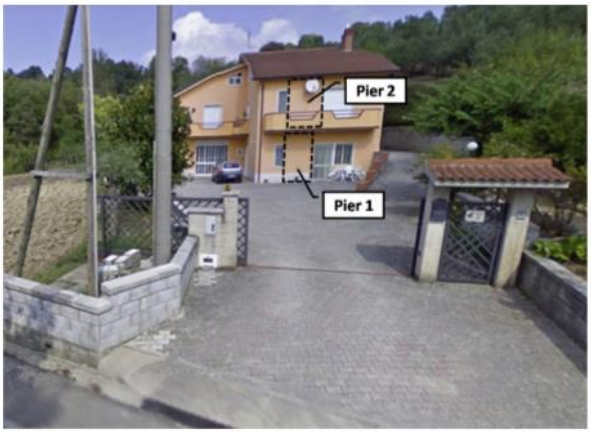

***Figure 4.8**: Structural components over the building façade*

Pressure-Impulse diagrams were built, assuming a medium pre-compression level for Pier 1 and a pre-compression level for Pier 2 (Figure 4.9 a) and b)).

From the analysis of the results, the values of probability of occurrence fall in a range between 2.1×10^{-4} and 1.7×10^{-1}. In the case of structural component Pier 1, 64% of the P-I combinations are located in the zone of the diagrams related to unsafe conditions, while in the case of Pier 2, 76% of unsafe conditions are reached.

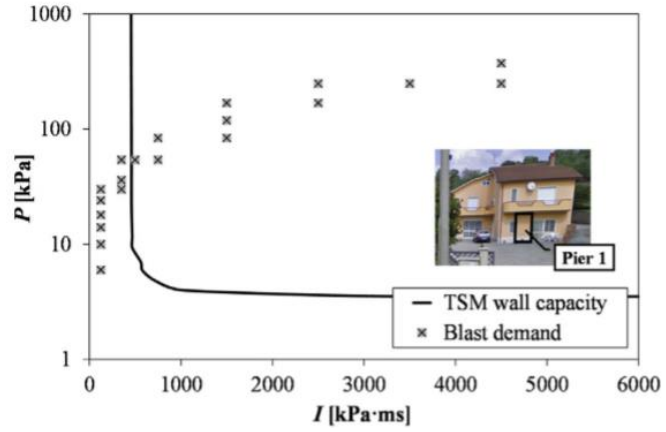

(a)

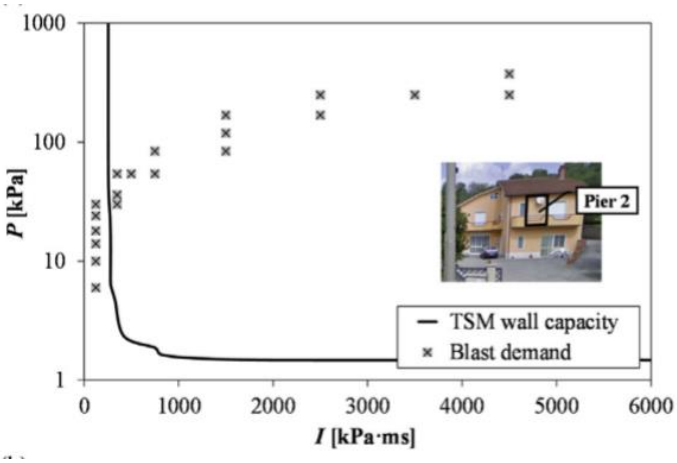

(b)

Figure 4.9: *Assessment of blast impact on structural components Pier 1 (a) and Pier 2 (b)*

4.5 Comparison between hydrogen and natural-gas pipelines

As reported in section 3.5, simulations for natural-gas were carried out in the same atmospheric and ground conditions, in order to realize a comparison with the hydrogen behaviour.

The effects of operating properties of natural gas pipeline were analysed and are reported in the following Figures. The charts are related to the explosivity class 6, but similar results are obtained in the case of explosivity class 9, too. As shown in Figure 4.10 a), the overpressure increases with increasing hole diameter and operating pressure. The maximum value of overpressure is reached in correspondence of a hole diameter of 0.9 m. It is noted a greater dependence on the increase in overpressure from the hole diameter than from the operative pressure.

On the contrary, the impulse increases mostly with the pressure than with the hole diameter.

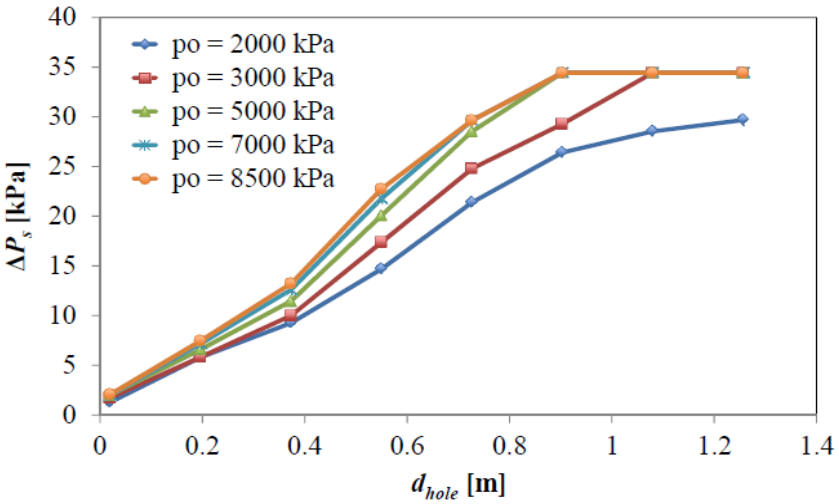

(a)

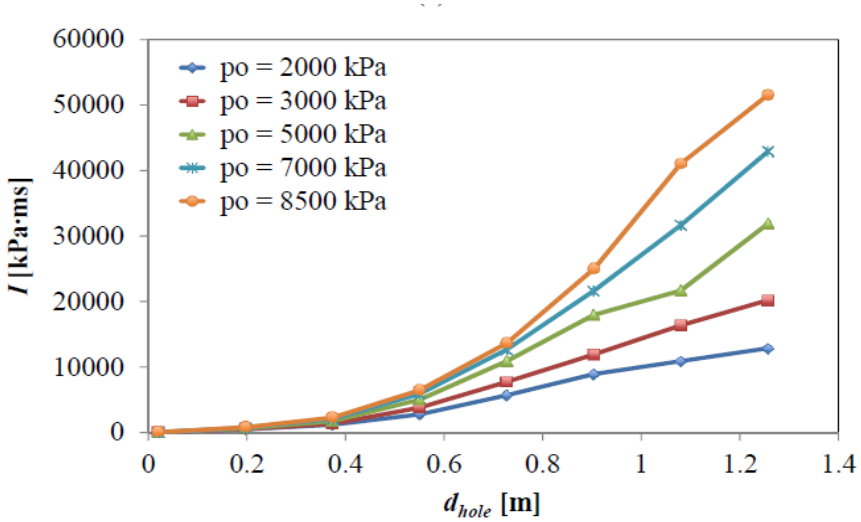

(b)

***Figure 4.10**: Natural gas pipelines: Peak of overpressure (a) and impulse (b) versus hole diameter at different value of operating pressure (d=1.257 m, L=1000 m, R=500 m, atmospheric stability class C, v= 10 m/s, explosivity class 6)*

In the case of hydrogen pipeline, a similar trend was observed (Figure 4.1), but the maximum overpressure was observed at a lower hole diameter (0.3 m) and in correspondence of a higher pressure (12800 kPa), since the natural gas pipelines works at lower pressures and with higher diameters.

Figure 4.11 a) and b) reports the overpressure and the impulse versus the length of pipeline from the gas supply station to the point of release. Both overpressure and impulse decrease with increasing the pipeline length (L), since at greater length the pressure into the pipeline

decreases. This trend is observed up to a value of L of about 3000 m; above 3000 m overpressure and impulse are quite constant.

In the case of hydrogen, the value at which the trend has become constant is 1000 m.

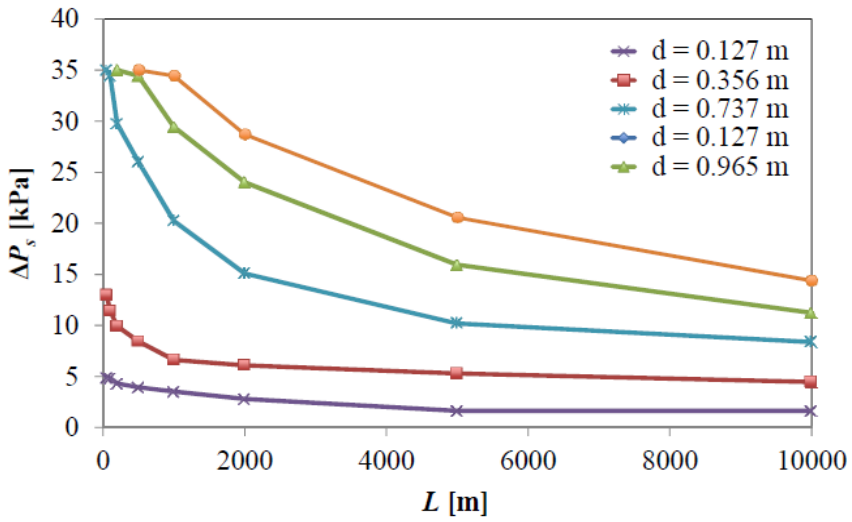

(a)

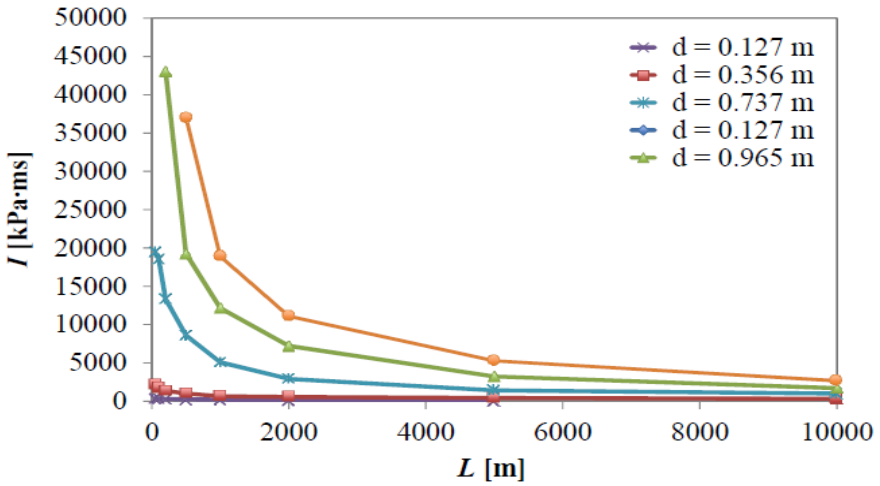

(b)

Figure 4.11 *: Natural gas pipelines: Peak of overpressure (a) and impulse (b) versus pipeline length from the centre of compression at different value of pipeline diameters (P_o=5000 kPa, R=500 m, full bore rupture, atmospheric stability class C, v= 10 m/s, explosivity class 6)*

Finally, a comparison of blast hazard evaluated both for hydrogen and natural gas were performed.

In the case of explosivity class 9, for natural gas, the value of 507 kPa has been obtained as maximum overpressure and of 300,000 kPa x ms as maximum impulse. For the class of explosivity 6, instead, lower values of overpressure and impulse are reached, 19 kPa and 30,000 kPa x ms, respectively.

For hydrogen the highest values achieved are 507 kPa and 60,000 kPa x ms, for the explosivity class 9 and 1 kPa and 125 kPa x ms, for the explosivity class 6, instead.

However, in all the cases analysed, higher values of impulse were found for natural gas with respect to hydrogen. This difference can be attributed to the most rapid hydrogen dispersion in the atmosphere, due to its lower density.

4.6 Damage to people involved in an explosion

The annual probability of damage to people involved in the explosion event has been evaluated. Two different classes of explosivity, with low (class 6) and high (class 9) ignition power and two different Pasquill atmospheric stability classes, D (neutrally stable) and F (moderately stable) at wind velocities of 5 and 2 m/s, respectively, have been taken into consideration.

Based on the analysis of the results, it was noted that the highest probability to reach the maximum pressure and impulse occurred in the case of stability class F at wind velocity of 2 m/s, since this is the scenario among those considered, in which the phenomenon of dispersion is slower.

The results related to the probability of fatality due to lung haemorrhage, head impact and whole-body impact for different combinations of overpressure and impulse are shown in Figure 4.12, 4.13, 4.14, in the conditions of the worst case scenario, referred to explosivity class 9 and atmospheric conditions F2.

The higher fatality probabilities were obtained considering head and whole-body impacts against obstacles, and a value of 1.605×10^{-3} death/year/1000 km was the maximum value achieved for an overpressure of 507 kPa and impulse of 12,500 kPa x ms, relating to the head impact.

Taking into account death due to lung haemorrhage, same combination of overpressure and impulse led to the higher probability of death, too.

Subsequently, acceptance criteria were considered in order to interpret the results obtained. These criteria are usually used to demonstrate that the risk related to the given hazard is acceptable or tolerable.

According to ISO/IEC Guide 73:2002, the risk is defined as the "*combination of the probability of an event and its consequence"*.

Acceptable levels of risk or risk acceptance criteria are established by the society, so as to build up risk-informed codes, primarily concerning people injury or death (Saffers and Molkov, 2014).

Different criteria for determining the individual harm exposure threshold value are reported in literature, even if there should be a legitimate basis, accepted by authorities and by most people.

EIGA (2007) proposed a value of 3.5×10^{-5} per year as individual harm exposure threshold in order to determinate the safety distances. Instead, defining the risk criteria, HSE (2013) has identified the risks involving single and multiple fatalities, and assigned the values of 10^{-3} per year, 10^{-4} per year and 10^{-6} per year as the maximum tolerable risk for workers, public and acceptable in general, respectively. So, negligible risks are considered below a value of 10^{-6} per year (DNV, 2015). Same value for the maximum acceptable individual risk is assigned in the Netherlands (DNV, 2015).

In view of this, the acceptance criteria used to evaluate the risk levels related to people involved in accidental hydrogen explosions are 10^{-6} per year (DNV, 2015).

As shown in the Figure 4.12, 4.13, 4.14, taking into consideration a threshold value of 10^{-6} per years/1000 km, several combinations of overpressure and impulse can cause high probability of death. In the case of death due to lung haemorrhage (Fig. 4.12), values of overpressure that overcome the acceptance value are higher than 249 kPa; combinations of overpressure and impulse with major probability of death are related to 374 kPa and 12500 kPa x ms, 478 kPa and 4500 kPa x ms, and 507 kPa and 12500 kPa x ms.

In the case of head impact (Fig. 4.13), values of 54 kPa and 7500 kPa x ms are already sufficient to exceed the threshold value. However, the higher probabilities of death are achieved for values of overpressure that get over 169 KPa. A similar trend is observed in the case of death to whole-body impact (Fig. 4.14).

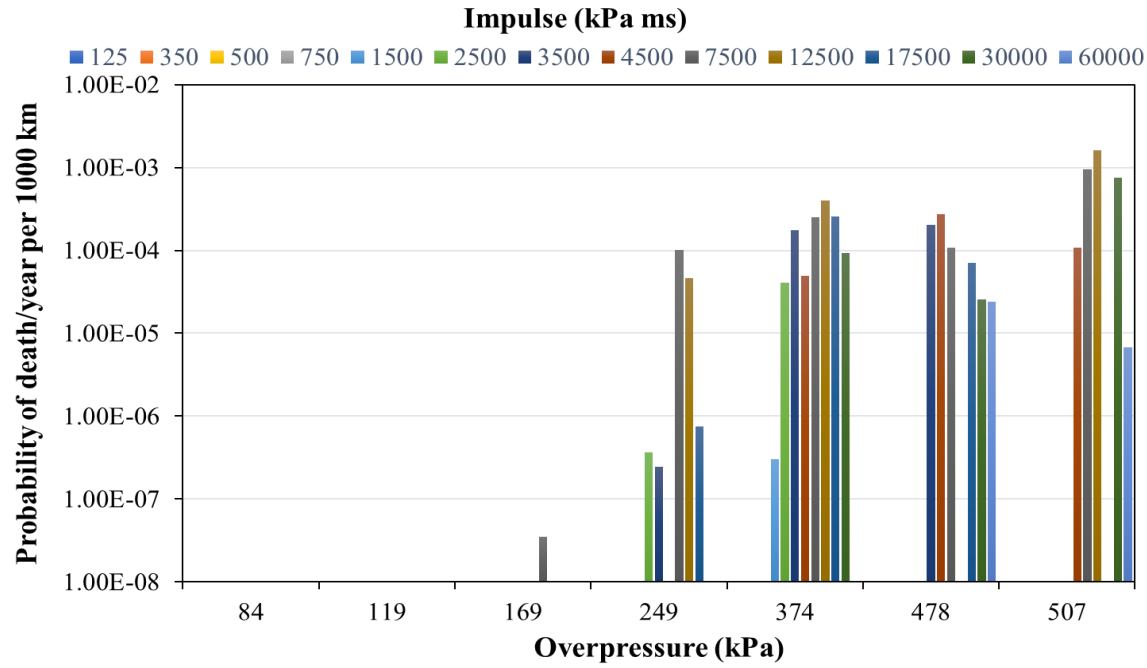

***Figure 4.12**: Probability of death due to lung haemorrhage for explosive class 9 and atmospheric stability class F2*

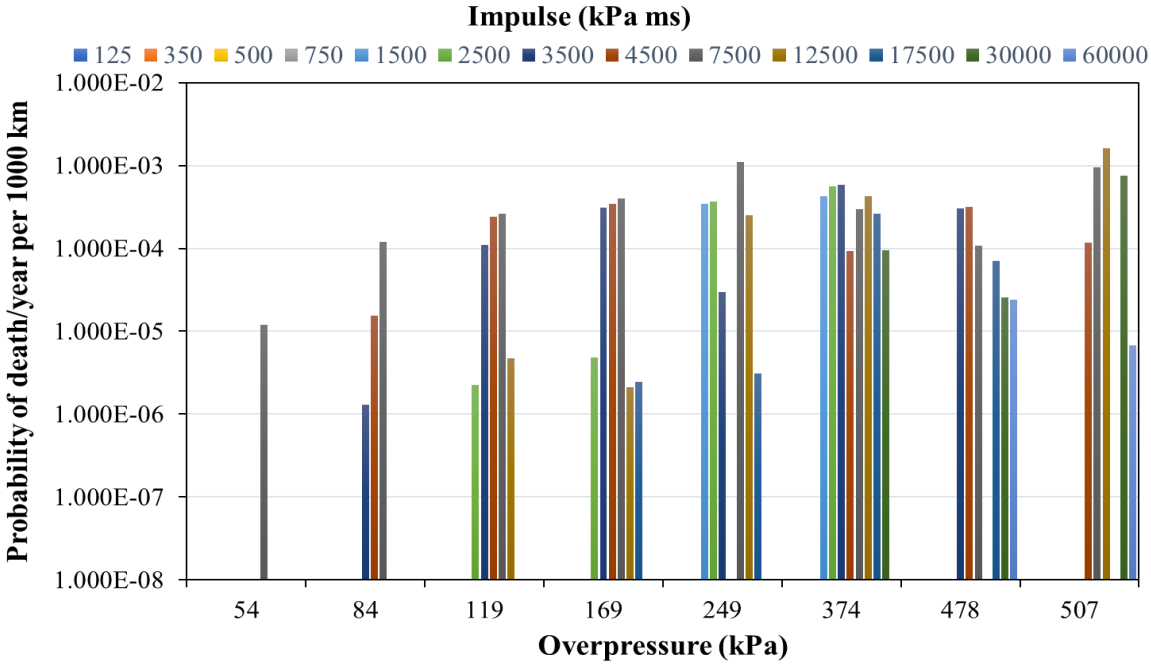

***Figure 4.13**: Probability of death due to head impact for explosive class 9 and atmospheric stability class F2*

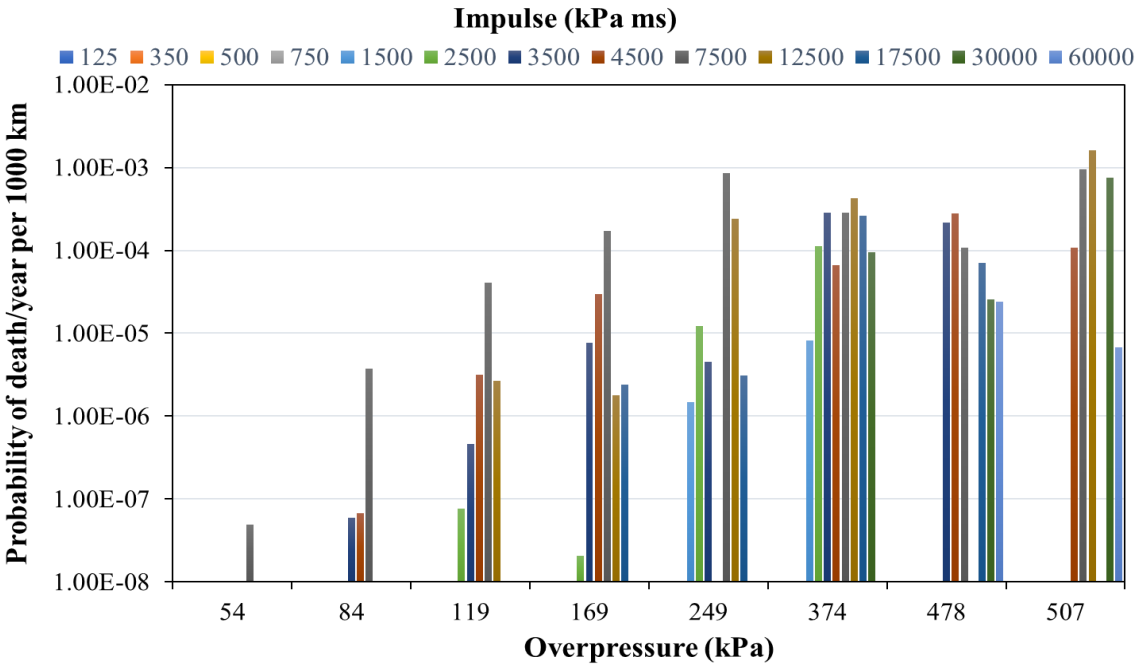

***Figure 4.14**: Probability of death due to whole body impact for explosive class 9 and atmospheric stability class F2*

Based on these acceptance criteria, in the case of explosivity class 9 and atmospheric conditions F2 the highest values were reached and the estimated probability of death is not acceptable. In contrast, lower values (10^{-11} death/year/1000 km) were achieved in the case of explosivity class 6 and atmospheric conditions F2, well below the threshold criteria.

Regarding the probability of injuries, higher values than the risk acceptance criteria are achieved when the overpressure exceeds 10 kPa, in both explosivity classes 6 and 9 and in the atmospheric stability class F2. In Figure 4.15 the results related to explosivity class 9 are reported.

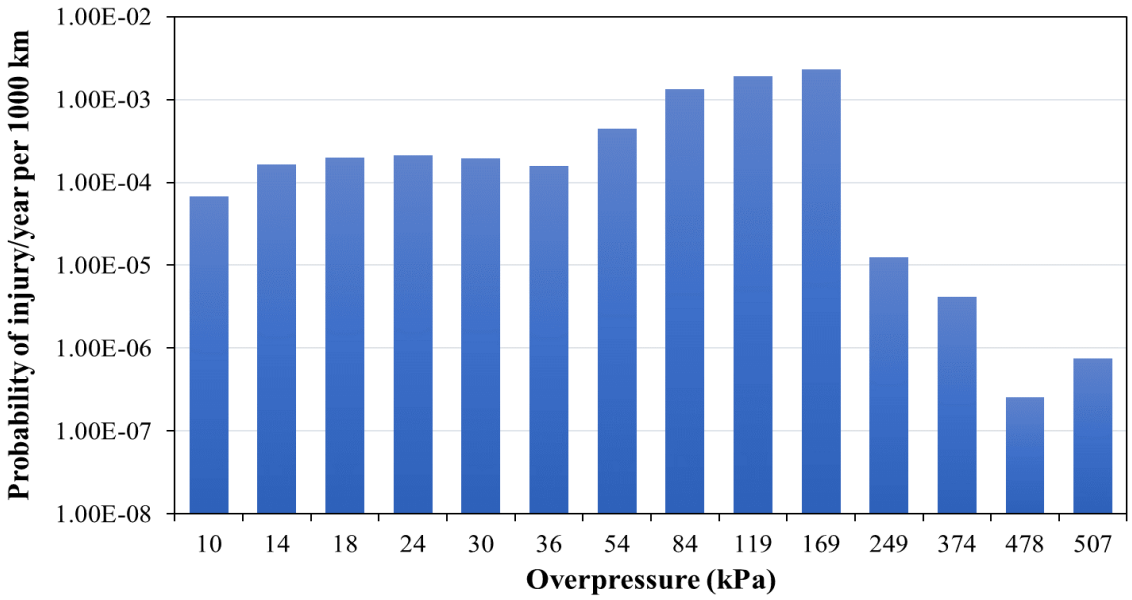

***Figure 4.15**: Probability of injury due to eardrum rupture for explosive class 9 and atmospheric stability class F2*

4.7 Fire hazard

The results of simulations were analysed in terms of the radiative heat flux arising from a jet fire. Varying the pipeline operating properties and the source release properties in the ranges illustrated in the previous sections, different values of heat flux have been evaluated.

The highest value of radiative heat flux reached is about 1630 kW/m^2, at the maximum value of operating pressure (12.8 MPa), with pipeline diameter of 0.508 m, and a distance from the compression station (L) of 50 m. It is achieved at the minimum distance (taken into consideration) of the target from the pipeline of 10 m.

The effect of pipeline operation properties on the radiative heat flux were investigated.

The Figure 4.16 reports the radiative heat flux versus the hole diameters (dhole) in conditions of atmospheric stability class F2, for a pipe diameter d=0.508 m and a length of pipeline from the point of compression L= 1000 m, at different pipeline operating pressures. A distance of 200 m from the centre of the jet fires (r) is assumed.

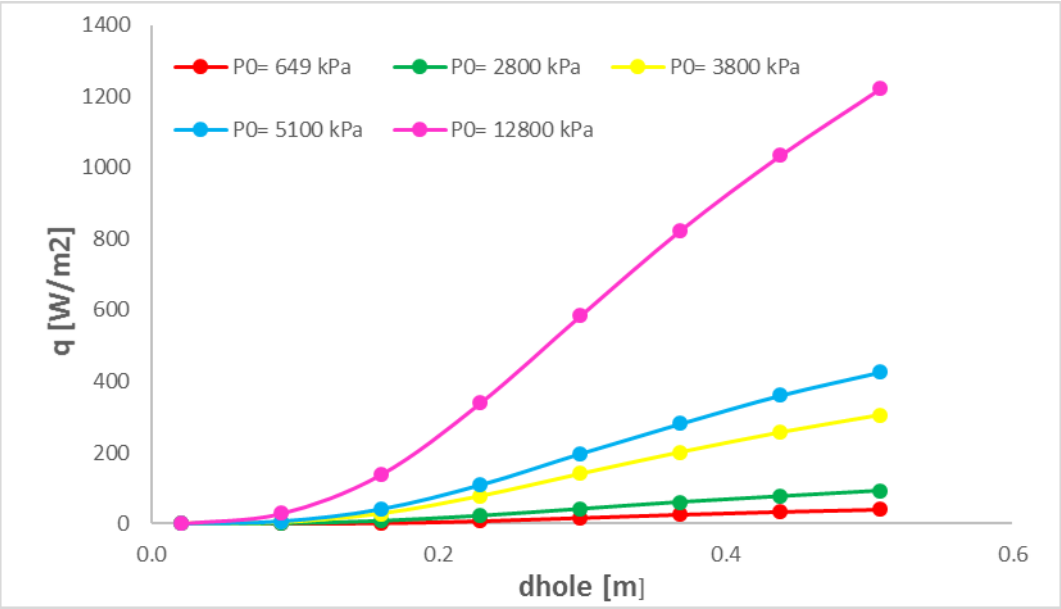

***Figure 4.16**: Radiative heat flux versus hole diameter (d=0.508 m, r= 200 m,L=1000 m, atmospheric stability class F, v= 2 m/s)*

As shown in Figure 4.16, as the hole diameter was increased, the radiative heat flux increased and this trend is more evident for the higher values of operative pressure. In more detail, for P_0=12800 kPa, the radiative heat flux varies from 0.77 W/m^2 in correspondence of the minimum d_{hole} considered to 1222 W/m^2 in correspondence of the full rupture of diameter.

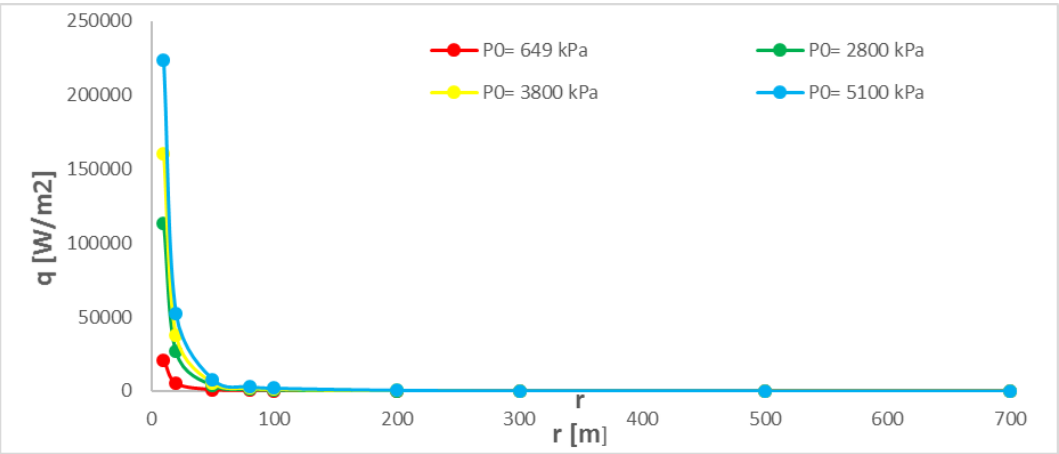

***Figure 4.17**: Radiative heat flux versus hole distance to the center of the jet fires (d=0.508 m, d_{hole} = d (full rupture),L=1000 m, atmospheric stability class F, v= 2 m/s)*

On the contrary, when the distance from the center of the jet fires is increased, the radiative heat flux decreases, as shown in Figure 4.17.

4.8 Damage to people due to jet fire

The evaluation of radiative heat flux generated by a jet fire allowed the estimation of the annual probability of damage to people. Atmospheric conditions denoted as F2 were taken into considerations, they are those that correspond to the greater stability. Distances between 10 m and 700 m from the centre of the jet fires were assumed.

Since the harm level depends not only on the radiative heat flux, but also on the duration of exposure, three different times were assumed (60 s, 300 s, and 600 s).

People exposed to high radiative heat fluxes for sufficient time may be damaged in terms of fatalities or injuries, resulting in first or second-degree burns. The Probit equations 3.37, 3.38 and 3.39 previously reported, were used for the evaluation of lethality, first degree burns and second-degree burns, respectively.

In the following figures 4.18- 4.29 the results obtained, for the three values of exposure time considered 60s, 300s, and 600s, respectively, are reported.

As frequency of rupture of hydrogen pipeline a value of 0.126 /year per 1000 km was employed (Air Liquide, 2005).

For a period of exposure of 60 s, the highest probability of fatality caused by a jet fire is 1.2 x 10^{-2} /year per 1000 km in correspondence of a radiation heat flux of 15000 W/m^2, at a distance of 10 m (Figure 4.18). At the same distance and for the same radiative heat flux, the probability of injuries reaches a maximum value of 2.4 x 10^{-2}/year per 1000 km, as shown in Figure 4.19.

More in detail, according to the chosen threshold criteria (10^{-6}/year per 1000 km), at a time of exposure of 60 s, probability fatalities caused by radiative heat fluxes lower than 3800 W/m^2 is acceptable, regardless of the distance considered. However, exceeding this value, for radiative heat fluxes of 7500-15000 W/m^2 the probability of death up to a distance of 100 m is not acceptable (3.34 x10^{-4} - 1.20 x10^{-4}/year per 1000 km,). This distance is reduced to 80 m for radiative heat flux of 25000 W/m^2, to 50 m for radiative heat flux in the range 25000-45000 W/m^2 and to 20 m for radiative heat flux in the range 125000-325000 W/m^2. For higher values of radiative heat flux the fatality occurs at a distance of 10 m.

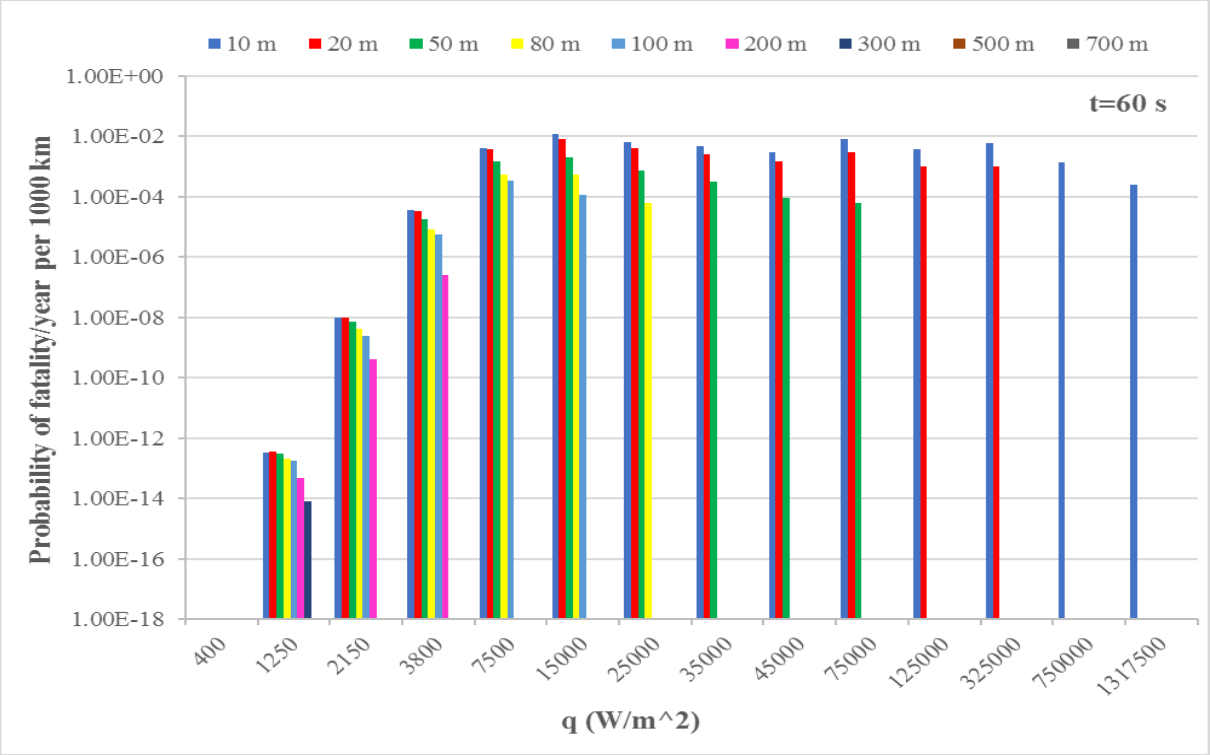

Figure 4.18: *Probability of fatality due to radiative heat flux (W/m^2) at different distances at t=60 s.*

Regarding the injuries (Figure 4.19), a value of heat flux of 2150 W/m^2 can cause damage with a probability of 4.30 x 10^{-4} /year per 1000 km up to a distance of 200 m. However, the highest probability of injuries (2.46 x 10^{-2} /year per 1000 km) occurs in correspondence of a radiative heat flux of 15000 W/m^2 at a distance of 10 m from the centre of the jet fire.

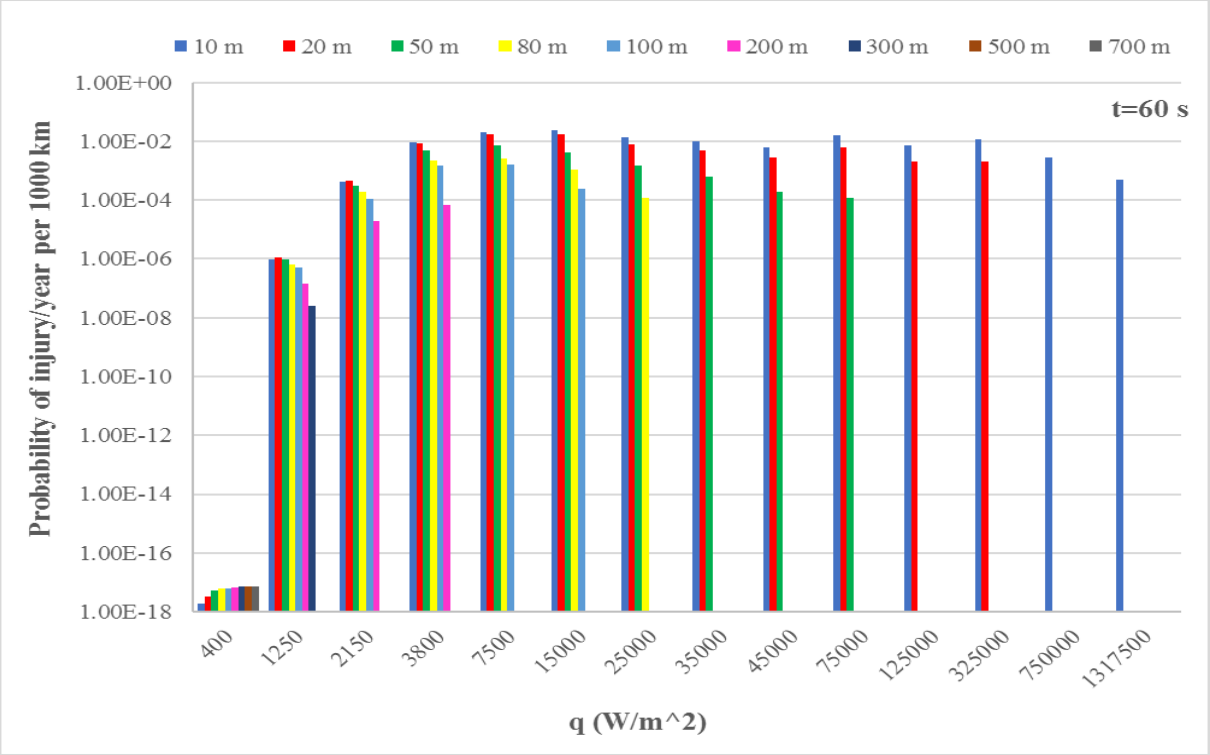

Figure 4.19: *Probability of overall injuries due to radiative heat flux (W/m^2) at different distances at t=60 s*

Comparing Figures 4.20 and 4.21 at 60 s of exposure time, the probabilities of second-degree burns are lower than those due to first degree burns and become higher than threshold value (10^{-6}/year per 1000 km), for radiative heat flux equal or higher than 3800 W/m^2.

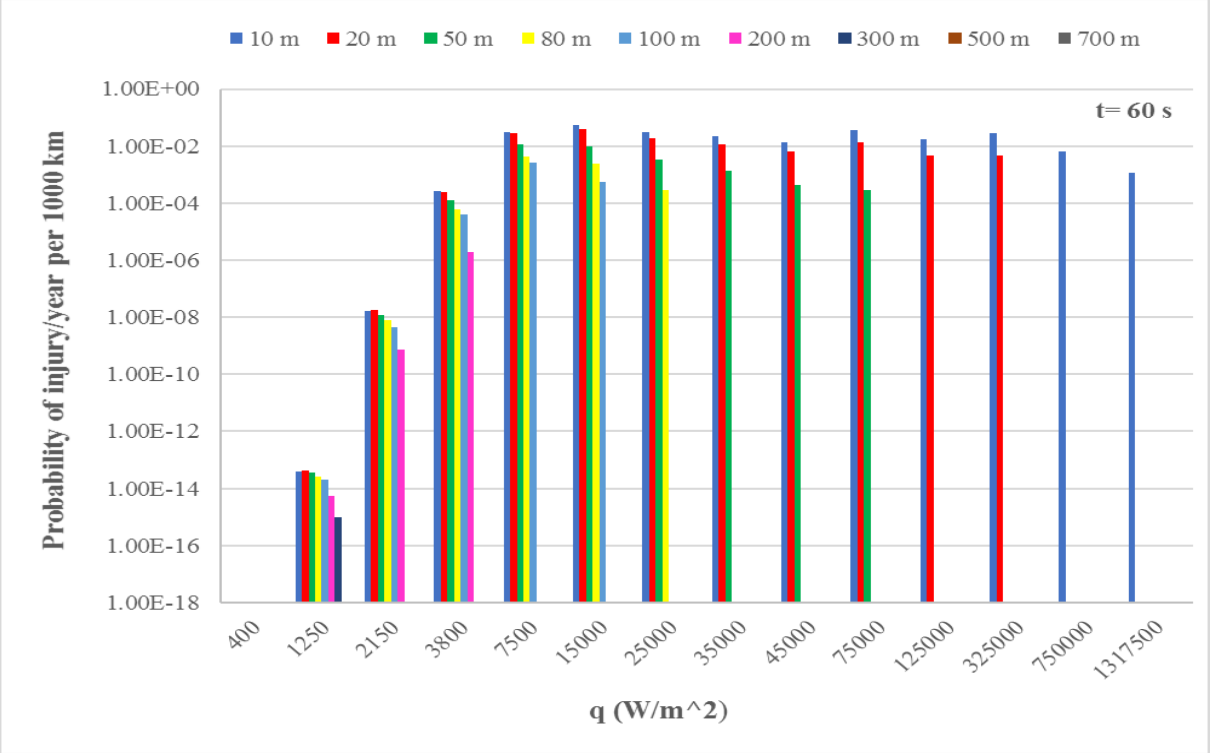

Figure 4.20: *Probability of injury due to second-degree burns at different distances at t=60 s*

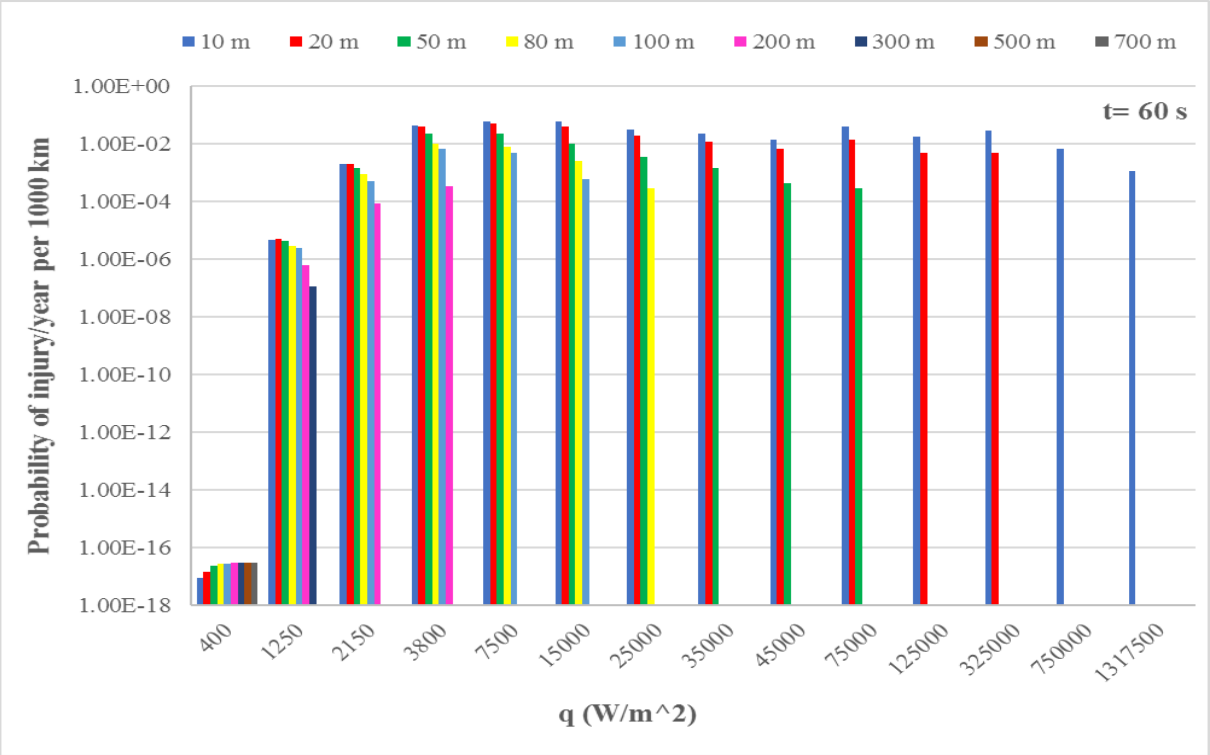

Figure 4.21: *Probability of injury due to first-degree burns at different distances at t=60 s*

For longer exposure times, both the probabilities of fatalities and injuries are considerable higher and the damage occurs already for low values of radiative heat flux and at larger distances from the flame.

Specifically, at 300 s, probabilities of fatality higher than 10^{-6}/year per 1000 km are observed for radiative heat flux of 1250 W/m^2 up to a distance of 300 m (Figure 4.22).

The probability of fatality increases with increasing the intensity of heat flux and it achieves a maximum in correspondence of 3800 W/m^2 up to a distance of 200 m.

At distances of 50 m, 80 m and 100 m, the probability values are 5.70 x 10^{-3}, 2.69 x 10^{-3} and 1.80 x 10^{-3}/year per 1000 km, respectively.

Moreover, at a distance of 10 m probability of fatality are not negligible in the whole range 1250-1317500 W/m^2 of the radiative flux.

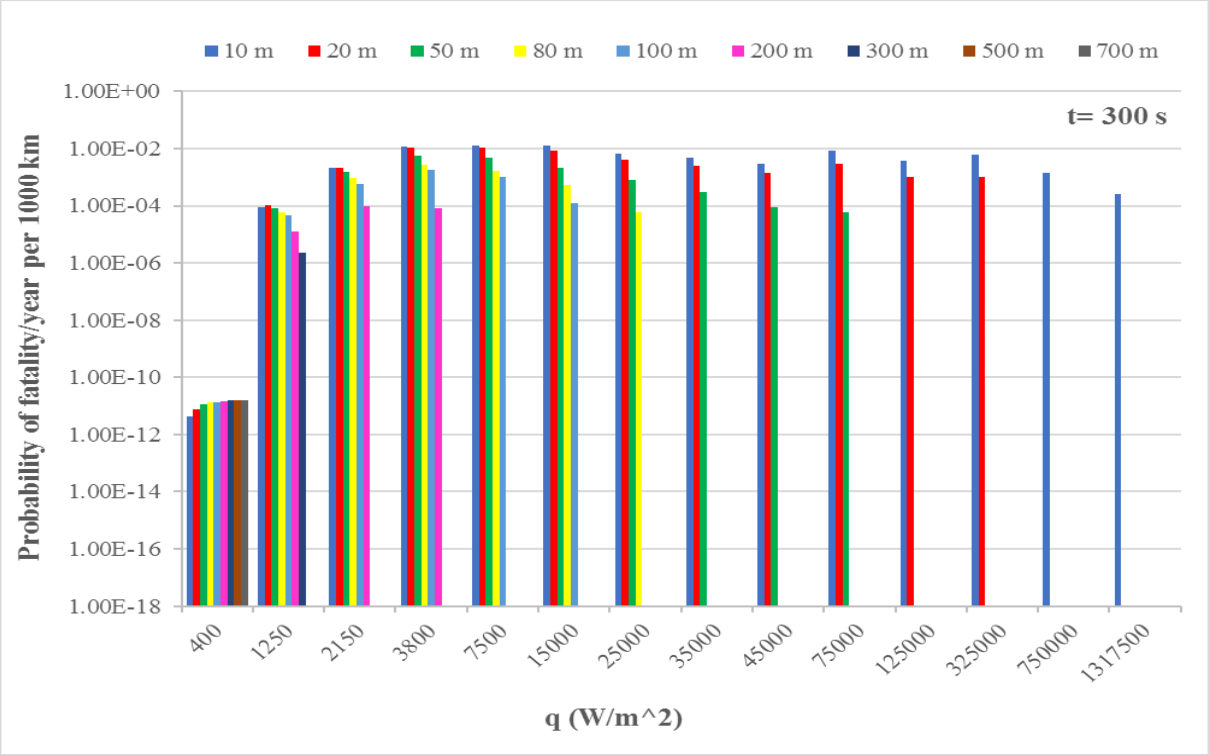

Figure 4.22: *Probability of fatality due to radiative heat flux (W/m^2) at different distances at t=300 s*

Regarding the injuries (Figure 4.23), all the values of radiative flux obtained lead to a probability of damage that overcomes the threshold value (10^{-6}/year per 1000 km) at t=300 s. Injuries are expected up to a distance of 700 m, but the maximum probability (2.51 x 10^{-2}/year per 1000 km) is observed at a distance of 10 m and for 7500 W/m^2.

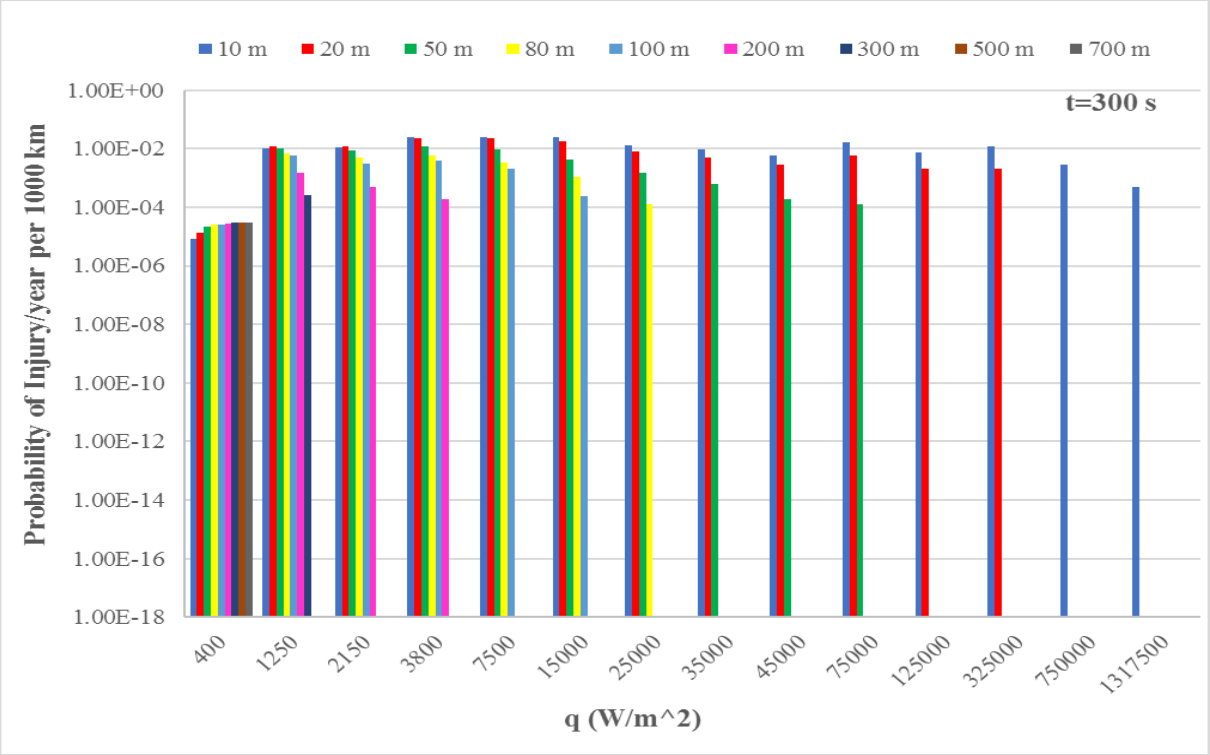

Figure 4.23: *Probability of overall injuries due to radiative heat flux (W/m^2) at different distances at t=300 s*

Analysing the first and second degree burns in detail (Figure 4.24 and 4.25), at the smallest value of radiative heat flux (400 W/m^2) first-degree burns have a probability higher than the threshold value while second-degree burns only at heat fluxes higher than 1250 W/m^2.

For first-degree burns, probabilities over the acceptance threshold limit are observed until 700 m, with a value of 7.96 x 10^{-5} /year per 1000 km.

In the case of injuries for second-degree burns, damage is observed until 300 m with a probability of 1.11 x 10^{-5}/year per 1000 km at 1250 W/m^2.

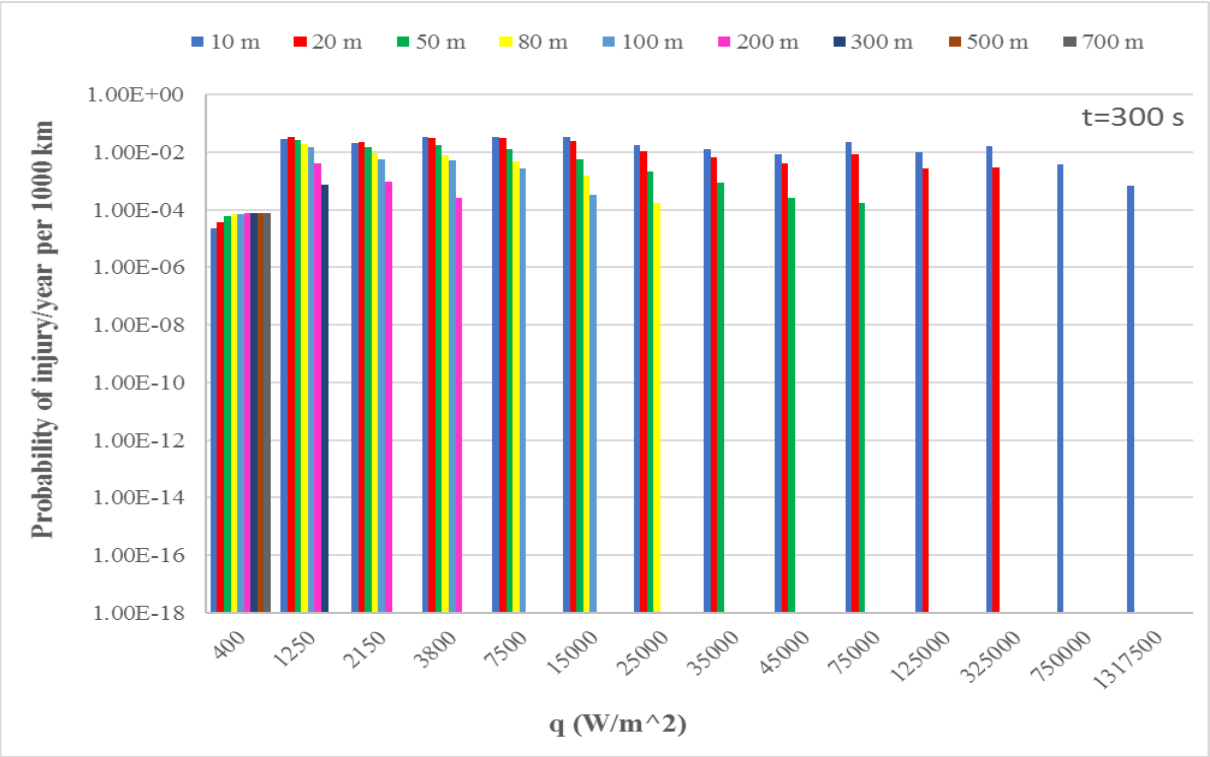

Figure 4.24: *Probability of injury due to first-degree burns at different distances at t=300 s*

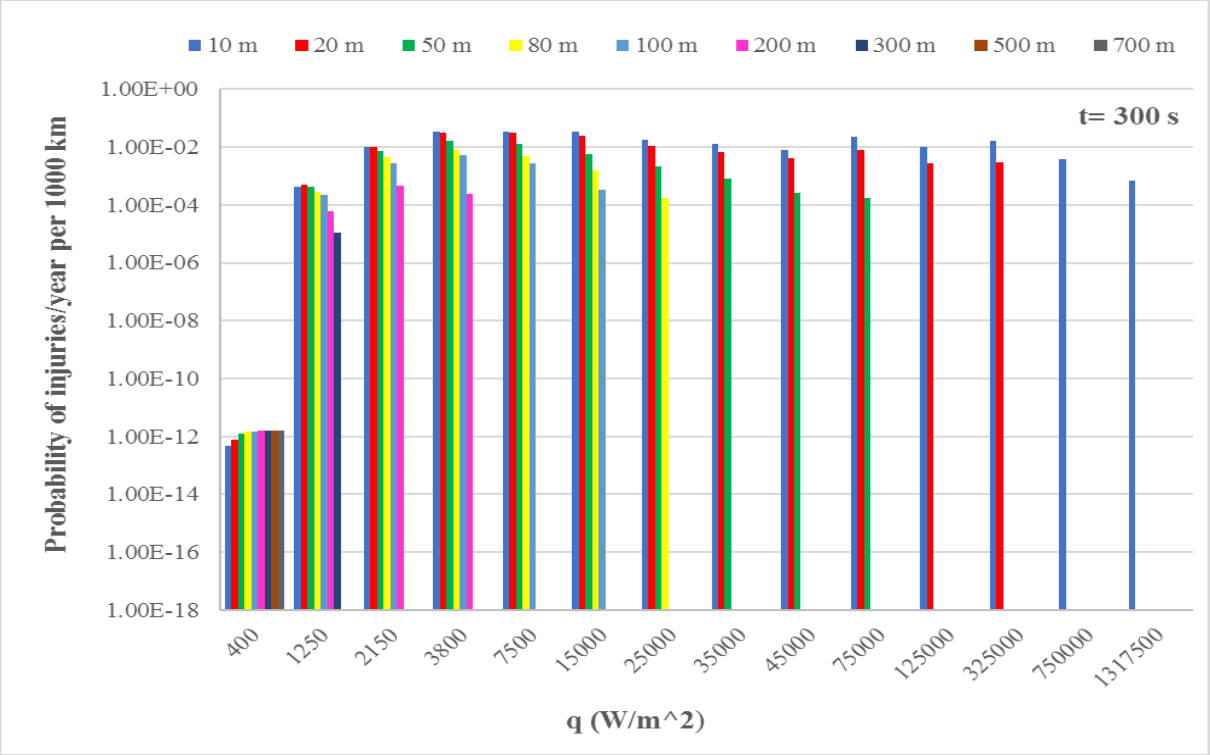

Figure 4.25: *Probability of injury due to second-degree burns at different distances at t=300 s*

The longest exposure time of 600 s was chosen as extreme value, considering that it takes into account the inability of escape. As expected, the probabilities of damage that occur are consequently very high.

In Figures 4.26, 4.27, 4.28, and 4.29, the results obtained for an exposure time of 600 s, corresponding to the complete flame duration, are reported.

As shown, the probability of fatality (Figure 4.26) does not achieve values that exceed the acceptance criteria of 10^{-6}/year per 1000 km only in correspondence of the lowest class of radiative heat flux taken into account (400 W/m^2). At a distance of 300 m a probability of 7.78 x 10^{-5}/yearper 1000 km fatality rate was found.

Furthermore, all the combinations of heat flux and distance cause damage in terms of injuries (Figure 4.27), and specifically probabilities of first degree burns are not acceptable already at 400 W/m^2 (Fig. 4.28), whereas those for second degree burns are not for heat fluxes higher than 1250 W/m^2 (Figure 4.29).

For first-degree burns a probability of 10^{-2}/year per 1000 km is observed up to a distance of 700 m, while for second-degree burns maximum distance is 300 m (2.87 x 10^{-4}/year per 1000 km at 1250 W/m^2).

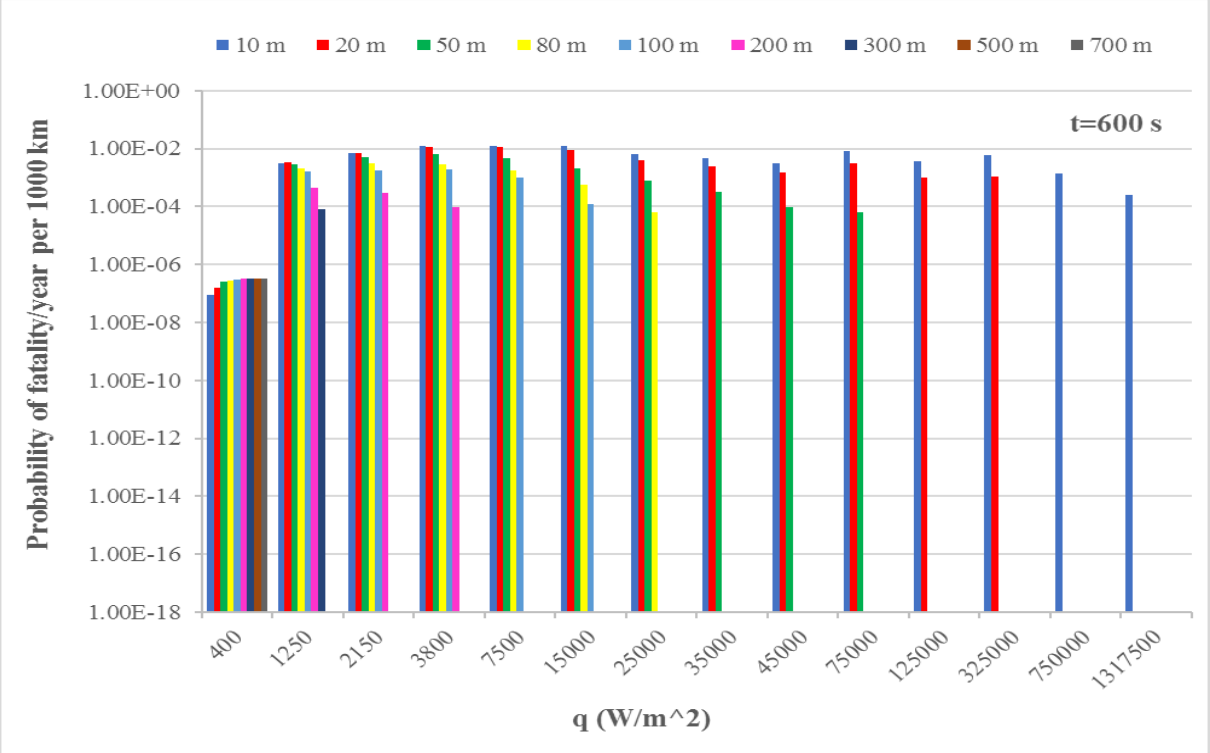

Figure 4.26: *Probability of fatality due to radiative heat flux (W/m^2) at different distances at t=600 s*

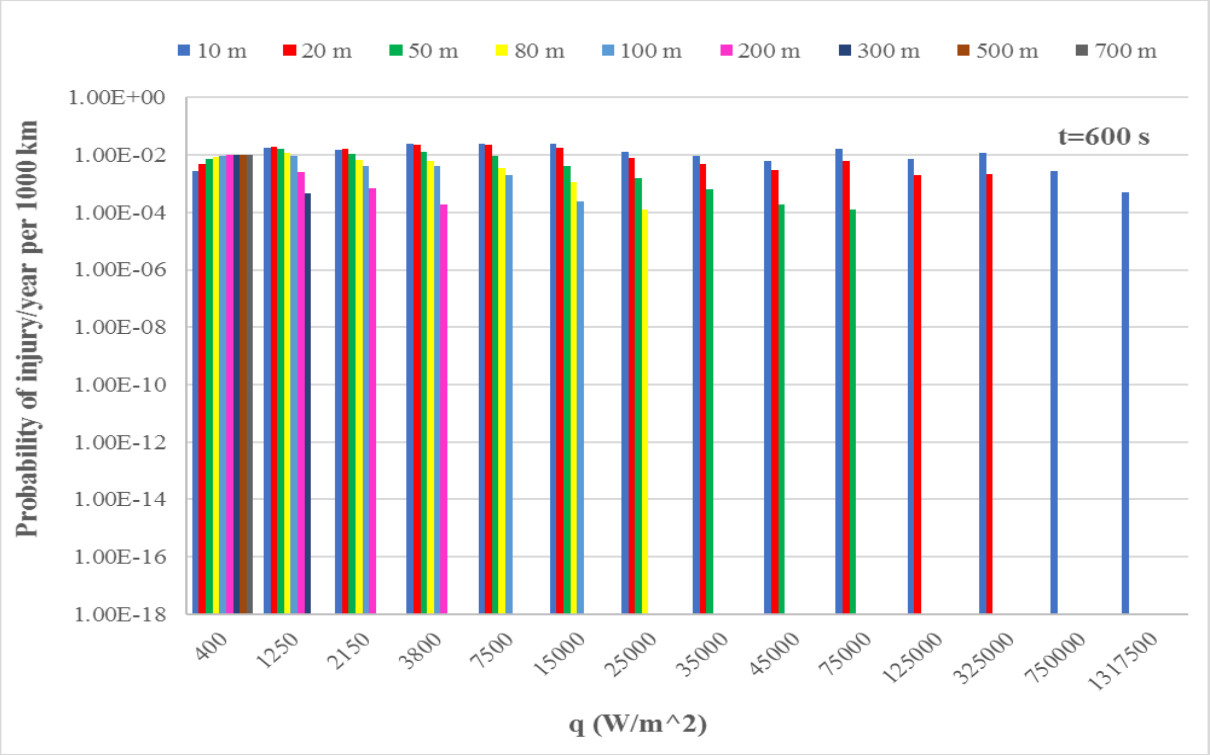

Figure 4.27: *Probability of overall injuries due to radiative heat flux (W/m^2) at different distances at t=600 s*

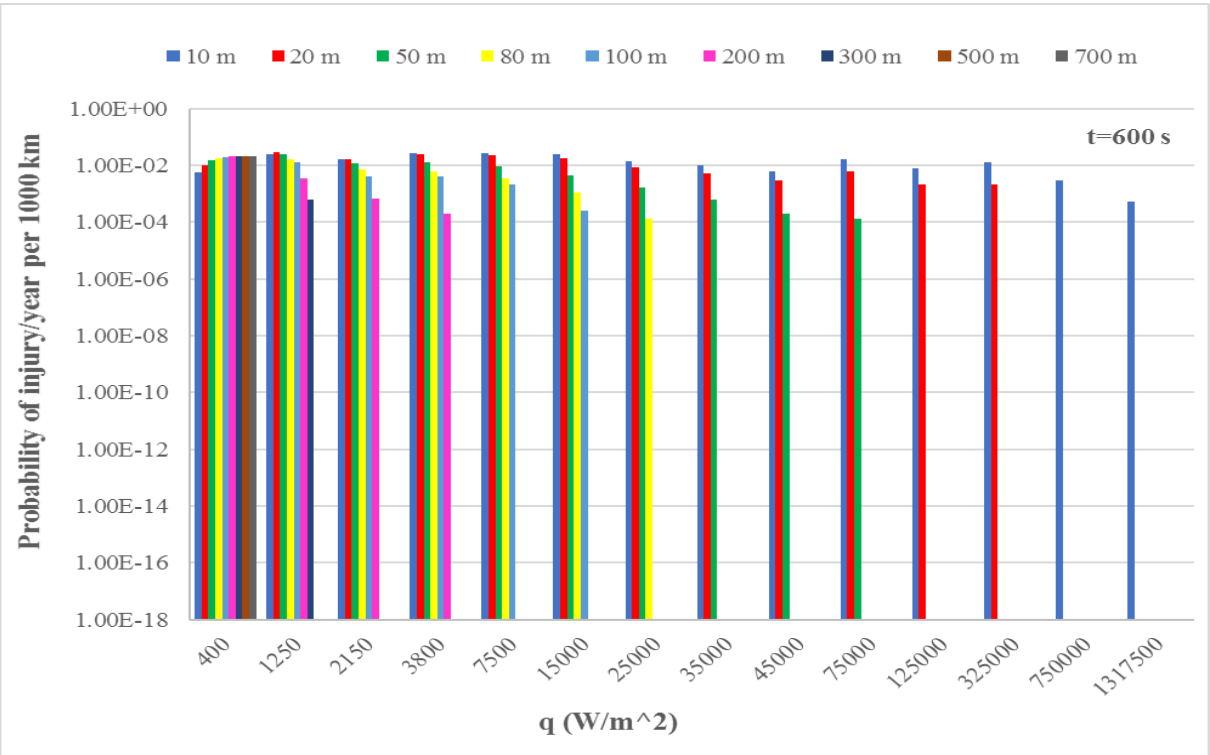

Figure 4.28: *Probability of injury due to first-degree burns at different distances at t=600 s*

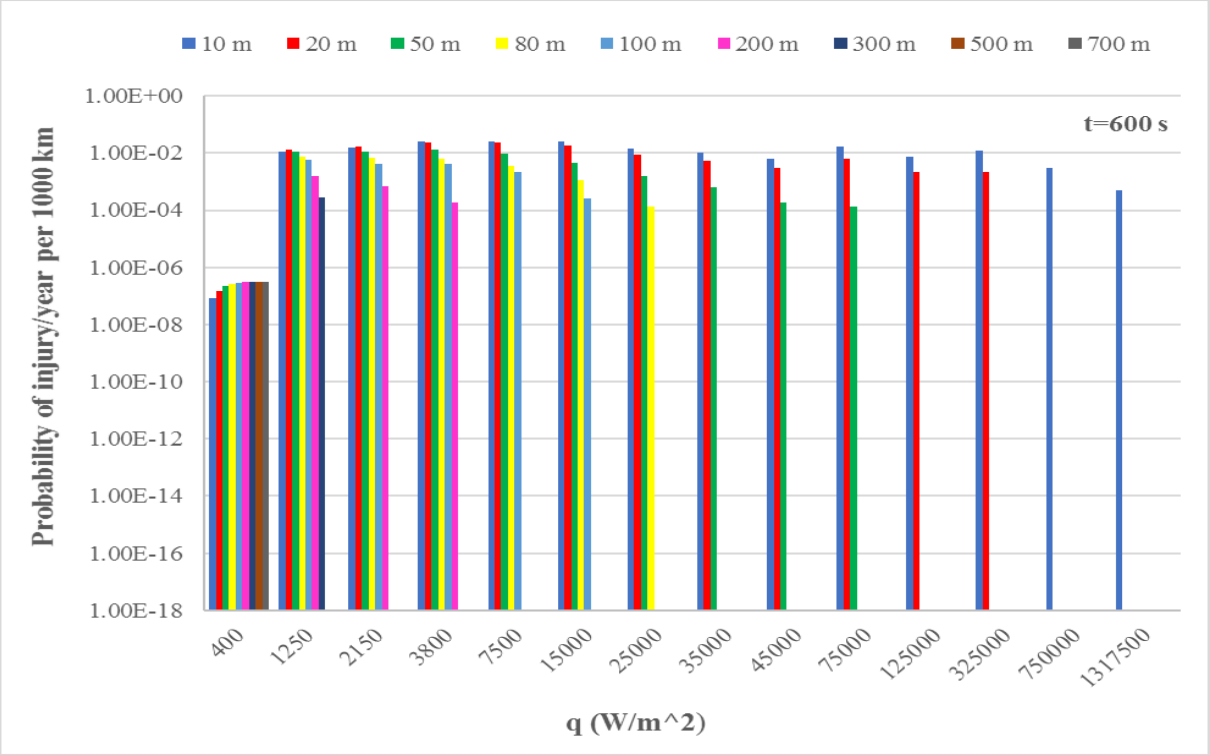

Figure 4.29: *Probability of injury due to second-degree burns at different distances at t=600 s*

Extended exposure to jet fires will increase both probability of fatality and injury that always overcome the acceptance criteria for the lower value of radiative heat flux considered. However, a time of 10 min is enough to allow people who are in the vicinity of the fires to escape and thus to avoid being overwhelmed and seriously damaged by the flame generated.

4.9 Damage to structures due to jet fire

Since Probit functions in terms of thermal effects on structures and equipment are not available in the literature, it was not possible to perform a probabilistic analysis in this case.

However, the maximum value of radiative heat flux reached at various distances from the pipeline and at the atmospheric conditions denoted as F2 was evaluated, and the correspondent damage was estimated, as shown in Figure 4.30.

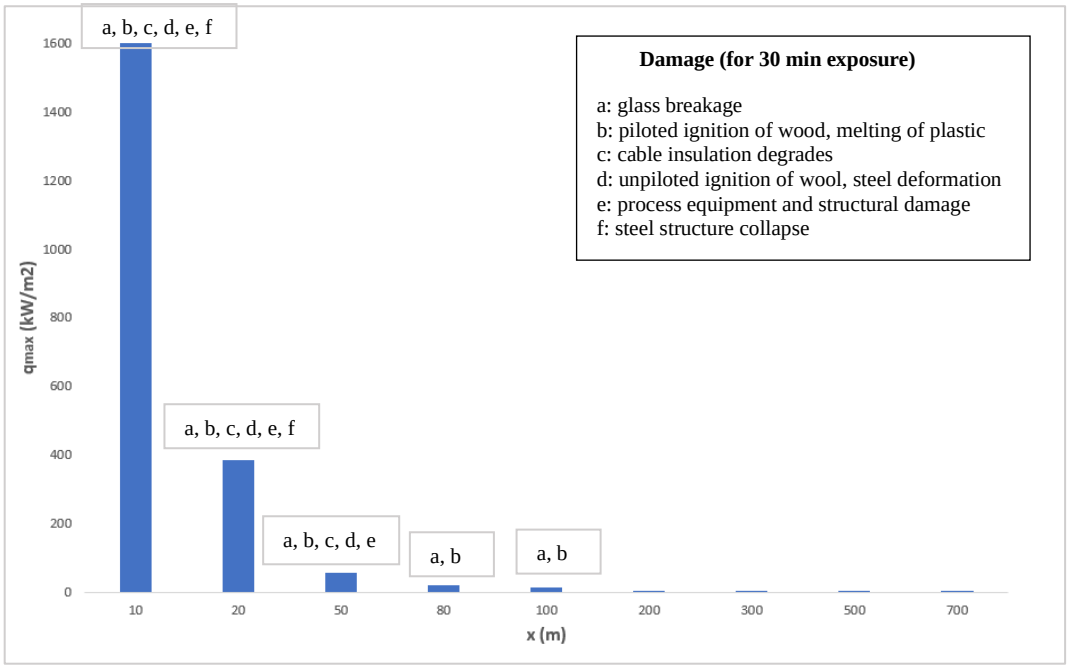

Figure 4.30: *Maximum value of radiative heat flux (kW/m^2) vs distance (m)*

According to the values reported in Table 3.17 for exposure time of 30 min, damage to structures occurs up to 100 m distance from the pipeline, even if the damage is minor (i.e. glass breakage, piloted ignition of wood and melting of plastic).

At a distance of 50 m, the exposure to a maximum value of radiative heat flux of 56 kW/m^2 can cause process equipment and structural damage.

Instead, more substantial damage occurs at distances of 10 and 20 m, where the values of radiative heat flux of 1632 kW/m^2 and 383 kW/m^2, respectively, are reached. At these distances the collapse of steel structures can also occur.

4.10 Safety distance

Finally, a minimum safety distance from the hydrogen pipeline was estimated. A threshold value of 10^{-6}/year per 100 km has been chosen as acceptable risk level, in accordance with the previous considerations. The results are reported in Figure 4.31, 4.32 and 4.33, for the three exposed times chosen.

Depending on the duration of exposure, different safety distances are evaluated. For stability class F and wind velocity of 2 m/s, for an exposure time of 60 s, a distance of 220 m can be considered as safety distance for injuries, as shown in Figure 4.31. In the case of fatalities, it reduces to 190 m.

Increasing the exposure time to 300 s, the safety distance increases up to an achieved a value of 700 m for injuries (Figure 4.32). This value decreases to about 300 m for fatalities. Finally, large exposure time (600 s) requires higher safety distance over 800 m for injuries and about 520 m for fatality (Figure 4.33).

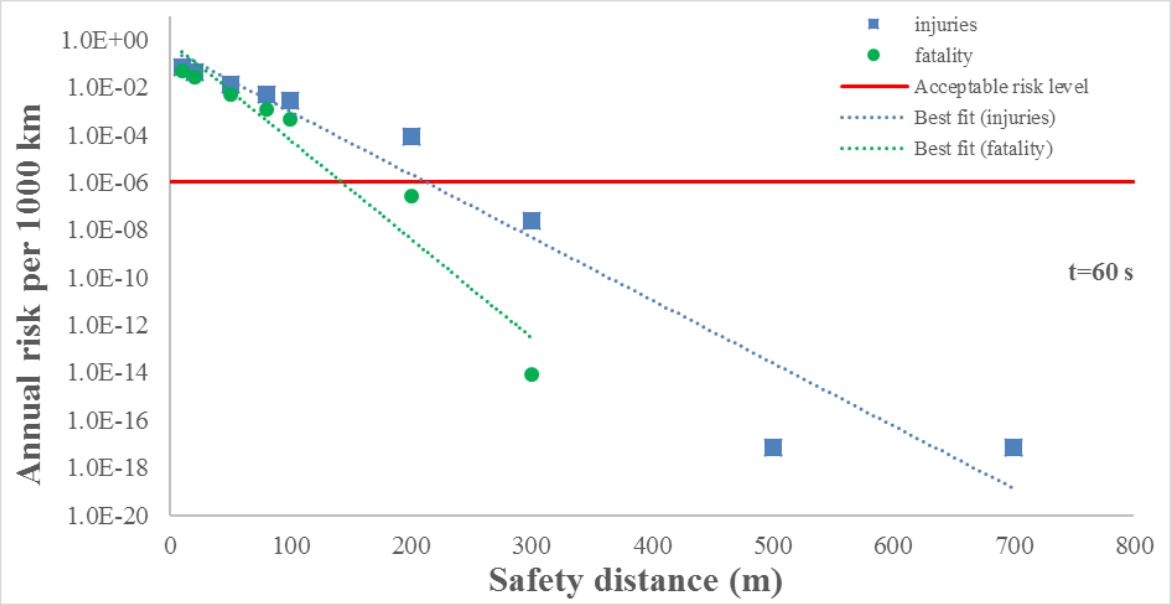

Figure 4.31: *Annual risk per 1000 km of damage to people (injuriess and fatality) vs safety distance, in the case of atmospheric stability class F2, at t=60 s*

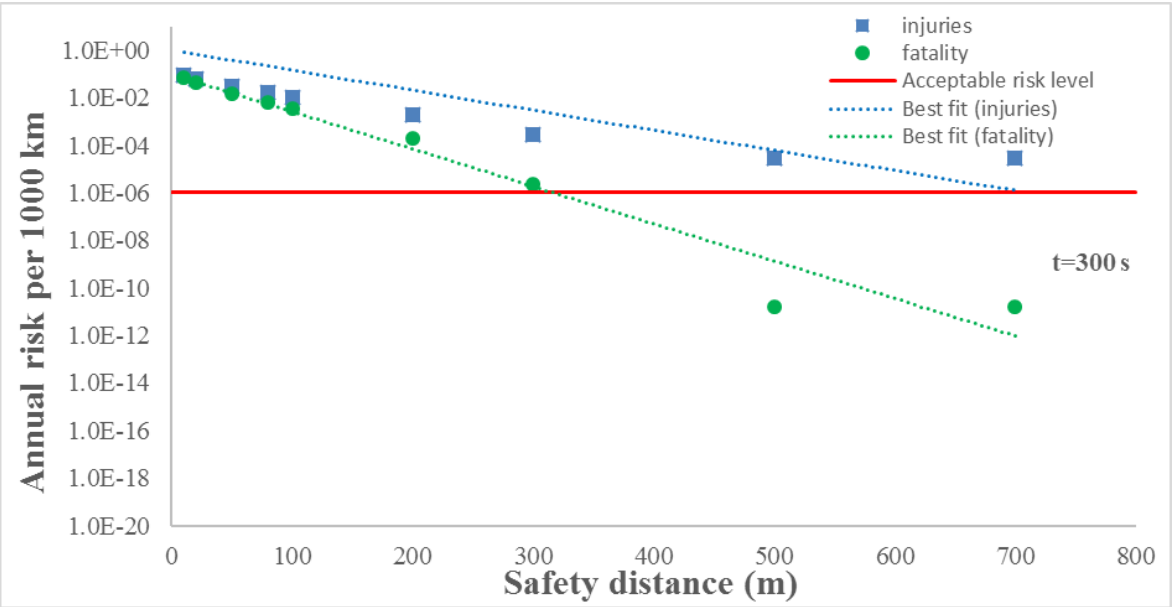

Figure 4.32: *Annual risk per 1000 km of damage to people (injuries and fatality) vs safety distance, in the case of atmospheric stability class F2, at t=300 s.*

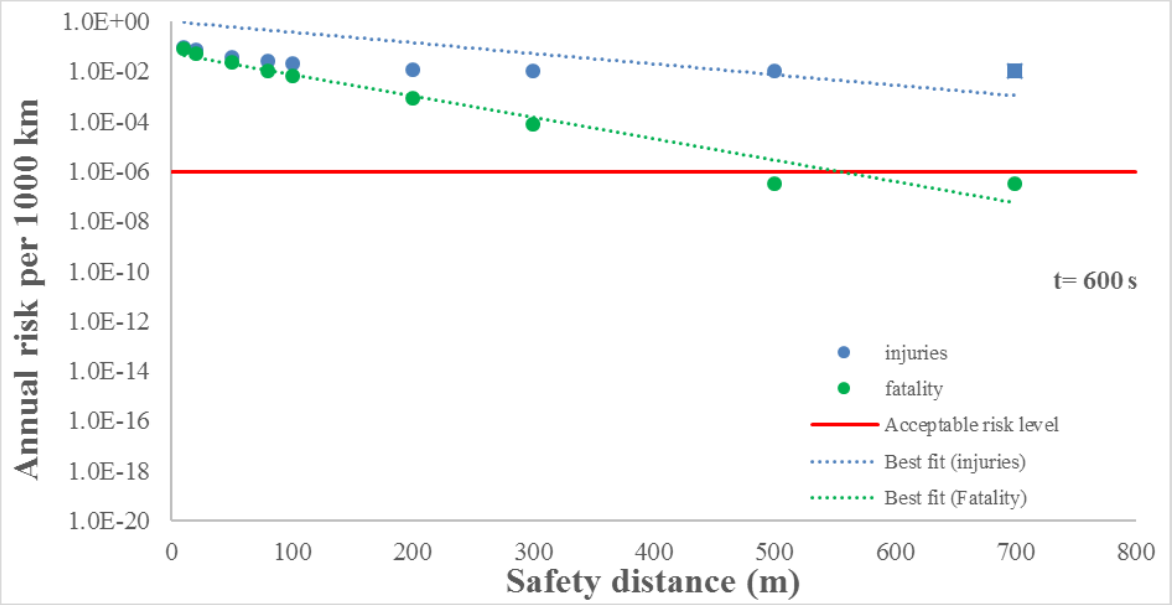

Figure 4.33: *Annual risk per 1000 km of damage to people (injuries and fatality) vs safety distance, in the case of atmospheric stability class F2, at t=600 s.*

4.11 Prevention and Mitigation systems

In order to reduce or eliminate long-term risks, resulting from accidental events, mitigation actions must be undertaken (PHMSA, 2013). The most rigorous risk-management procedures related to high-pressure hydrogen pipelines must be required, especially in urban areas (Penev et al., 2019).

The Hydrogen Tools Portal, developed by the Pacific Northwest National Laboratory with the support of the U.S. Department of Energy's Office of Energy Efficiency and Renewable Energy (EERE), suggests a risk reduction plan to reduce or eliminate the most critical issues, subsequently to the individualisation of the hazards and the classification of the risk.

Prevention measures are used to minimize to an acceptable level or remove the likelihood of occurrence and/or the severity of consequences (h2tools database, 2019 (b)).

The following steps for the hazard control are proposed:

1. Remove the hazard, if it is possible
2. Use materials with the same features and functions, but less hazardous
3. Introduce engineering controls in order to isolate the hazard
4. Define administrative controls (procedures, indicators and rules) for workers and any other people who may be involved in the hazard
5. Give personal protective equipment as a dowry

EIGA (European Industrial Gases Association), in the section of the report relating to the hydrogen pipeline systems (IGC Doc 121/14), after the identification of the hazards, suggests that, for each hazard, mitigation measures shall be determinate. These measures consist of: i) control of third party interference, ii) thickening of the pipe, iii) non-destructive tests on welds, iv) inerting of the pipe, v) pipe marking, vi) valves that detect an increase of flux or decrease of pressure, vii) mass balance to individuate a leak, viii) bury the pipeline, ix) protect the pipe with suitable coating , x) operating procedures (i.e. inspections programs, corrosion control programs, emergency plan).

4.11. 1 Prevention and Mitigation measures relating to the leakage

To prevent fire and/or explosion, gaseous hydrogen pipelines should be check periodically, with a hydrogen detector as suggested by EIGA (2014). National regulations and population density in the area of interest are decisive factors in establishing the periodicity of the controls, generally expected between 1 to 4 times per year. Valves, flanged connections and compression fitting are the crucial points to be kept under observation.

Catastrophic failure of gaseous hydrogen pipeline can be caused by corrosion phenomena: i.e., hydrogen gas embrittlement at ambient temperature (internal corrosion) and stress corrosion cracking of line pipe materials (external corrosion). Hight values of temperature and pressure help these phenomena and the risk can be mitigated by low stress levels. Fixed the operative temperature and pressure, thicker pipeline walls and thermal relieving residual welding stresses are used to maintain lower stresses, generally.

Risks related to these corrosion mechanisms can be reduced if advisable materials are used. Steels and stainless steel are subject to the embrittlement in hydrogen gas environments. Purity, temperature and pressure are some factors that may favor this phenomenon.

From the analysis of various accidents, it results that the most frequent cause of leaks is the corrosion due to the difference in electric potential between the external part of the pipe and the soil. An electrochemical cell is generated that removes metal from the pipe, and this can cause a leak in the pipe over time. This type of corrosion can be prevented through a good cathodic protection, according to established standards (i.e. NACE RP 177, EN 12954).

Furthermore, to reduce the possibility of occurrence of a leak in the pipe, are suggested welded connections.

Valves are used to resize a possible leak.

Portions of entire pipeline are isolated through isolation valves, located in easy to reach point to be manually closed. Control and pressure reducing valves are employed to monitor the flow and the pressure. If the pressure arises above the maximum allowable working pressure, safety relief valves, installed in the closest point to be protected, are used.

Several controls, moreover, are generally provided to prevent the pipeline from breaking. A pneumatic or a hydrostatic pressure test is established to control the values of pressure. Radiographic examination of the weld is performed to investigate the integrity of the joints.

CHAPTER 5

Conclusions

Hydrogen has been identified as the “energy carrier of the future”, both because it is an inexhaustible source, and because its combustion does not produce pollutants. In order to make it available at point of use, one of the safest and cheapest ways to transport and deliver large quantities of hydrogen is represented by pipelines.

From a safety point of view, hydrogen pipeline accidents can result in various outcomes and different effects can manifest on buildings and people located in the vicinity of the failure.

In this thesis, a multi-disciplinary procedure has been presented in order to assess the damage to people and buildings involved in the accidental events that occur with a major probability, as a consequence of a gaseous hydrogen pipeline failure. From the analysis of the literature, the probability of hydrogen pipeline rupture has been estimated to 0.126/year per 1,000 km. The events that occur with a major frequency have been investigated: both jet fires and explosions were taken into consideration.

Following an explosion, the effects that can occur on people and buildings near the accident location are related to the values of overpressure and impulse generated by the explosion itself.

Different atmospheric stability classes have been considered, in order to analyse various scenarios, from extremely unstable to moderately stable ones. Both explosivity classes 6 (low ignition power) and 9 (high ignition power) has been considered.

Pressure-impulse diagrams have been employed to estimate the blast damage to structures. Two different structural components have been considered, i.e. reinforced concrete (RC) columns and tuff stone masonry (TSM) walls, and their different behaviour under the event of the explosions have been investigated.

Combinations of overpressure and impulse have been selected and simulations with the SLAB integral model have been carried out. It was predicted that the RC columns do not suffer damage for all P-I combinations analysed. In the case of natural-gas explosion, the RC columns are not subjected to a collapse, neither. TSM walls are involved in a collapse for different P-I combinations, instead. The lower value of overpressure at which damage occurs is 6 kPa for an impulse of 750 kPa ms. In this case, the same trend has been observed in the case of natural-gas explosions, too.

To confirm this behaviour, a case study has been investigated and several collapse conditions have been identified. A blast demand radius at different levels of peak overpressure and impulse has been evaluated. A safety distance of 1000 m was predicted in all the cases investigated. Only in the case of explosivity class 9 and atmospheric stability D5 a higher value of safety distance has been found (2000 m).

The results of the simulations have been analysed taking into account acceptance criteria proposed in literature. A value of 10^{-6} / year per 1000 km has been chosen.

For the assessment of the damage that people involved in an explosion due to a hydrogen pipeline rupture can suffer, Probit functions available in the literature have been used. People can be injured both directly as indirectly; the level and the types of harms depend on the values of overpressures and impulses reached. Damage to human organs, which are mostly affected by sudden pressure changes (lungs and eardrum) may be manifested. In addition, people can be subjected to damage caused by head impact and whole-body displacement, because they can be thrown away due to the intensity of the blast wave. The possible injuries to people inside a building have been considered, too, since the buildings may partially or completely collapse as a result of an explosion.

From the analysis of the results, a distance of 1000 m has been estimated as safety distance in the case of hydrogen explosions in the considered operating conditions.

The other possible scenario that may arise following a pipeline rupture is a jet fire, and the damage to people due to such accidental event has been investigated through Probit functions, too. The level and the type of harm depend on the intensity of radiative heat flux generated by the hydrogen flame. People can suffer damage in terms of fatalities and injuries (first and second-degree burns, mainly). The intensity of the damage depends on the exposure duration to the heat flux, too. At larger distances from the flame, the radiative heat flux to which people are exposed decreases, and the level of damage is reduced.

Depending on the time of exposure, different safety distances have been estimated. For a small time of 60 s, a distance of about 200 m has been evaluated. For an exposure duration of 300 s a safety distance of about 700 m for injuries and a safety distance of about 300 m for fatalities was calculated.

In conclusion, a safety distance of 300 m from the axis of the jet fires has been proposed in the case of hydrogen jet fires arising in the operative conditions considered.

The probabilistic procedure presented may be employed in order to design new hydrogen pipeline networks and to assess the existing ones.

However, to reduce the estimated safety distances, risk prevention and mitigation measures must be taken into account.

The use of standard materials, in accordance with national and international regulations, can prevent corrosion phenomena that may cause over time larger or smaller leaks and generate gas dispersion with disastrous consequences (explosions or jet fires).

The installation of valves to control the pressure, flow rate and tightness of the joints allows prompt intervention in the event of any anomalies.

Preventive and control tests can in any case prevent a loss from occurring and therefore the consequent accident.

Finally, if the procedure is used to build a new pipeline system, it is advisable to build buildings that have reinforced concrete structural elements, since they do not suffer damage related to the collapse and therefore the safety distances to be adopted are reduced those proposed for the protection of people who are in the vicinity of the accidental event.

References

Adam J., Parisi F., Sagaseta J., Lu X., 2018, *Research and practice on progressive collapse and robustness of building structures in the 21st century*, Engineering Structure Journal, 173, 122-149.

AIChE Center for Chemical Process Safety, 2000, *Guidance for Consequence Analysis of Chemical Releases*, Center for Chemical Process Safety, American Institute of Chemical Engineers, New York: American institute of Chemical Engineers.

Air Liquide, 2005, *Questions and Issues on Hydrogen Pipelines, Pipeline Transmission of Hydrogen,* Doe Hydrogen Pipeline Working Group Meeting, August 31, 2005, available at https://www.energy.gov/sites/prod/files/2014/03/f10/hpwgw_questissues_campbell.pdf (accessed on 20.03.2019).

Balat M., 2008, *Potential importance of hydrogen as a future solution to environmental and transportation problems*, International Journal of Hydrogen Energy, 33, pp. 4013-4029.

Baykara S.Z., 2018, *Hydrogen: A brief overview on its sources, production and environmental impact,* International Journal of Hydrogen Energy, 43, pp. 10605-10614.

Bedel L., Junker M., 2006, *Natural gas pipelines for hydrogen transportation*, Proceedings of 16th World Hydrogen energy Conference 2006 (WHEC 2006), 13-16 June 2006, Lyon, France, ISBN:9781622765409, 1006-1010.

Bezedek R. H., 2019, *The hydrogen economy and jobs of the future*, Renewable Energy and Environmental Sustainability, 4, 1.

Brunesi E., Parisi F., 2017, *Progressive collapse fragility models of European reinforced concrete framed buildings based on pushdown analysis*, Engineering Structure Journal, 152, 579-596.

Consalvi J. L, Nmira F., 2019, *Modeling of large-scale under expanded hydrogen jet fires*, Proceedings of the Combustion Institute, 37, pp. 3943-3950.

Crowl D.A., 2003, *Understanding explosions,* American Institute of Chemical Engineers, New York.

Crowl D.A., Louvar J., 2011, *Chemical process safety fundamentals with applications*, 3rd ed. Prentice Hall, Upper Saddle River.

DM 17.01.2018: *Norme tecniche per le costruzioni*, Italian Ministry of Infrastructure and Transportation, Rome, 2018 [in Italian].

DNV Technica, 2001, *Human resistance against thermal effects, explosions effects, toxic effects and obscuration of vision*, DNV Technica, Scandpower A/S, Det Norske Veritas, Oslo, Norway.

DNV, 2015, *Risk Acceptance Criteria and Risk Based Damage Stability*. Final Report, part 1: Risk Acceptance Criteria: Report no.: 2015-0165, Rev 2, 2015.

EGIG, 2011, *8th Report of the European Gas Pipeline Incident* Data Group. Groningen: European Gas Pipeline Incident Data Group.

EGIG, 2015, *9th Report of the European Gas Pipeline Incident* Data Group. Groningen: European Gas Pipeline Incident Data Group.

EIGA, 2007, European Industrial Gases Association, *Determination of safety distances*, IGC Doc 75/07/E, Revision of Doc 75/01/rev. 2007.

EIGA, 2014, European Industrial Gases Association, *Hydrogen Pipeline Systems*, IGC Doc 121/14, Revision of Doc 121/04.

Eisenberg N.A., et al., 1975, *Vulnerability model: a simulation system for assessing damage resulting from marine spill*, Final Report SA/A-015 245, US Coast Guard.

Ekoto I.W., Houf W.G., Ruggles A.J., Creitz W.L., Li J.X., 2012, *Large-scale hydrogen jet flame radiant fraction measurements and modeling*, In: Proceedings of the International Pipeline Conference, Calgary, Canada, September 24-28, 2012.

Ekoto I. W., Ruggles A. J., Creitz W. L., Li J. X., 2014, *Updated jet flame radiation modeling with buoyancy corrections*, International Journal of Hydrogen Energy, 39, pp. 20570-20577.

Ellingwood B.R., 2006, *Mitigating risk from abnormal loads and progressive collapse*, Journal Performance Constructed Facilities, 20, pp. 315-323.

Ermark D.L., 1990, *SLAB an atmospheric dispersion model for denser-than air releases*, (URCL-MA-105607). Livermore: Lawrence National Laboratory.

Eurocode 1, 2006, *Actions on structures – Part 1-7: General actions – Accidental actions*., Comité Européen de Normalisation, Brussels.

Eurostat data of Statistics on the production of manufactured goods, available at http://ec.europa.eu/eurostat/web/main accessed on 20.03.2019.

Federal Emergency Management Agency, 1987, *Handbook of Chemical Hazard Analysis Procedures*, Washington, D.C.

Gerboni R., Salvador E., 2009, *Hydrogen transportation system: elements of risk analysis*, Energy, 34, pp. 2223-2229.

Han S.H., Chang D., Kim J.S., 2014, *Experimental investigation of highly pressurized hydrogen release through a small hole*, International Journal of Hydrogen Energy, 39, pp. 9552-9561.

Hankinson G., Lowesmith B. J., 2012, *A consideration of methods of determining the radiative characteristics of jet fires*, Combustion and Flame, 159, pp.1165-1177.

HIAD 2.0, *Hydrogen Incidents and Accidents Database,* available at https://odin.jrc.ec.europa.eu/giada/, accessed on 05.05.2019.

HSE, 1991, *Major hazard aspects of the transport of dangerous substances*, Health & Safety Executive.

HSE, 2013, *Methods of approximation and determination of human vulnerability for offshore major accident hazard assessment*. UK 2010 SPC/Tech/OSD/30, rev 2013.

https://h2tools.org/hyarc/hydrogen-delivery September 2016.

https://h2tools.org/bestpractise/risk-mitigation, accessed on 19.12.2019.

Hydrogen Pipelines, available at https://h2tools.org/hyarc/hydrogen-delivery, accessed on 20.03.2019.

Hymes I., Boydell W., Prescott B., 1996, *Thermal Radiation: Physiological and Pathological Effects*, Institution of Chemical Engineers.

HYPER, 2008, HYPER Installation Permitting *Guide for Hydrogen and Fuel Cells Stationary Application*, WP2 D4.1, IPG 5th Draft, December 2008.

HyResponse, 2016 (a), Grant agreement No: 325348, Compiled by S. Tretsiakova-McNally; Reviewed by D. Makarov (Ulster University), *Lecture-Harm criteria for people and environment, damage criteria for structures and equipment.*

HyResponse, 2016 (b), *Basic of Hydrogen Safety for first responders, Lecture- Hydrogen fires.*

Huang Y., Li Y., Dong B., 2018, *Radiant Heat Flux Profile of Horizontally Oriented Rectangular Source Fuel Jet Fires,* Industrial and Engineering Chemistry Research, 57, pp. 1078−1088.

Imamaura T., Hamada S., Mogi T., Wada Y., Horiguchi S., Miyake A., Ogawa T., 2008, *Experimental investigation on the thermal properties of hydrogen jet flame and hot currents in the downstream region,* International Journal of Hydrogen Energy, 33, pp. 3426-3435.

ISO/IEC Guide 73: 2002, Risk management – vocabulary- guidelines for use in standard 2002.

Iwasaka M., Urano Y. and Hashiguchi Y., 1979, *Fire Hazard of Compressed Hydrogen by Rapid Leak,* Koatsu Gas (Journal of the High Pressure Gas Safety Institute of Japan), 16 (7), pp. 333-338.

Jeffries R.M., Hunt S.J., Gould L., 1997, *Derivation of fatality of probability function for occupant buildings subject to blast loads,* Health & Safety Executive.

Jo Y.D., Ahn B.J., 2006, *Analysis of hazard area associated with hydrogen gas transmission pipelines*, International Journal of Hydrogen Energy 31, 2122–2130.

Kinsella K. G., 1993, *A Rapid Assessment Technology for the Prediction of Vapor Cloud Explosion Overpressure,* International Conference and Exhibition on the Safety, Health and Loss Prevention in the Oil, Chemical and Process Industries, Singapore.

La Chance J., Houf W., Middleton B., Fluer L., 2009, *Analyses to support development of risk-informed separation distances for hydrogen codes and standards,* Sandia National Laboratories, Albuquerque, NM.

La Chance J., Tchouvelev A., Engebo A., 2011, *Development of uniform harm criteria for quantitative risk analysis of the hydrogen infrastructure,* International Journal of Hydrogen Energy, 36, pp. 2381-2388.

Less FP.,1994, *The assessment of major hazards: a model for fatal injury from burns*, Transactions of the Institution of Chemical Engineers, 72 (Part B):127-34.

Linde Engineering News, available at https://www.lindeengineering.com/en/news_and_media/press_releases/news-20190228 accessed on 20.03.2019.

Melani L., Sochet I., Rocourt X., Jallais S., 2009, *Review of methods for estimating the overpressure and impulse resulting from a hydrogen explosion in a confined-obstructed volume*, 3rd International Conference on Hydrogen Safety September 16-18, 2009, Ajaccio, Corsica, France.

Merchant Hydrogen Plant Capacities, available at https://h2tools.org/hyarc/hydrogen-production accessed on 20.03.2019.

Mirza N.R., Degenkolbe S., Witt W., 2011, *Analysis of hydrogen incidents to support risk assessment,* International Journal of Hydrogen Energy, 43, pp. 10605-10614.

Mogi T., Nishida H., Horiguchi S., 2005, *Flame characteristics of high-pressure hydrogen gas jet,* In: Proceedings of first International Conference on Hydrogen Safety (ICHS2005), Pisa, Italy.

Mogi T., Horiguchi S., 2009, *Experimental study on the hazards of high-pressure hydrogen jet diffusion flames,* Journal of Loss Prevention in the Process Industries, 22, pp. 45– 51.

Molina A., Schefer R. W., Houf W. G., 2007, *Radiative fraction and optical thickness in large-scale hydrogen-jet fires*, Proceedings of the Combustion Institute, 31, pp. 2565-2572.

Molkov V., 2012, *Fundamentals of Hydrogen Safety Engineering* I, ISBN: 978-87-403-0226-4. Available free at bookboon.com.

Mudan K. S. and Croce P. A., 1988, *Fire Hazard Calculations for Large Open Hydrocarbon Fires*, SFPE Handbook of Fire Protection Engineering, Boston, MA: society of Fire Protection Engineers.

NFPA, NFPA 2, 2011, *Hydrogen Technologies Code*, Quincy, MA 02169-7471, NFPA 2.

Ngo T., Mendis P., Gupta A, Ramsay J., 2007, *Blast Loading and Blast Effects on Structures-An overview*, eJSE International, pp. 76-90.

Okabayashy K., Nonaka T., Sakata N., Takeno K., Hirashima H. and Chitose K., 2005, *Characteristics of dispersion for leakage of high-pressurized hydrogen gas*, Japan Society for Safety Engineering, 44(6), pp. 391-397.

Papadakis G.A., 1999, *Major hazard pipelines: a comparative study of onshore transmission accidents*, Journal of Loss Prevention in the Process Industries, 12, pp. 91-107.

Parisi F., 2015, *Blast fragility and performance-based pressure-impulse diagrams of European reinforced concrete columns*., Engineering Structures, 103, 285-297.

Parisi F., Balestrieri C., Asprone D., 2016, *Blast resistance of tuff stone masonry walls*, Engineering Structures 113, pp. 233-244.

Penev M., Zuboy J., Hunter C., 2019, *Economic analysis of a high-pressure urban pipeline concept (HyLine) for delivery hydrogen to retail fueling stations*, Transportation Research Part D 77, pp. 92-105.

Pasquill F., 1961, *The estimation of the dispersion of windborne material*, Meteorological Magazine, 90, pp. 33-49.

Pietersen C. M., Huerta S.C., 1985, TNO 84-0222*: Analysis of the LPG Incident in San Juan Ixhuatepec, Mexico City, 19 November 1984, Apeldoorn*, The Netherlands: Netherlands Organisation for Applied Scientific Research.

PHMSA, *Gas Distribution, Gas Gathering, Gas Transmission, Hazardous Liquids, Liquefied Natural Gas (LNG) and Underground Natural Gas Storage* (UNGS), Annual Report Data, Available https://www.phmsa.dot.gov/data-and-statistics/pipeline/gas-distribution-gas-gatheringgas-transmission-hazardous-liquids, accessed on 16.06.2018.

Proust C., Jamois D., Studer E., 2011, *High pressure hydrogen fires*, International Journal of Hydrogen Energy, 36, pp. 2367-2373.Rigas F., Amyotte P., 2013, *Myths and Facts about Hydrogen Hazards*, Chemical Engineering Transactions, 31, pp. 913-918.

Russo P., Parisi F., Augenti N., Russo G., 2014, *Derivation of risk areas associated with high-pressure natural-gas pipelines explosions including effects on structural components*, Chemical Engineering Transactions 36, pp. 289-294.

Russo P., Parisi F., 2016, *Risk-targeted safety distance of reinforced concrete buildings from natural-gas transmission pipelines*, Reliability Engineering and System Safety, 148, pp. 57-66.

Russo P., De Marco A., Mazzaro M., Capobianco L., 2018, *Quantitative risk assessment on a hydrogen refuelling station*, Chemical Engineering Transactions 67, 739-744.

Saffers J., B., Molkov V.V., 2014, *Hydrogen safety engineering framework and elementary design safety tools*, International Journal of Hydrogen Energy, 39, pp. 6268-6285.

Shi Y., Hao H., Li Z-X., 2008, *Numerical derivation of pressure–impulse diagrams for prediction of RC column damage to blast loads*, International Journal of Impact Engineering, 35 (11), pp.1213-1227.

Schefer R. W., Houf W. G., Bourne B., Colton J., 2006, *Spatial and radiative properties of an open-flame hydrogen plume*, International Journal of Hydrogen Energy, 31, pp.1332-1340.

Schefer R. W., Houf W. G., Williams T. C., Bourne B., Colton J., 2007, *Characterization of high-pressure, underexpanded hydrogen-jet flames*, International Journal of Hydrogen Energy, 32, pp. 2081–2093.

Shirvill L.C., Roberts P.T., Roberts T.A., Butler C.J., Royle M., 2006, *Dispersion of hydrogen from high-pressure sources*, Proceedings of Hazards XIX conference. Manchester, UK, March 27-30, 2006.

Stoll A.M and Chianta M.A, 1969, Method and rating system for evaluation of thermal protection, Aerosp. Med., 40 (II), pp. 1232-1238.

Swain R., 2011, *Fuel Leak Simulation*, Proceedings of the 2001 DOE Hydrogen Program Review, NREL/CP-570-30535.

TNO, 1989, *Methods for the determination of possible damage*, Green Book, In: CPR 16E., The Netherlands Organization of Applied Scientific Research.

TNO, 2005, *Methods for the calculation of physical effects due to releases of hazardous materials (liquid and gases)*, Yellow book, van den Bosh, C.J. H., Weterings, R.A.P.M. (Eds) TNO, The Hague.

Tsao C.K., Perry W.W., 1979, *Modifications to the vulnerability model: a simulation system for assessing damage resulting from marine spills*, Report ADA 075 231 US Coast Guard.

Turns S.R., Myhr F.H., 1991, *Combustion Flame*, 87, pp. 319-335.

Woodson S.C., Baylot J.T., 1999, *Structural collapse: quarter-scale model experiments*, Technical Report SL-99-8, US Army Corps of Engineers Engineer Research and Development Center.

Woodson S.C., Baylot J.T., 2000, *Quarter-scale building/column experiments*, In: Mohamed E, editor. Proceeding of advanced technology in structural engineering, Philadelphia, PA, USA, p. 1-8.

Zhang X., Xiao L., 2018, *Analysis of Hazardous Chemicals Transportation Accidents and Transportation Management*, Chemical Engineering Transactions, 67, No. 1, pp. 745-750.

Zhou K., Liu N., Zhang L., Satoh K., 2014, *Thermal Radiation From Fire Whirls: Revised Solid Flame Model, Fire Technol.*, 50(6), pp. 1573–1587.

Zhou K., Jiang J., 2016, *Thermal Radiation From Vertical Turbulent Jet Flame: Line Source Model*, Journal of Heat Transfer, 138, pp. 042701-042708.

Nomenclature

a_P Plank's absorption coefficient

b co-volume

C_d drag coefficient

C_{H2} hydrogen concentration

c_p specific heat at constant pressure

c_v specific heat at constant volume

d pipeline diameter

d_{hole} hole diameter

D damage

e…..relative error

E event

F….. view factor

f_F friction factor

I impulse

$k_{1……}$empirical constant of Probit functions

$k_{2……}$empirical constant of Probit functions

L length of pipeline from the compression station

L_f…..flame length

m_{fuel} mass flow rate

W_f….flame width

P pressure

P_a ambient pressure

P_o operating pressure

Pr probability

P_v average compressive stress

P_w water partial pressure

Q_{peak} mass flow rate

Q_{steady} stationary mass flow rate

R distance from the centre of explosions

r distance from the centre of jet fires

R_{H2} hydrogen gas constant

Re Reynold's number

RH relativity humidity

T_a ambient temperature

T_o initial temperature

T temperature

T_{ad}...adiabatic temperature

T_f….flame temperature

T_S source material temperature

v velocity

$v_{b,o}$ mean wind speed

E Young's modulus

f_m peak compressive strength of masonry

h_w height TSM walls

S distance

S_{rad} radiative power

t_w thickness

q radiative heat flux

V…..causative variable

Y…..Probit function

Y_s…stoichiometric mass fraction

z compressibility factor

Greek letter

α ratio of the effective hole area to the pipe sectional area

γ specific heat ratio of hydrogen

ΔP_s overpressure

ΔH_c combustion heat

λ_R frequency of pipeline rupture occurrence

ν Poisson's ratio

ρ density

τ atmospheric transmissivity

χ_{rad} radiative fraction